

Challenges for Perovskite Nanocrystals and How to Overcome Them

Carola Lampe

München, 2022

Challenges for Perovskite Nanocrystals and How to Overcome Them

Dissertation

zur Erlangung des Doktorgrades der Naturwissenschaften (Dr. rer. nat.)



an der Fakultät für Physik
der Ludwig-Maximilians-Universität München

vorgelegt von

Carola Lampe

aus Friedberg

München, 20. Mai 2022

Promotionskommission

Erstgutacher:

Prof. Dr. Alexander Urban

Zweitgutachter:

PD Dr. Bert Nickel

Vorsitzender:

Prof. Dr. Til Birnstiel

Beisitzer:

Prof. Dr. Ulrich Schollwöck

Tag der mündlichen Prüfung: 15. Juli 2022

dedicated to my family

Publications and conferences

Scientific Publications of Results Presented in This Work

* denotes equal contribution

- V. A. Hintermayr*, C. Lampe*, M. Löw, J. Roemer, W. Vanderlinden, M. Gramlich, A. X. Böhm, C. Sattler, B. Nickel, T. Lohmüller, A. S. Urban
Polymer nanoreactors shield perovskite nanocrystals from degradation
Nano Letters 19(8): 4928-4933 (2019)
- Q. Xue*, C. Lampe*, T. Naujoks, K. Frank, M. Gramlich, M. Schoger, W. Vanderlinden, P. Reisbeck, B. Nickel, W. Brütting, A. S. Urban
Doubly Stabilized Perovskite Nanocrystal Luminescence Downconverters
Advanced Optical Materials 2102791 (2022)
- T. Morgenstern, C. Lampe, T. Naujoks, M. Jurow, Y. Liu, A. S. Urban, W. Brütting
Elucidating the performance limits of perovskite nanocrystal light emitting diodes
Journal of Luminescence 220: 116939 (2020)
- F. Treber, K. Frank, B. Nickel, C. Lampe, A. S. Urban
An Ambient Atmosphere Low Temperature Based Synthesis for Lead-Free Double Perovskites
in preparation (2022) LFDP in preparation
- C. Lampe*, I. Kouroudis*, M. Harth, S. Martin, A. Gagliardi, A. S. Urban
Constrained Artificial Intelligence Guided Compositional Engineering of CsPbBr₃ Nanoplatelets
in preparation (2022)
- C. Lampe*, K. Frank*, B. Nickel, A. S. Urban
Elucidating Perovskite Syntheses Processes by In-Situ SAXS Analysis
in preparation (2022)

Additional Publications

- A. Singldinger, M. Gramlich, C. Gruber, C. Lampe, A. S. Urban
Nonradiative energy transfer between thickness-controlled halide perovskite nanoplatelets
ACS Energy Letters 5(5): 1380-1385 (2020)
- M. Gramlich, M. W. Swift, C. Lampe, J. L. Lyons, M. Döblinger, A. L. Efros, P. C. Sercel, A. S. Urban
Dark and Bright Excitons in Halide Perovskite Nanoplatelets
Advanced Science 9(5): 2103013 (2022)
- M. Gramlich, C. Lampe, J. Drewniok, A. S. Urban
How Exciton-Phonon Coupling Impacts Photoluminescence in Halide Perovskite Nanoplatelets
The Journal of Physical Chemistry Letters 12(46): 11371-11377 (2021)
- M. F. Lichtenegger, J. Drewniok, A. Bornschlegl, C. Lampe, A. Singldinger, N. A. Henke, A. S. Urban
Electron-Hole Binding Governs Carrier Transport in Halide Perovskite Nanocrystal Thin Films
ACS Nano 16(4): 6317-6324 (2022)

- S. Wang, M. Dysik, C. Lampe, M. Gramlich, D. K. Maude, M. Baranowski, A. S. Urban, P. Plochocka, A. Surrente
Thickness-Dependent Dark-Bright Exciton Splitting in Cs-based Nanoplatelets Revealed via Magneto-Optical Spectroscopy
submitted (2022)

Contributions to Conferences and Workshops

- *CeNS Workshop 'Celebrating NanoScience'* (Poster)
Venice, Italy, September 2018
- *MRS Spring Meeting* (Talk)
Phoenix, USA, April 2019
- *PSCO* (Talk)
Lausanne, Switzerland, October 2019
- *MRS Fall Meeting* (Poster)
Boston, USA, December 2019
- *9th International SolTech Conference* (Talk)
Munich, Germany, October 2020
- *e-conversion Conference* (Poster)
Munich, Germany, September 2021
- *CeNS Retreat* (Poster)
Kleinwalsertal, Austria, May 2022

Zusammenfassung

Bleihalogenid-Perowskit-Nanokristalle haben die Halbleiter-Community in den letzten Jahren aufgrund ihrer faszinierenden optoelektronischen Eigenschaften, wie hoher Quantenausbeute und präziser Einstellbarkeit der Bandlückenenergie, in Erstaunen versetzt. Während vornehmlich die hervorragenden optoelektronischen Eigenschaften von Perowskiten hervorgehoben werden, ist es weniger üblich, ihre Nachteile anzusprechen. Im Zuge dieser Arbeit werden mehrere Herausforderungen für Perowskit-Nanopartikel diskutiert und durch neuartige Syntheseverfahren angegangen. Die Arbeit konzentriert sich auf drei Hauptprobleme: Erstens, die intrinsische Stabilität von Perowskit-Nanokristallen, zweitens, das Finden der optimalen Emissionseigenschaften und schließlich die Toxizität von Blei.

In dieser Dissertation wird ein neuartiger synthetischer Ansatz unter Verwendung von Diblock-Copolymer-Nanoreaktoren verwendet, um Perowskit-Nanopartikel herzustellen. Die Polymermizelle bietet Schutz vor Umwelteinflüssen und unterdrückt ferner die Ionenwanderung. Der Syntheseprozess wird mittels dynamischer Lichtstreuung analysiert und im Folgenden material- und kosteneffizienter gestaltet. Darüber hinaus zeigen die mizellenverkapselten Nanokristalle, nach der Einführung organischer Liganden in die Syntheseroutine, eine Quantenausbeute von nahezu eins. Gleichzeitig wird ihre Haltbarkeit, insbesondere in dünnen Schichten, weiter erhöht. Die Anwendbarkeit von in Polymermizellen und organischen Liganden eingekapselten Perowskiten wird in einem Downconverter-Anwendung gezeigt, in der blaue Emission effizient in grüne umgewandelt wird.

Ein weiteres diskutiertes Thema ist das vorteilhafte Emissionsprofil anisotroper Emitter. Deren Überlegenheit bei potenziellen Geräteanwendungen wird demonstriert. Im Folgenden wird ein maschineller Lernalgorithmus entwickelt und eingesetzt, um die gezielte Synthese gewünschter Emissionswellenlängen zu ermöglichen und eine robustere Syntheseroutine zu generieren. Durch gezielte Nachbehandlung kann das gesamte sichtbare Spektrum mit anisotropen Perowskitemittern abgedeckt werden. Um das Verständnis des zugrunde liegenden Synthesemechanismus weiter zu verbessern, wird In-situ-Röntgenstreuung eingesetzt, um Syntheseschritte zu identifizieren und unbekannte Mechanismen aufzuklären. Die Bildung von anisotropen Perowskit-Nanoplättchen wird zeitabhängig beobachtet, während zeitgleich ihr Emissions- und Streuprofil überwacht wird.

Letztendlich wird eine neuartige Syntheseroutine für bleifreie Perowskite entwickelt und optimiert. Der Ansatz ist so konzipiert, dass er möglichst einfach und anspruchslos in Bezug auf die Laboranforderungen ist. Verschiedene Parameter wurden gescreent und optimiert. Zusätzlich wurde eine Mangan-Dotierung in die Synthese implementiert. Dabei werden bleifreie Nanokristalle synthetisiert, die mit den bisherigen Rekordkristallen, die in aufwändigen Prozessen hergestellt werden müssen, durchaus konkurrieren können.

Abstract

Lead halide perovskite nanocrystals have been astounding the semiconductor community in recent years due to intriguing optoelectronic properties, such as high quantum yields and large bandgap tunability. While everyone highlights the excellent optoelectronic properties of perovskites, it is less common to address their drawbacks. In the course of this thesis, several challenges for perovskite nanocrystals are discussed and approached by novel synthetic processes. The work focuses on three main challenges: First, the intrinsic stability of perovskite nanocrystals, second, finding the optimal emission properties, and lastly the toxicity of lead.

Throughout this thesis, a novel synthetic approach employing diblock copolymer nanoreactors is used to grow perovskite nanocrystals. The polymer micelle provides protection from environmental forces and further suppresses ion migration. The synthetic process is analyzed using dynamic light scattering and optimized to be more material- and cost-efficient. Furthermore, the micelle-encapsulated nanocrystals show near-unity quantum yield after the introduction of organic ligands in the synthetic routine. Simultaneously, their durability, especially in thin films, is further enhanced. The applicability of perovskites encapsulated in polymer micelles and organic ligands in devices, is shown in a downconverter device where they efficiently transform blue into green emission.

Another topic discussed is the beneficial emission profile of anisotropic emitters. The supremacy in potential device applications is demonstrated for 2D perovskite nanoplatelets. In the following, a machine learning algorithm is developed and employed to allow the targeted synthesis of desired emission wavelengths and to generate a more robust synthetic routine. By purposeful post-synthetic treatment, the whole visible spectrum can be covered using anisotropic perovskite emitters. To further enhance the understanding of the underlying synthetic mechanisms, in-situ X-ray scattering is deployed in combination with PL spectroscopy. The formation of anisotropic perovskite nanoplatelets is observed time-dependently while monitoring their emission and scattering profiles.

Ultimately, a novel synthesis routine for lead-free perovskite is developed and optimized. The approach is designed to be most facile and non-demanding regarding the laboratory requirements. Different parameters were screened and optimized. In addition, manganese doping was implemented in the synthesis. Lead-free nanocrystals able to compete with the current state-of-the-art nanocrystals can easily be synthesized with the new routine.

Table of Contents

Zusammenfassung	vii
Abstract	ix
1 Introduction	1
2 Fundamentals	3
2.1 Crystals and their Optoelectronic Basics	4
2.1.1 Electronic Structure in Crystalline Solids	4
2.1.2 Semiconductors	5
2.1.3 Light Absorption and Emission in Semiconductors	6
2.1.4 Confined Semiconductors	9
2.2 Metal Halide Perovskites	11
2.2.1 Crystal Structure	11
2.2.2 Optoelectronic Basics of Bulk Perovskites	12
2.2.3 Perovskite Nanocrystals	14
2.2.4 Challenges for Industrial Applications	19
2.3 Computational Methods in Nanocrystal Research	24
3 Materials and Methods	25
3.1 Nanocrystal Synthesis	26
3.1.1 Diblock Copolymer-Templated Synthesis	27
3.1.2 $\text{Cs}_{n-1}\text{Pb}_n\text{Br}_{3n+1}$ Nanoplatelets	27
3.1.3 Lead-Free Perovskite Nanocrystals	28
3.2 Structural Characterization	29
3.2.1 Transmission Electron Microscopy	29
3.2.2 X-ray Scattering	30
3.2.3 Dynamic Light Scattering	33
3.3 Optical Characterization	33
3.4 Computational Methods	35
4 Stability of Lead Halide Perovskites	37
4.1 Diblock Copolymer Micelles as Nanoreactors	38

4.2	Optimizing the Synthesis Using Dynamic Light Scattering	45
4.3	Integrating Organic Ligands	49
4.4	Summary	55
5	Optimizing the Emission Properties of Perovskites Nanocrystals	57
5.1	Directional Emission in Quasi-2D Nanoplatelets	58
5.2	Machine Learning Based Synthesis Optimization	62
5.3	Color Tunability of Nanoplatelets	67
5.4	Analyzing Syntheses Processes	71
5.5	Summary	76
6	Lead-Free Double Perovskites	77
6.1	Manganese Doped Cs ₂ NaBiCl ₆ Nanocrystals and Their Optical Properties	78
6.2	Impact of Manganese Content on Mn:Cs ₂ NaBiCl ₆ Nanocrystals	81
6.3	Reaction Temperature and its Effect	82
6.4	Longterm Stability of Mn:Cs ₂ NaBiCl ₆ Nanocrystals	82
6.5	Summary	83
7	Conclusion	85
	References	I
	List of Figures	IX
	List of Tables	XIII
	List of Abbreviations	XV
	Acknowledgments	XVII

1

Introduction

*'There's Plenty of Room at the Bottom:
An Invitation to Enter a New Field of Physics'*

This is the title of the famous lecture given by Richard Feynman at the annual American Physical Society Meeting at Caltech in December 1959.¹ This sentence marks the beginning of nanotechnology research. The word 'nano' refers to the factor of 10^{-9} and is indispensable in today's scientific research. Especially semiconductor and metal nanocrystals (NCs) are the main actors in nanoscience. They are used in multiple everyday life situations, e.g. as UV-light absorbers in sunscreen (ZnO and TiO₂ nanoparticles) or as main components in liquid-crystal displays (LCDs).^{2,3} The reason for the supremacy of nanoparticles was already postulated by Feynman in his lectures: macroscopic properties of a material are highly dependent on the size and dimension of the crystals. This effect has already been used unintentionally for centuries, e.g. in the coloring of glass windows using metal nanoparticles.^{4,5}

This thesis, however, will discuss a specific class of semiconductor – halide perovskites. While they have been known for almost a century, their properties as optoelectronic materials only earnestly entered discussion after first reports in 2009.^{6,7} Since then, they were used in many laboratories as sensitizers in solar cells. Today's record perovskite-based solar cells show efficiencies up to 25.5% in single junction cells and record-breaking 29.7% for perovskite-silicon tandem cells.^{8,9} With these numbers, perovskite-based solar cells are able to compete in the world market. Since 2014, however, scientific research has also turned to nanocrystalline lead halide perovskite (LHP).¹⁰ The jump from macroscopic crystals to NCs results in a change of the optoelectronic properties. While perovskite bulk crystals are predominantly used for their high absorption coefficient and facile synthesis, perovskite NCs are known for their near-unity photoluminescence quantum yield (PLQY) and easily tunable bandgap. They can be widely used in optoelectronic applications like light emitting diodes (LEDs), photodetectors, or optically pumped lasers, due to their unique properties.¹¹

However, LHPs suffer from few but significant drawbacks: Their most prominent disadvantage is their intrinsic instability in ambient conditions. Oxygen, moisture, and UV-light are known to affect the performance of LHP NCs. Furthermore, the ionic nature of LHPs makes them vulnerable to foreign ions and intrinsic ion migration. Especially halide ions are known to move freely through the crystal altering its properties reversibly or irreversibly. Furthermore, the emission properties of LHP NCs vary drastically for different perovskite compositions and morphologies. To build a perfect emitter, a detailed understanding of the emission profile, the NC synthesis and their adaptability towards multiple emission colors is necessary. Another major drawback of LHP NCs is their fundamental compound lead. The toxicity of lead drastically impedes the commercialization of LHP-based applications. Environmentally friendly alternatives are needed for a long-term and widespread application of perovskite compounds.¹²⁻¹⁶

In the course of this thesis, each of these problems will be approached individually. To understand the underlying nature of semiconductors, their basic concepts are discussed in [Chapter 2](#). In addition, an introduction to LHPs and especially in LHP NC chemistry is presented. The following [Chapter 3](#) shows all chemical and spectroscopic methods used in this thesis. The results of this work are divided in three chapters. [Chapter 4](#) investigates a novel synthetic approach to overcome the instability of LHP NCs. Polymer nanoreactors will be introduced and their performance as protection against environmental forces monitored. The resulting NC samples will be optimized and tested in an optoelectronic application. [Chapter 5](#) discusses the advantage of using anisotropic LHP NCs as emitters. Following this is a machine learning-based approach to optimize the synthesis of LHP nanoplatelets (NPL) approach as well as their optical properties. Furthermore, the synthetic procedure is analyzed using in-situ X-ray scattering and PL spectroscopy. Finally, [Chapter 6](#) presents a novel synthesis routine to form lead-free perovskite NCs in a facile low-temperature procedure.

2

Fundamentals

The work in this thesis is based on semiconductor crystals. Accordingly, this chapter presents the theoretical basics of semiconductors and their optical properties. The quantum confinement effect and its impact on semiconductor crystals will be discussed in the following. Since exclusively perovskites are investigated in this thesis, their structure and optoelectronic properties and the basic concepts of perovskite nanocrystal syntheses are presented. Furthermore, the challenges for perovskite nanocrystals in industrial applications are introduced and discussed.

2.1 Crystals and their Optoelectronic Basics

2.1.1 Electronic Structure in Crystalline Solids

A crystal is defined as an ordered arrangement of identical building blocks. The smallest subunit of particles forming the crystal by repetitive translation along well-defined axis is called the primitive unit cell. Therefore, each crystal is defined by a lattice and its translational symmetry and the basis providing the type and position of particles in the unit cell. The translational operation \mathbf{R} can be defined as

$$\mathbf{R} = n_1 \mathbf{a}_1 + n_2 \mathbf{a}_2 + n_3 \mathbf{a}_3 \quad (2.1)$$

with the primitive translation vectors a_i . The length and angles of the primitive translational vectors define the lattice type. There are 14 different Bravais lattices that describe 230 space groups. Each crystal can be categorized into one of them depending on its lattice parameters. The simplest 3D lattice is a simple cubic structure with orthogonal axes with the same length and one atom per lattice point, as can be seen in [Figure 2.1](#).¹⁷⁻¹⁹

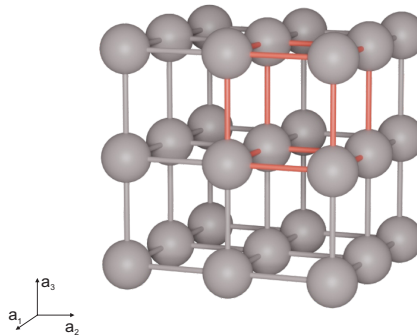


Figure 2.1: Simple Cubic Crystal Lattice Schematic display of a crystal cubic lattice with one atom per lattice site. An exemplary unit cell is marked in red.

In order to extract the electronic structure of the crystal the interaction of electrons within the crystal structure must be examined. For crystal-wave interactions it can be useful to consider the crystal structure in reciprocal space to simplify the consideration of electromagnetic waves. In reciprocal space, a wave vector \mathbf{k} can be represented as a point. The reciprocal lattice is directly related to its real space lattice. The reciprocal lattice vectors b_i need to fulfill the relation $\mathbf{R}\mathbf{G} = 2\pi n$, with $\mathbf{G} = \hbar b_1 + \hbar b_2 + \hbar b_3$ and $n = 1, 2, 3, \dots$, and can be obtained from the lattice vectors a_i :^{17,18,20}

$$b_i = 2\pi \frac{(a_j \times a_k)}{(a_1 \times a_2) \cdot a_3} \quad (2.2)$$

Where i, j and k represent a cyclic permutation of the indices 1, 2, and 3.¹⁷ Comparable to the real space, the reciprocal lattice consists of a periodic repetition of the smallest possible volume, here called the Brillouin zone (BZ). It provides all symmetry information about the crystal and can therefore be used to describe the properties of the entire crystal. To simplify the description even further, high

symmetry points within the BZ are defined and marked with Greek letters (inside the BZ) and roman letters (surface of BZ), the center of the BZ is always denoted with Γ (compare Figure 2.2).¹⁷

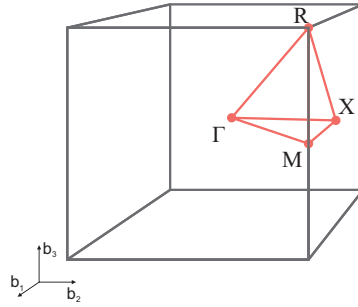


Figure 2.2: Brillouin Zone The first Brillouin zone of a simple cubic lattice with the corresponding high symmetry points. Adapted from Reference [21].

The periodic arrangement of particles in a crystal leads to a periodic potential $V(\mathbf{r}) = V(\mathbf{r} + \mathbf{R})$ made of atomic cores. Consequently Schrödinger's equation for electrons needs to be extended by the potential $V(\mathbf{r})$, leading to:

$$H\psi(\mathbf{r}) = \left[-\frac{\hbar^2}{2m_e} \Delta + V(\mathbf{r}) \right] \psi(\mathbf{r}) = E\psi(\mathbf{r}) \quad (2.3)$$

with the electron mass m_e and $-\hbar^2 \Delta$ as momentum operator. The wave function $\psi(\mathbf{r})$ is given by Bloch's theorem as a plane wave $e^{i\mathbf{k}\mathbf{r}}$ modulated by a periodic function with $u_{\mathbf{k}}(\mathbf{r}) = u_{\mathbf{k}}(\mathbf{r} + \mathbf{R})$:

$$\psi_{\mathbf{k}}(\mathbf{r}) = e^{i\mathbf{k}\mathbf{r}} \cdot u_{\mathbf{k}}(\mathbf{r}) \quad (2.4)$$

Thereby $u_{\mathbf{k}}(\mathbf{r})$ follows the same periodicity as the crystal lattice. Consequently, Bloch functions and their corresponding eigenvalues $E_{\mathbf{k}}$ experience the same periodic repetition in k -space allowing the description of all possible electron states within the first BZ.

$$E_{\mathbf{k}} = E_{\mathbf{k}+\mathbf{G}} = \frac{\hbar^2}{2m} |\mathbf{k} + \mathbf{G}|^2 \quad (2.5)$$

Schrödinger's equation can result in multiple different eigenvalues $E_n(\mathbf{k})$ for each wave vector k , with the band index n . Each band consists of discrete energy levels; however, due to the number of atoms in a macroscopic crystal, these levels can be considered quasi-continuous and are therefore described as energy bands. The dispersion relation is referred to as band structure. Energies without electronic states between distinct bands are called band gaps. Traditionally $E_n(\mathbf{k})$ is plotted against k following a defined path along high symmetry points in the BZ. If we assume the position in k space to be negligible, and only the number of states in an energy range is important, then the so-called density of states (DOS) can be used, which summarizes the number of states within an energy interval.²²

2.1.2 Semiconductors

To differentiate between metals, semiconductors (SCs), and insulators, not only the electronic band structure itself but the occupancy of the bands needs to be considered. The Fermi energy E_f describes the boundary between occupied and unoccupied states at 0 K. In metals, E_f lies within the conduction

band (CB), resulting in a partially filled band allowing electronic transport. For SCs and insulators, E_f lies above a fully filled valence band (VB) and beneath an empty CB. The difference in energy between the valence band maximum (VBM) and conduction band minimum (CBM) is defined as the bandgap. Insulators exhibit a bandgap of more than around 3 to 4 eV while for SCs the gap between VB and CB is smaller. The small energy gap results in a weak conductance of SCs at room temperature (RT) due to some electrons being thermally elevated from the VB in the CB according to Fermi-Dirac statistics:²²

$$f(E, T) = \frac{1}{\exp\left(\frac{E - E_f}{k_B T}\right) + 1} \quad (2.6)$$

Depending on their bandgap, SCs can be classified as direct or indirect. In the case of a direct SC the VBM and the CBM occur at the same point in k space, whereas in indirect SCs, they lie at different points (see Figure 2.3). The term direct and indirect refer to the nature of the lowest energy transition between the bands, as discussed in the following section.

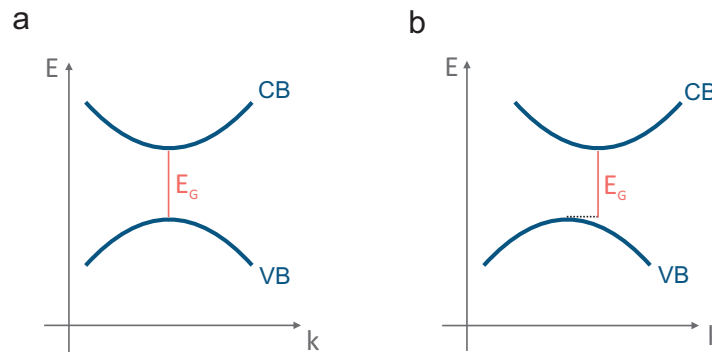


Figure 2.3: Direct and Indirect Bandgaps in Semiconductors (a) In direct SCs, the VBM and CBM are situated at the same k value. (b) In contrast, an indirect semiconductor is described by different k values for VBM and CBM.

2.1.3 Light Absorption and Emission in Semiconductors

Charge carriers can be excited electronically or optically, but for the scope of this thesis exclusively optical excitation was applied. Through absorption of photons, electrons can jump to an excited state. If the energy of a photon exceeds the bandgap energy, an electron can be excited into an energetically higher band. This process is called an interband transition. The initial state in the lower band is unoccupied, a so-called hole remains. A hole is considered a positively charged quasi-particle. An absorption process therefore creates an electron-hole pair. Electron and hole are oppositely charged particles and are consequently subjected to Coulomb interaction. The e-h pair can enter into a bound state; the e-h pair is then referred to as an exciton. Excitons can be found in many crystalline materials. Depending on the material and circumstances, excitons can be categorized into two main types:²² Wannier-Mott excitons are primarily found in inorganic SCs. They exhibit a large radius about many lattice points and are therefore considered delocalized on the order of 10 nm. Since the thermal energy $k_B T$ equals 25 meV at RT these excitons are mainly observed at low temperatures. In contrast, Frenkel excitons have larger binding energies of 0.1 to 1 eV, allowing their existence at RT. Frenkel excitons exhibit a radius in the range of the size of a unit cell binding them to specific lattice points. Consequently, they can be considered as bound or localized excitons. Wannier-Mott excitons dominate the material discussed in this thesis, hence, they shall be discussed further.

To calculate the energies of the bound state of excitons, it is convenient to compare the bound electron-hole pair to a hydrogen atom. There, the center of mass motion describes the overall system's energy and yields a parabolic dispersion. The combined exciton wavevector is given by $\mathbf{K} = \mathbf{k}_e + \mathbf{k}_h$. Due to the large exciton radius, the dielectric screening $\epsilon = \epsilon_0\epsilon_r$ of the crystals must be considered as well as the reduced mass of the exciton μ :

$$\mu = \left[\frac{1}{m_e^*} + \frac{1}{m_h^*} \right]^{-1} \quad (2.7)$$

By using the Bohr model, the energetic states of the exciton can be expressed as

$$E_n = R_y^* \frac{1}{n^2} = \frac{\mu e^4}{32 \pi^2 \epsilon_0^2 \epsilon_r^2 \hbar^2} \frac{1}{n^2} \quad (2.8)$$

with the principle quantum number n and the exciton Rydberg energy R_y . The radius of the electron-hole pair is given by the exciton Bohr radius and is defined as:

$$a_{\text{ex}} = \frac{4 \pi \epsilon_0 \epsilon_r \hbar^2}{\mu e^2} \quad (2.9)$$

The existence of Wannier-Mott excitons extends the electronic band structure of a SC. Exciton states are introduced in the bandgap below the conduction band as seen in [Figure 2.4 b](#). It must be noted that due to a combined wavevector \mathbf{K} of electron and hole, the exciton states cannot be displayed in a standard band structure, and the so-called two-particle picture is introduced. It shows the energetic states of electron-hole pairs depending on their combined wavevector \mathbf{K} . Equally to free charge carriers, an exciton can be created through photon absorption. Due to energy and wavevector conservation during absorption, excitons can only be created at intersections of the dispersion relations of excitons and photons.

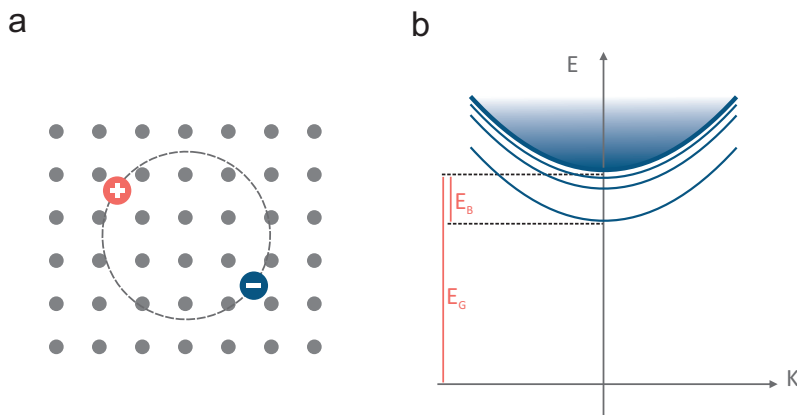


Figure 2.4: Wannier-Mott Exciton and its Energetic States (a) Schematic representation of a Wannier-Mott exciton. The bound electron-hole pair is delocalized over several lattice points. (b) Two-particle picture of e-h pairs. The blue filled area describes the regime for free electron-hole pairs, the so called continuum. Beneath this lie discrete exciton states. The energetic difference between the continuum dispersion and the lowest lying 1s exciton state defines the exciton binding energy E_B .

Whether free charge carriers or excitons dominate in a crystal is strongly dependent on the temperature of the system. The larger $k_B T$ becomes compared to the exciton binding energy, the more prevalent

free e-h pairs are. The introduction of excitonic states is visible in the absorption spectra of a SC, at low temperatures, an excitonic peak at lower energy than the absorption onset will be observable.

In the last section, optical excitation of electrons was discussed. The reverse process of an electron dropping from its excited state will be discussed in the following. The emission of light induced by radiative interband transitions is called photoluminescence (PL). In general, PL involves three distinct steps. Firstly, electron-hole pairs must be excited by optical excitation. Secondly, excited charge carriers will relax towards the band edges. Thirdly, the electron-hole pairs recombine radiatively, emitting a photon. As electrons are usually excited in a higher state than the conduction band, they lose their energy by generating lattice vibrations (phonons). This rapid process is termed relaxation and happens on times scales of 10s of ps. Several phonon scattering events will occur until the electron reaches the bottom of the conduction band (or of the 1s exciton parabola). There, electrons remain for a longer time and distribute according to the thermal energy following Fermi Dirac statistics. The recombination of electrons and holes can be radiative or non-radiative. In the case of radiative recombination, an electron-hole pair recombines, and a photon with energy corresponding to the energy gap between the electron in the CB and the hole in the VB is released. In contrast, non-radiative recombination does not produce a photon, but the energy is transferred to other quasi-particles such as phonons or other charge carriers.²³ To define how efficient an emitter is, it is convenient to determine the photoluminescence quantum yield (PLQY) of a material. The PLQY compares the rate constants of radiative (k_r) and nonradiative (k_{nr}) processes and gives a value between 0 and 1. A PLQY of 1 corresponds to 100% describing a perfect emitter with pure radiative recombination. A PLQY of 0% means the material does not emit light, and non-radiative recombinations are predominant. In other words, the PLQY describes how many of the absorbed photons (N_{absorbed}) recombine radiatively and are therefore reemitted (N_{emitted}).

$$PLQY = \frac{k_r}{k_r + k_{nr}} = \frac{N_{\text{emitted}}}{N_{\text{absorbed}}} \quad (2.10)$$

The overall emission footprint of a SC is affected by two different effects: homogenous and inhomogeneous broadening. The foundation of their properties will be presented in the following. Inhomogeneous broadening is a temperature-independent effect induced by inhomogeneities in a sample. For nanocrystals these can be found in their size distribution, their surface defects, and the surrounding dielectric environment. Minor deviations from each other can cause slightly different emission properties for individual crystals in a sample. Generally, all these effects follow a normal distribution, hence, inhomogeneous broadening can be described by a Gaussian function. For homogeneous broadening, it is convenient to consider temperature-dependent and temperature-independent contributions. The so-called natural linewidth of a spectrum is temperature-independent. Based on Heisenberg's uncertainty principle, the emission linewidth of an emitter is broadened even at 0 K.²⁴ Additionally, the linewidth is affected by scattering processes in the sample, e.g. carrier-carrier or carrier-phonon scattering. Especially the carrier-phonon interactions are strongly temperature-dependent. Phonons are quasi-particles describing the vibrational motions of atoms in a periodic arrangement. They are characterized by a wave vector \mathbf{k} and a frequency $\omega(\mathbf{k})$ and divided into acoustic and optical phonons. Thereby acoustic phonons describe the coherent movement of atoms in the same direction. Optical phonons only occur in solids with more than one atom in their smallest unit cell. They describe out of phase motions of neighboring atoms within the same unit cell.

Table 2.1: Quantum Confinement Overview of different types of confinement depending on the number of free dimensions with the corresponding effect on the density of states²²

type of structure	quantum confinement	number of free dimensions	DOS
bulk	-	3	$\alpha E^{1/2}$
quantum well	1D	2	αE^0
quantum wire	2D	1	$\alpha E^{-1/2}$
quantum dot	3D	0	discrete

Generally, acoustic phonons lie energetically beneath optical phonons in their respective dispersion relations, and optical phonons possess a frequency and energy unequal zero at the BZ center. Optical phonons follow Bose-Einstein statistics and are therefore more relevant to carrier-phonon interactions at higher temperatures. The interactions with acoustic phonons scale linearly with temperature. The homogenous broadening of a sample can be described as:

$$\Gamma(T) = \Gamma_0 + \Gamma_{ac}(T) + \Gamma_{op}(T) = \Gamma_0 + \sigma_{ac}T + \frac{\gamma_{op}}{\exp(E_{op}/k_B T) - 1} \quad (2.11)$$

with Γ_0 containing the natural linewidth and temperature-independent carrier-carrier interactions, $\sigma_{ac}T$ describing the interactions of charge carriers with acoustic phonons depending on the temperature and $\Gamma_{op}(T)$ as the interaction with optical phonons following Bose-Einstein statistics. Homogeneous broadening is generally described with a spectrum exhibiting a Lorentzian function. A Voigt profile describes the overall emission line width, a convolution of a Gaussian and Lorentzian function.^{25,26}

2.1.4 Confined Semiconductors

So far, the properties of infinitely large crystals have been discussed. However, the properties change drastically for nanocrystals in the size range of a few nanometers. Here quantum mechanical confinement effects need to be considered. Confined structures are generally classified by their dimensionality. Therefore, a crystal can be confined in one (quantum well), two (quantum wire), or three dimensions (quantum dot). Low-dimensional structures limit the mobility of electrons and holes due to the confinement. The partial localization of the charge carriers has two main effects: (1) the confinement energy increases the energy of electrons and holes, and (2) the shape of the DOS is changed. The effect of different dimensionalities of quantum confinement is summarized in [Table 2.1](#).

To determine the wave functions and energies of confined particles, it is convenient to look at the quantum mechanical description of a particle in a box. It is an example of a particle trapped between two infinitely high potential barriers, comparable to an electron in a 1D confined quantum well. The potential is given by:

$$V(z) = \begin{cases} 0 & 0 \leq z \leq L \\ \infty & \text{otherwise} \end{cases} \quad (2.12)$$

By solving Schrödinger's equation the wavefunction results in:

$$\psi_n(z) = \begin{cases} A_n \sin\left(\frac{\pi z}{L} n\right) & 0 \leq z \leq L \\ 0 & \text{otherwise} \end{cases} \quad (2.13)$$

with the corresponding eigenvalues:

$$E_n = \frac{\pi^2 \hbar^2}{2mL^2} n^2 \quad (2.14)$$

where L denotes the size of the box, m the electron mass, and n is an integer factor. Since the energy eigenvalues are proportional to $\frac{1}{L^2}$, the energetic gap will increase with decreasing L . Overall, the 'particle in a box' problem is a simplification of a quantum well and more sophisticated approaches are needed to calculate exact energies for confined systems. Nevertheless, it is useful to understand the underlying effect. Additional effects of quantum confinement are shortly summarized in the following. The continuum onset E_C appears as E_G in bulk crystals, in confined NCs it is increased by the confinement energy leading to $E_C = E_G + E_e + E_h$. This effect is shown in Figure 2.5. The increase in the confinement energy allows a limited tunability of the emission color of NC. Taking advantage of this effect was an integral part of this thesis.

The confinement also has a large impact on excitons and their binding energies. If the crystal size falls below the excitonic Bohr radius a_x , two effects appear. The decrease in the radius of electron and hole can reduce their screening, enhancing the exciton binding energy. Additionally, excitons experience a significantly lower dielectric function of the surrounding of the NCs. This leads to a stronger interaction between electron and hole and, consequently, increasing the exciton binding energy.

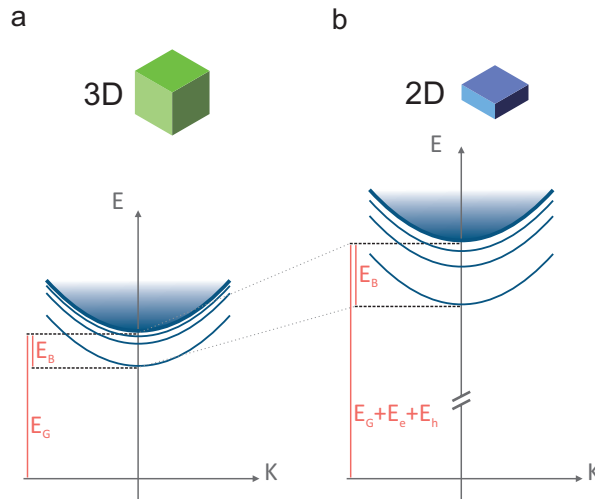


Figure 2.5: Effect of Quantum Confinement - From 3D to 2D The confinement in one dimension will lead to an increase in the continuum onset $E_C = E_G + E_e + E_h$ and an increased exciton binding energy E_B .

2.2 Metal Halide Perovskites

The original mineral perovskite CaTiO_3 was first reported by the German mineralogist Gustav Rose in 1839.⁶ It is named after the Russian mineralogist Lev Aleksevich von Perovski. Nowadays, the term perovskite describes a crystal structure that can be adopted by materials with the composition ABX_3 . Many perovskites are oxides, like the popular ferroelectric BaTiO_3 .^{27,28} The compounds in this thesis, however, are metal halide perovskites, more specifically mostly LHPs. LHPs were first reported by Wells in 1893; he revealed the structural and electronic properties of the inorganic perovskite CsPbX_3 ($X=\text{Cl}, \text{Br}, \text{I}$).²⁹ In 1978, Weber et al. published synthesis and structure details for organic-inorganic perovskites with methylammonium instead of cesium.³⁰ Extensive research on perovskites started after its recognition as an optoelectronic material for solar cells in 2009. The first application as a light emitter in LEDs was realized in 2014 by Tan et al.¹⁰ Nowadays, perovskite solar cells with efficiencies of 25.5% have been realized, while LEDs with external quantum efficiencies (EQE) beyond 20% are now produced, with research and development still ongoing.^{8,31}

2.2.1 Crystal Structure

In general, perovskite describes a material with the composition ABX_3 which adopts the perovskite structure with A being a monovalent cation, B a divalent cation and X a monovalent anion. The structure is a continuous array of corner-sharing BX_6 octahedra. An A -cation occupies the void between eight octahedra. In the case of LHP, the B position is occupied by Pb^{2+} and the X position by a halide anion (Cl^- , Br^- , I^-). The A -cation can be a small ion like Cs^+ or a small molecule like methylammonium (MA^+) or formamidinium (FA^+) to fit into the octahedral void.

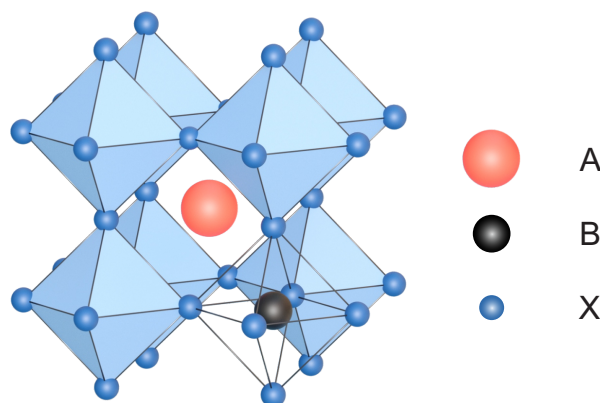


Figure 2.6: Perovskite Crystal Structure The perovskite structure ABX_3 consists of cornersharing BX_6 octahedra. Therein a B -cation (black) is coordinated by six X -anions (blue). The void in between is occupied by an A -cation (red).

The perovskite structure is not universal for any ABX_3 composition. Due to size constraints in the structure, only specific ratios of ion sizes are suitable for a perovskite compound. A guideline for the crystallization in this structure is the Goldschmidt tolerance factor t .³² It is based on the ionic radii of the components:

$$t = \frac{r_A + r_X}{\sqrt{2}(r_B + r_X)} \quad (2.15)$$

For perovskites, the Goldschmidt factor lies in the range of 0.81 to 1.0.^{33,34} In general, the Goldschmidt factor quantifies how efficiently the space of the crystal structure is filled. A tolerance factor of 1 indicates a perfect cubic crystal structure. Below $t = 1$, a distortion of the octahedra can be observed, lowering the overall symmetry, usually induced by a smaller A-cation. In the case of a larger A-cation and $t > 1$, the traditional perovskite structure is not formed but alternative low dimensional structures.³⁵ Furthermore, perovskites can be constrained by the octahedral factor $\mu = r_B/r_X$, which describes the stability of BX_6^{4-} octahedra, it contains the ionic radii of the B and X ions, and ranges between 0.44 and 0.9 for stable octahedra. Combining the Goldschmidt tolerance factor t and the octahedral factor μ makes it possible to predict the structure and phase of ternary LHPs. Figure 2.7 shows the parameter space of LHPs with respect to the ionic radii of the A-cation and X-anion (B-cations are exclusively lead). The boundaries of the tolerance and octahedral factors are marked in red and blue, respectively. Additionally, commonly used ions are marked at their respective position. It can be seen that larger molecular cations like FA or ethyl ammonium (EA) are at the edge of stable perovskite structures depending on the used halide ion.

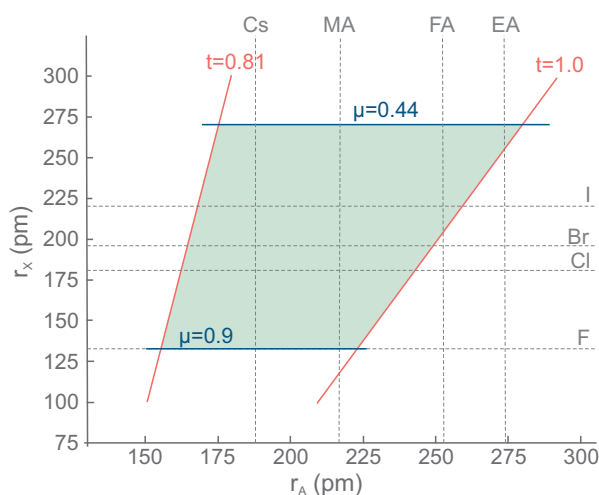


Figure 2.7: Structure Factors for 3D Lead Perovskites Parameter space for 3D LHPs as a function of A-cation and X-anion ionic radii. Blue and red lines mark the boundaries of the octahedral and tolerance factor, respectively. The green area marks section in which stable perovskites can be achieved. Adapted from Reference [34].

In this thesis, mainly $CsPbBr_3$, $MAPbBr_3$ and $MAPbI_3$ perovskites will be discussed. Cs^+ is a small cation with an ionic radius of 167 pm,³⁶ consequently it does not occupy a lot of space in the structure resulting in a lower symmetry phase. $CsPbBr_3$ is found to be in an orthorhombic phase at RT caused by a tilting of the octahedra. Only by heating the crystal to 88 °C are a tetragonal, and at 130 °C, a cubic structure observed.³⁷ MA^+ , in contrast, exhibits an ionic radius of 217 pm³⁶ and is therefore much larger than Cs^+ . Hence, $MAPbX_3$ ($X = Cl, Br, I$) crystals adopt a cubic phase already at RT and only experience phase transitions at low temperatures.³⁸

2.2.2 Optoelectronic Basics of Bulk Perovskites

The band structure of a SC is crucial for understanding its possibilities in energy conversion applications. The assignment of a band structure is not a straightforward process and is usually governed by a theoretical approach. One of the most established ways to determine a band diagram is using density functional theory (DFT). LHPs are typically considered to be direct bandgap SCs. The bandgap is

located at the R point in the BZ, as can be seen, exemplary for CsPbBr₃ in Figure 2.8 a. The shown band structure was obtained from DFT calculations assuming a cubic structure. A look at the DOS gives insight into the composition of the bands. VB and CB are formed through the hybridization of Br and Pb orbitals (see Figure 2.8 b). The main contribution to the conduction band is from X p and Pb 6p, while for the valence band, it comes from X p and Pb 6s orbitals. The CB exhibits a p-like character while the VB displays an s-like character, contrary to typical inorganic SCs (see Figure 2.8 a).^{39–41}

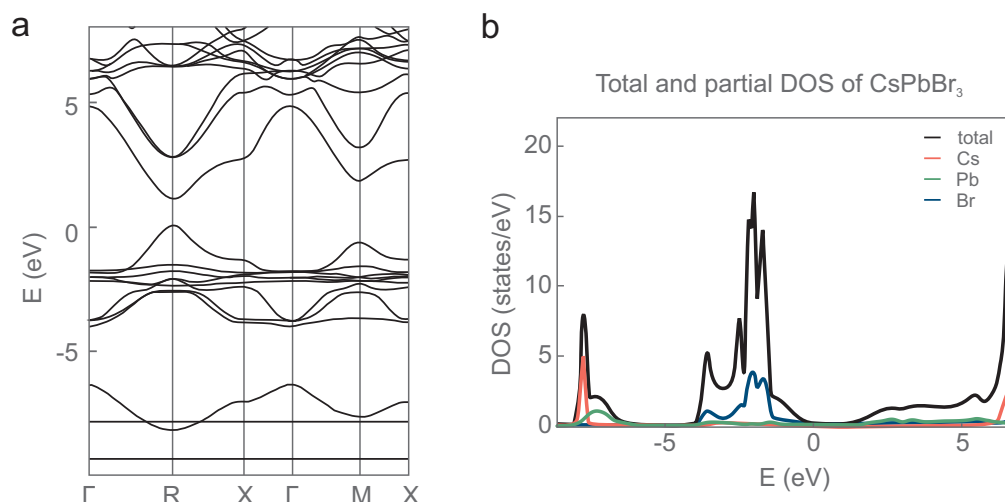


Figure 2.8: Band Structure and Partial Density of States CsPbBr₃ (a) Electronic band structure of CsPbBr₃ obtained by DFT calculations. (b) Total and partial DOS for CsPbBr₃. The impact of the halide ion on the band gap is given by the amount of energetic states near the band edge. The partial DOS for cesium shows that the A-cation has no large influence on the band-edge states. Adapted from Reference [41].

It follows that the bandgap can easily be tuned by varying the halide composition in the perovskite. Additionally, it can be seen that Cs does not contribute to near band edge states (see Figure 2.8 b, PDOS of cesium). Hence, it is sufficient to calculate the DOS near the bandgap with only the contributions from lead and halide states. While CsPbBr₃ has a bandgap of 2.4 eV, the hybrid organic-inorganic LHP MAPbI₃ has a bandgap of around 1.51 eV, the corresponding bromide perovskite (MAPbBr₃) has a bandgap around 2.22 eV, and the chloride variant MAPbCl₃ has a value of around 3.11 eV.^{41–43}

The band structure is the basis for the optoelectronic properties of perovskites. A simplified version of the band structure of MAPbI₃ is shown in Figure 2.9 a together with its correlating absorption spectrum (Figure 2.9 b). A sharp absorption onset is visible at around 1.6 eV in the spectrum, indicating the bandgap energy at the R point. The colored arrows indicate interband transitions at different \mathbf{k} values from the VB to the CB. The flat band allows the facile absorption throughout the visible light spectrum, indicating the quality as an absorber. This is one of the many reasons why perovskites are considered an excellent absorber material for light-harvesting applications.⁴⁴

The absorption onset and the PL emission can easily be tuned by changing the halide ion as described in the previous paragraph. With the dependence of the VB edge on the halide, almost any desired bandgap energy in the visible energy spectrum can be realized by combining different halide ions. Additionally, quantum confinement effects can be used to adjust the bandgap energies. Due to their composition and electronic structure, LHPs are generally accepted as defect tolerant. Defects are omnipresent in all crystals on atomic and macroscopic scales. They can be point defects like vacancies or dislocations of the structure. The term defect tolerant thereby describes a structure that retains its band structure even in case of high defect concentrations. Defects, in general, induce additional energetic states in

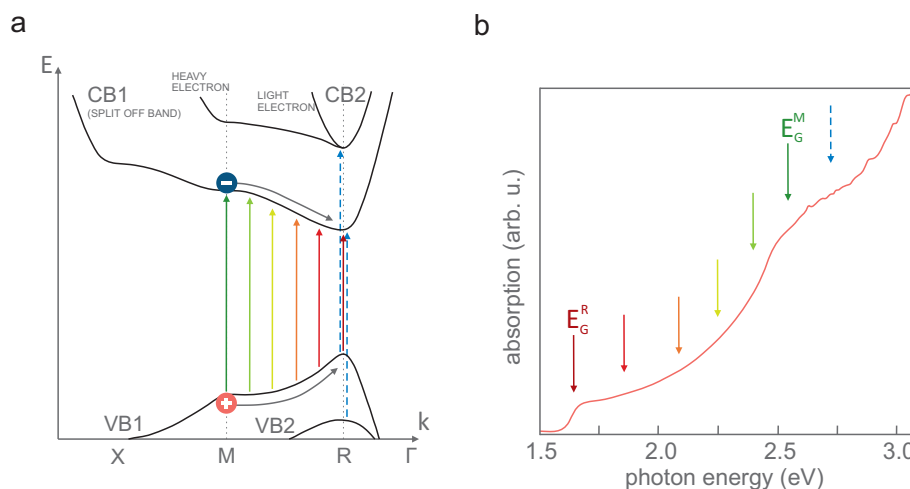


Figure 2.9: Electronic Band Structure of Lead Halide Perovskites (a) Electronic band structure of MAPbI₃ bulk crystals obtained by DFT calculations. The band gap energy is defined at the R point, between the bands VB1 and CB1. Colored arrows indicate possible photoinduced transitions. Blue dashed arrows indicate further dipol allowed transitions including higher bands. (b) Absorption spectrum of MAPbI₃ with arrows corresponding to the colored transitions in (a). Adapted from Reference [44].

the band structure, which increase the non-radiative recombination rate. In LHP, these trap states are generally located near the band edges or within the band, forming so-called shallow traps. Especially at RT, shallow traps do not greatly influence the material and its properties.^{45–47}

2.2.3 Perovskite Nanocrystals

The interest in NC research was sparked by discovering quantum-size effects in nanometer-sized SCs in the 1980s.^{48,49} Generally, a NC is characterized by the size of the crystal, which is in at least one dimension in the quantum confinement regime, usually in the range of a few nanometers. One of the first mentions of perovskite NCs was a report in 2011 of nanometer-sized MAPbI₃ crystals as absorber material in a photovoltaic application.⁵⁰ In 2014 Schmidt et al. published the first solution-based colloidal synthesis approach for MAPbBr₃ NCs⁵¹ followed by Protesescu et al. in 2015 presenting a colloidal synthesis for monodisperse CsPbX₃ NCs.¹¹ They found three outstanding properties inherited by LHP NCs: firstly, the LHP NCs showed a remarkably high PLQY without any post-synthetic treatment. Secondly, LHP NCs could be synthesized with very narrow emission spectra (full width at half maximum (fwhm) <100 meV), which makes them excellent candidates for any light emitting application. Thirdly, similar to bulk LHPs, the emission is tunable through the visible spectrum by mixing different halide ions. These outstanding properties along with simple solution-based syntheses have drawn researchers to LHP NC research.

LHP NCs have been realized in a vast variation to this date. The morphologies of NC can be different, in the past, nanocubes (3D/0D),^{11,52} nanoplatelets (2D)⁵³ and nanowires (1D)^{54,55} have been realized. All different shaped nanocrystals share one important attribute. LHP NCs do not exist as themselves but with an organic ligand layer. The organic ligands are part of the synthesis process and often determine the shape and size of NCs. Additionally, they are necessary to ensure a stable NC dispersion as they prevent the assembly and fusion of multiple LHP NCs. The most common ligands in LHP chemistry are oleic acid and oleylamine.

Synthesis

Much energy has been used to develop reliable and efficient synthesis approaches for LHP NCs. For nanomaterials, two main strategies can be employed. A synthesis can be either a 'bottom up' or a 'top down' approach. Top down strategies use macroscopic crystals and break them down into smaller sizes by mechanical forces or chemical processes. Top down procedures often yield inhomogeneous products and are therefore not of much interest for LHP-based application.⁵⁶ 'Bottom up' approaches generally take advantage of physical or chemical forces resulting in a self-organization of a molecular or atomic system. Especially, liquid phase bottom up approaches have proven themselves as ideal candidates for the synthesis of colloidal LHP NCs. In perovskite research, two main strategies have established themselves: (i) the so-called hot injection method and (ii) the ligand assisted reprecipitation (LARP) method. The underlying principles of both will be briefly presented in the following to introduce perovskite syntheses and their challenges.^{56,57}

Hot injection syntheses were already well known before the interest in LHP NCs, having been developed in the 1990s for the fabrication of cadmium chalcogenide NCs.⁵⁸ The hot injection process is based on the rapid injection of a precursor into a hot solution containing other precursors and ligands dissolved in a high boiling solvent. The synthesis can be separated into a nucleation and a growth stage. The nucleation starts immediately after injection resulting from a state of supersaturation. As the number of monomers is limited and decreases steadily during nucleation, this monomer depletion quickly ends the nucleation stage, after which the existing nuclei continue growing, but no additional nuclei are formed. This leads to a NC population with a narrow size distribution, provided the synthesis is stopped during the growth stage.⁵⁹ To control the size and shape of NCs, several parameters can be tuned, namely the ligand concentration, the type of ligand, the precursor ratios and concentrations, and the injection temperature of the precursor solutions. The colloidal synthesis approach by Protesescu et al. uses equal amounts of amine and acid ligands together with a lead halide in octadecene. By adding cesium oleate (Cs-oleate), they obtain monodisperse CsPbX₃ nanocubes. The size (4-15 nm) of the NCs can be adjusted by the reaction temperature (140-200 °C).¹¹ Organic-inorganic LHPs can be synthesized by exchanging Cs-oleate for a methylamine solution as presented in Reference [60]. Various shapes and sizes can be synthesized by the hot injection method. A variety of compositions of different sized nanoplatelets as well as different sized nanocubes have been reported. Hot injection methods possess two major drawbacks. Usually, hot injection syntheses are conducted under inert conditions using a Schlenk setup due to oxygen and water-sensitive precursors. This makes the synthesis process more complicated and susceptible to mistakes. Additionally, this process is not easily scalable to large product quantities since an increasing injection volume hinders the maintenance of the reaction temperature resulting in inhomogeneous products.¹¹ To circumvent this problem, comparable one-pot syntheses have been developed. As the name suggests, all precursors, ligands, and a solvent are mixed, and the reaction is induced by external heating (heating mantle, ultrasonication⁵² or microwave irradiation⁶¹). Nevertheless, these alternative methods suffer from limited size and shape control and often require post-synthetic purification and size selection steps.

Another common technique for fabricating LHP NCs is the LARP process. It is based on supersaturated recrystallization, which is a process that was used for thousands of years and is still used to harvest salt.⁶² In general, ions are dissolved in a solvent until an equilibrium concentration is reached. The solution is then shifted into a nonequilibrium state of supersaturation, for example, by evaporating the solvent, varying the temperature, or adding an antisolvent. The supersaturation induces spontaneous

precipitation of crystals until an equilibrium is reached again. This strategy was already employed to fabricate organic nanoparticles and polymer particles.^{63,64} In case of LHP NCs, ligands are introduced into the process, hence the term 'ligand assisted reprecipitation'. For LHPs, typically, precursor salts (lead halides and A-cation halides) are dissolved in a polar solvent (DMF, DMSO,..) and dropped into a nonpolar solvent (usually toluene or hexane) with ligands. Mixing both precursor solutions instantly results in a supersaturation state, hence, nucleation and growth of particles will start immediately.⁶⁵ Different shapes and morphologies can be achieved by varying precursor ratios as well as the type of solvents and ligands.^{66,67} Contrary to hot injection methods, LARP can be conducted in ambient atmospheres and is therefore much easier to upscale and less prone to mistakes. Nevertheless, LARP methods introduce other challenges for LHP nanocrystals. The introduction of a polar solvent can cause defects and degradation in the NCs due to the precursor salt-solvent interactions. This is the reason for the limited stability and poor optical properties of LARP-based NC samples.⁶⁸ Additionally, LARP processes do not yield the same control over the shape and size of the NCs as hot injection methods due to uncontrolled nucleation and growth stages.^{69,70}

Bohn et al. developed a synthesis routine for inorganic LHP nanoplatelets (NPLs) with a tunable emission between 435 and 497 nm based on a LARP process.⁷¹ The RT wet synthesis provides CsPbBr₃-based NPLs with a monolayer precise thickness tunability. Thereby, one monolayer corresponds to a unit cell size, roughly 0.6 nm. The synthesis takes advantage of the quantum confinement effect in one dimension to achieve different emission colors (see [Figure 2.10 a](#)). The synthesis is based on reprecipitation mechanisms while determining the thickness by controlling the molar ratio of precursors. During the synthesis, Cs-oleate is injected into a PbBr₂-ligand-solution comprising oleic acid and oleylamine as ligands. An antisolvent, acetone, is added after 5 s to induce NPL formation. After 60 s of vigorous stirring the reaction is terminated by centrifugation at 1800 g for 3 min. The supernatant is discarded and the sediment redispersed in 2 ml hexane. The ratios of PbBr₂-ligand-solution, Cs-oleate, and acetone determine the thickness between 2 and 6 octahedral layers (from now on called monolayers (ML)). Absorption spectra of the samples feature a prominent excitonic peak induced through confinement in one direction. Quantum confinement effects are responsible for the blueshift of the usually green emission of CsPbBr₃ to various blue tones. PL spectra show that each thickness can be directly assigned to a specific emission wavelength with a narrow and color pure peak. The strong quantum confinement in NPLs is the source of the unique properties of this material. The exciton binding energies in NPLs are reported to increase with decreasing NPL thickness up to around 280 meV, making these promising emitters for LEDs. In a first experiment, the implementation of NPL emitters in an LED showed promising results ([Figure 2.10 b](#)).

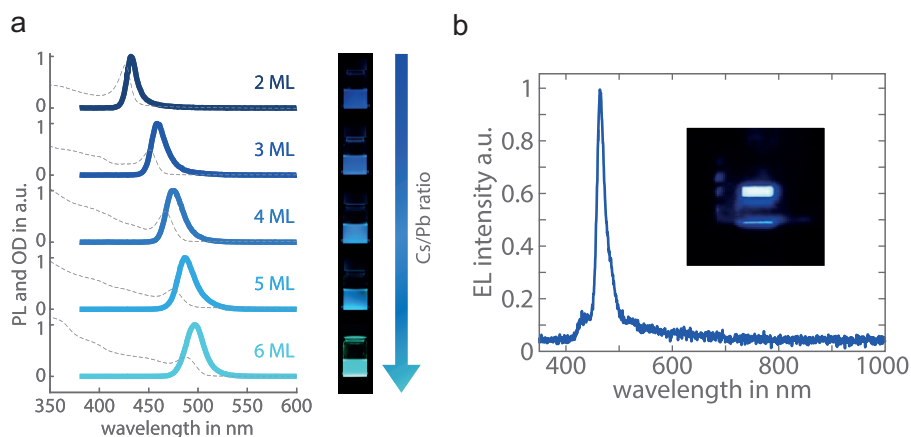


Figure 2.10: Photoluminescence and Absorption Spectra of CsPbBr₃-based Nanoplatelets (a) Photoluminescence (blue lines) and absorption (dashed gray lines) spectra of CsPbBr₃-based NPLs of different thicknesses. A redshift from 432 nm (2ML) to 497 nm (6ML) can be ascribed to decreasing quantum confinement effects. The panel in (a) displays respective NPL dispersions under UV-illumination. The different thicknesses and emission properties are achieved by a variation in the Cs/Pb ratio. (b) Electroluminescence (EL) spectrum of a LED fabricated with 3ML NPLs. The inset shows an image of the corresponding device. Adapted from Reference [71].

The role of ligands

As mentioned before, LHP NCs are passivated by organic ligands. Commonly used is a binary ligand system consisting of aliphatic carboxylic acids and primary amines of various chain lengths. The most common one is oleic acid and oleylamine (see Figure 2.11). In a nonpolar solvent like toluene, the ligand mixture undergoes a reaction leading to the protonation of oleyl amine by oleic acid. One reason for the necessity of organic ligands is the insolubility of PbBr₂ in nonpolar solvents. By introducing the ligand system, the metal salt can easily be dissolved and integrated into a wet synthesis. Another reason for incorporating ligands in NC chemistry is their ability to provoke growth in different NC morphologies. While oleic acid is sufficient for the growth of isotropic nanocubes, the presence of oleylammonium is shown to be essential for anisotropic structures.⁷² The protonated oleylammonium competes with Cs⁺/MA⁺ for the A-cation lattice site in the crystals leading to the potential prevention of further growth on the passivated crystals facet. The absence of oleylamine prevents anisotropic growth, and only cubic nanocrystals can be synthesized.^{73,74} Furthermore, different lateral sizes and thicknesses can be achieved by the correct ligand mixture and ratio. Micron-sized CsPbBr₃-based nanosheets with a controlled thickness of a few nanometers have been produced with short and long chain ligand combinations.^{72,75–77}

Nevertheless, the necessary amount of ligands is based on a delicate thermodynamic equilibrium. The perovskite structure can be affected dramatically by either too few ligands, as is often the case for diluted samples, or too many ligands. The introduction of too many ligands (acid and amines) supports the formation of the lead-poor hexagonal Cs₄PbBr₆ species and fragmentation into smaller crystals. Furthermore, the binary ligand system enables the complete dissolution of LHPs, which could be detrimental to the sample upon higher dilution. Too few ligands will lead to desorption of ligands on the NC surface and disintegration of the structure. Non-passivated surfaces can aggregate and fuse to form uncontrolled crystal clusters. To further enhance the stability of samples and prevent desorption of ligands, it might be useful to introduce ligands with higher binding energy or a kinetic

barrier for ligand detachment like DDAB or zwitterionic ions, which can attach at two different sites at the crystal.^{78–80}

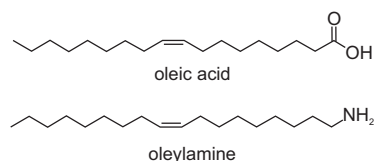


Figure 2.11: Typical Organic Ligands for Perovskite Nanocrystals Chemical structure of the most often used organic ligands oleic acid and oleylamine. In a thermodynamic equilibrium, oleylamine often is protonated by oleic acid.

Post-synthetic treatments

To enhance and optimize the optical properties and the stability of LHP NCs, it is convenient to implement a post-synthetic treatment. The introduced treatments can be used to alter the surface, shape, and phase of LHPs. The whole range of modifications is extensive and lies far beyond the scope of this thesis. Hence, only surface treatments and anion-exchange processes will be introduced. The surface of NCs is per se a defect, as the crystal structure terminates here and not all ions can be satisfied with bondings like in the internal volume of a NC. Ligands usually passivate the surface of a NC by interacting with surface ions and vacancies. The weak binding of the ligands creates a dynamic system of binding and desorbing ligands. Especially during purification steps, ligands are often removed from the sample, which leads to less passivated and more unstable NCs. Since the most prominent surface defect in LHP is a halide vacancy, it is common to add a lead halide ligand mixture to prepared NCs. The excess of halides will lead to defect passivation resulting in less non-radiative recombination enhancing the optical properties. This process is schematically depicted in [Figure 2.12 a, b](#). Simultaneously, the ligands will help to stabilize the NCs in dispersion.^{77,81} Bohn et al. provide such a strategy to enhance optical properties by surface defect repair. The process requires a post-synthetic treatment with a so-called 'enhancement solution' consisting of PbBr_2 and ligands dissolved in hexane. By redispersing the sediment in an enhancement solution instead of pure hexane, the PLQY of NPLs could be enhanced to up to 75% (see [Figure 2.12 c](#)).

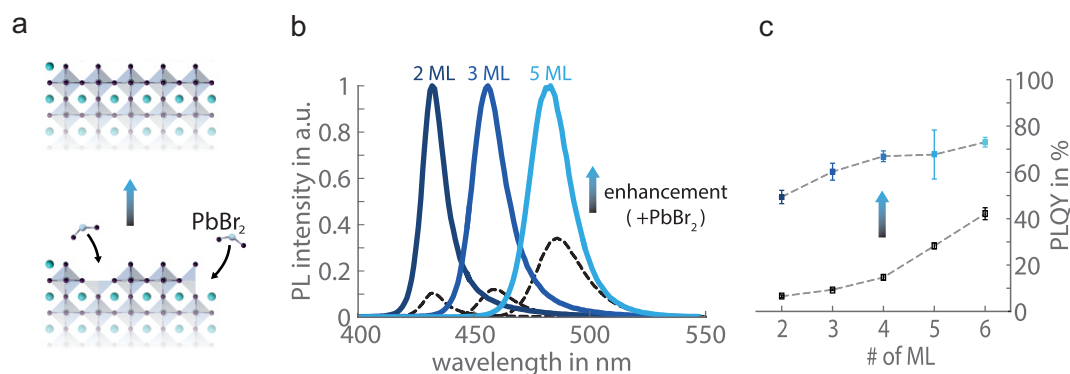


Figure 2.12: Enhancement of CsPbBr_3 -based Nanoplatelets (a) Schematic representation of defect passivation by additional PbBr_2 . The ions fill vacancies on the NC surfaces. The effect of the 'enhancement solution' on PL spectra is shown in (b), an immediate increase in PL intensity is observed, with the emission maxima remaining spectrally constant. (c) The treatment with enhancement solution drastically improves the PLQY as shown in (c). A PLQY increase of at least 30% is observed for all samples. Adapted from Reference [71].

As described in [Subsection 2.2.2](#), the VBM and consequently the emission color of LHP NCs, can easily be tuned by varying the halide composition. Synthesis procedures often allow only a limited variation in the composition. A post-synthetic halide ion adjustment is therefore effective for fine-tuning the optical properties. A minimum requirement for ion exchange in a structure is the mobility of the ion species. The halide ion mobility in the perovskite structure is extraordinarily high due to the high intrinsic concentration of halide vacancies. Due to the high ionic conductivities, it is sufficient to expose LHP NCs to a halide source to induce the ion exchange. This can be done in liquid or dry phase. Astonishingly, exposure to a halide vapor also results in a changed composition.^{82–88}

2.2.4 Challenges for Industrial Applications

Despite their excellent optoelectronic properties and variability of LHP NCs, one of the biggest concerns about them is their long-term stability. The unstable nature and sensitivity to environmental factors hinder industrial relevance and long-term application. Oxygen, moisture, heat, and UV radiation can induce irreversible degradation of the perovskite structure by interacting with the ionic constituents: The hygroscopic nature of A-cations can cause irreparable damage to the crystals through hydrolyzation by exposure to a minimal amount of water. The presence of oxygen, especially in combination with light exposure (UV radiation), can promote the formation of oxides and other stable molecules in the structure. Heat and light exposure induce mobility and solvation of ions and support the formation of elemental lead (Pb_0) particles as well as undesired phase transformations. These are only a limited amount of possible reactions, in nature, external factors often occur in combination, and the resulting damage can be amplified. Already partial degradation can have detrimental effects on the performance of LHPs in devices. Hence, post-synthetic mechanisms are often applied to prevent degradation. The use of encapsulation or embedding of NCs in inert matrices shows a vast improvement in NC stability, but the optical properties of the perovskite are often negatively affected.^{12–14,89,90} Another essential factor considering the stability of LHP NCs is their high ion mobility, as described in the previous section. Especially halide anions are prone to move through the crystal, which could lead to a deviation from the regular ABX_3 stoichiometry. A deficiency of halide ions can alter the perovskite structure and promote the formation of lead nanoparticles.¹⁴ In devices, the accumulation of ions on one contact can cause damage to the whole device structure. Furthermore, in mixed halide perovskite samples, a local demixing of the halide ions can occur, causing a microphase separation, destroying the optical properties of the sample. This is especially a problem in light emission applications as it limits the tunability of emission colors. Therefore, suppression of ion mobility is desired for most applications. Besides their sensitivity towards external forces, LHP NCs suffer from a stability problem originating in their synthetic routine. As introduced in a previous paragraph, NCs are passivated by an organic ligand layer. As their binding to the NC surface is only a weak polar interaction, they are subject to a dynamic equilibrium of binding and detaching from the surface. As a consequence, a suitable ligand concentration preserving the equilibrium is crucial for the long-term stability of a NC dispersion. Too little or too many ligand molecules can cause the transformation into larger NCs by fusion of single NCs or the fracturing into smaller particles by intercalation in the structure, respectively. Additionally, organic ligands hinder the application of LHP NCs in light emitting devices due to their isolating structure. A thin film of LHP NCs can contain up to 30 vol% organic ligand material, which is detrimental for electrical applications.^{77–79} Different approaches have been developed to overcome some or all of these issues. They include device and

single crystal encapsulation, different coatings, and embedding in inert matrices. However, each method provides its own drawback by either affecting the LHP properties or introducing additional challenges for applications.^{91–94}

Despite their stability and application problems, LHPs possess another inherent obstacle, as they contain lead. Lead, a heavy metal, is known to enter the human blood system through ingestion, inhalation, or skin contact. It thereby mimics essential elements like calcium, zinc, and iron and blocks essential enzymes and receptors. The similarity of Pb^{2+} with Ca^{2+} enables lead to pass the blood-brain barrier and accumulate in the brain. Generally, heavy metals have been shown to damage organs and genetic material and promote severe diseases. Considering the duration of lead accumulation in biological systems, even exposure to small amounts of heavy metals should be avoided. Consequently, lead-free alternatives are desired and required for future applications.^{15,16,95}

Boosting LHP NC stability - Diblock Copolymer Micelles as Nanoreactors

An alternative bottom-up synthesis approach for nanoparticles to overcome stability problems is the application of nanoreactors. The usage of nanoreactors allows to abandon organic ligands. The confined space of nanoreactors limits the growth of a nanoparticle to a suitable size. Polymers have proven themselves as suitable candidates for this. The term polymer generally describes a molecule formed by the repetition of a single unit. If the type of subunit remains the same, the molecule is called a homopolymer. In the case of two or more different subunits, the polymer is specified as a copolymer. The arrangement of polymers can be unsystematic, giving a random copolymer. In block copolymers, however, the subunits arrange in blocks. Each block is a continuous repetition of a single monomer. The chemical differences (e. g., polarity, solubility) of the building blocks lead to a great versatility for applications involving catalysts, medicine, and biology. Building blocks can be arranged in different ways. The simplest arrangement is a linear polymer consisting of two chains, the so-called diblock copolymer. Block copolymers with more building blocks in linear, dendritic, starlike, or cyclic structures have been reported. Diblock copolymers are most often synthesized with living anionic polymerization. The synthesis was discovered by Swarc et al. in 1956 and can be applied to various building blocks like styrenes, dienes, or lactones.⁹⁶ The polymer is built through the sequential addition of monomers to the first block. Undesired side reactions during the synthesis can be suppressed by selected chemical protection.⁹⁷ The building blocks in diblock copolymers are generally immiscible but the fact that the building blocks are covalently bonded to each other leads to a spatially limited microphase separation in the range of 10 to 100 nm. Throughout this thesis, the chosen diblock copolymer is a polystyrene (PS) and poly(2-vinyl pyridine) (PVP) compound (see [Figure 2.13](#)). PS and PVP are linked with a covalent bond. In the following, the polymer will be denoted as PS(n)-PVP(m), with n and m describing the number of monomers within each polymer chain.^{56,98}

Depending on the chemical environment, diblock copolymers (in further reading referred to as polymers) can adapt different phases. In order to use them as nanoreactors, an arrangement of micelles is desired. The formation of micelles was first reported for rubber in 1958 by Merrett.⁹⁹ Polymer micelles the focus of several theoretical and experimental studies.^{100–102} Micelle formation is a self-assembly process occurring due to different solubilities of PS and PVP. To induce micellization, the critical micelle concentration (CMC) needs to be exceeded, only then polymers will start to aggregate. Thereby, the number of free polymers (unimers) in the solution remains constant. Several milligrams

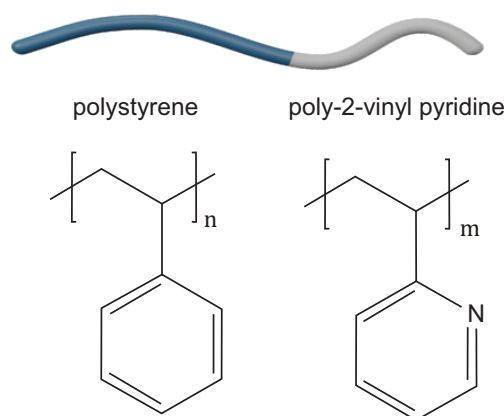


Figure 2.13: Polystyrene-Polyvinyl pyridine Diblock Copolymer The block copolymer used in this thesis comprises a linear arrangement of n units of polystyrene (PS) and m units of poly-2-vinyl pyridine (PVP).

per liter are sufficient to exceed the CMC for most polymers.¹⁰³ Micellization is driven by different forces to form an energetically favorable structure. On the one hand, there is the aggregation of less soluble PVP chains due to attractive forces in between them. On the other hand, there is the repulsion of the soluble PS blocks. Finally, the micelle consists of a PVP core and a soluble PS shell. Polymer micelles have been used as nanoreactors to fabricate metal nanoparticles for many years. The core-shell structure of PS-PVP polymer micelles in toluene allows a selective dissolution of polar precursors. The interaction of metal salts and the PVP chain further stabilizes the polymer micelle by increasing the insolubility of the PVP-ion core in toluene, and consequently, the CMC decreases for ion-filled polymer micelles. In addition to their nanoreactor properties, polymer micelles exhibit another unique capability. Polymer micelles can easily be arranged in highly ordered monolayers in thin films. They adopt a quasihexagonal pattern upon dip- or spin coating. The driving forces during the self-assembly process in macroscopic patterns are attractive capillary forces and electrostatic and steric interactions.⁵⁶ The process of micellization and self-assembly in ordered thin films is schematically depicted in [Figure 2.14](#).

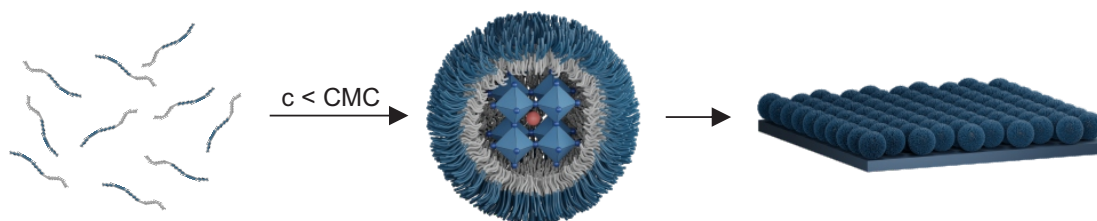


Figure 2.14: Micellization and Micelle Films If the concentration of the polymer surpasses the CMC, polymer chains assemble in micelles comprising a PVP core and a PS shell. Upon dip coating or drop casting, micelles arrange in a quasi hexagonal pattern in a monolayer on a substrate.

Overcoming the Toxicity of Lead - Lead-Free Perovskite NCs

Their biggest drawback must not be neglected while talking about LHPs and their suitability as optoelectronic material. The basis is still lead, a toxic heavy metal known to accumulate in biological systems. A more environmentally friendly alternative with comparable properties is necessary to match the modern world's requirements. Different strategies to eliminate lead from the perovskite

structure have been attempted. The most obvious one is the replacement of lead with its lighter group IV analogs tin and germanium.^{104,105} The first colloidal synthesis of lead-free (LF) perovskite NCs was reported in 2016 by Jellicoe et al.,¹⁰⁴ followed by Wang et al.¹⁰⁵ Both presented CsSnX₃ (X=Cl, Br, I) NCs prepared by a hot injection method. Different emission wavelengths, as well as NC morphologies, have been realized. Comparable germanium compounds were reported in 2018 by Wu et al.¹⁰⁶ However, group IV compounds usually suffer from poor stability as tin and germanium are prone to oxidization from 2+ to 4+ states.^{95,107}

Another approach is the so-called 'cation transmutation', thereby two lead cations are substituted with a monovalent and a trivalent cation to match charge neutrality.¹⁰⁷ The resulting quaternary system with the formula A₂C⁺D³⁺X₆ is denoted as a double perovskite (DP). The structure of DPs shows alternating octahedra centered by C and D cations, respectively. The unit cell of DPs consequently expands to eight corner-sharing octahedra (Figure 2.15).^{95,107} The introduction of a fourth ion in the perovskite structure also demands an adaption of the well-known Goldschmidt factor while keeping the boundaries (see Equation 2.15):^{95,107}

$$t = \frac{r_A + r_X}{\sqrt{2} \left(\frac{r_C + r_D}{2} + r_X \right)} \quad (2.16)$$

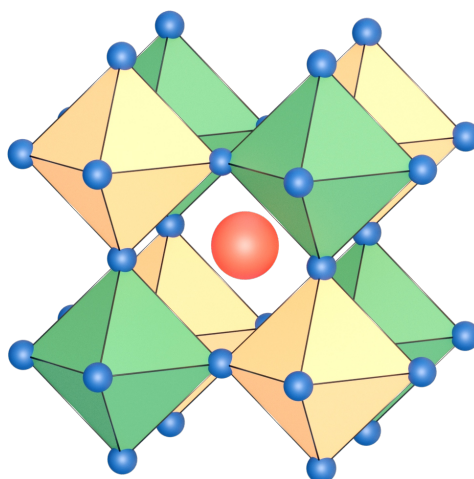


Figure 2.15: Double Perovskite Structure The crystal structure of a DP A₂C⁺D³⁺X₆ is built of alternating octahedra centered by C (green) or D (orange) cations. X-anions are shown in blue, red represents the A-cation position.

The requirements of the Goldschmidt factor limit the possible candidates for a DP structure. Theoretical approaches found the most promising compounds with group 1 and 11 elements as monovalent cations and group 13 and 15 elements as trivalent cations. However, DFT calculations revealed indirect bandgaps for all tested compounds. Hence, bandgap engineering and property tuning in LFDP are achieved by doping and alloying. Different synthesis routes have been developed to fabricate LFDP NCs. The first LFDP Cs₂AgBiBr₆ NCs were synthesized in 2018 by hot injection methods. One process uses metal acetates as a cation source and a trimethylsilyl halide as an anion source.¹⁰⁸ Simultaneously, a synthesis routine based on metal nitrates, metal halides, and hydrogen bromide as ion precursors was developed. A minimal number of alternative synthesis methods have been reported until now. Since 2016 different LARP strategies for ternary LF perovskite compounds were presented but are not established in the research for LFDP.^{109–111}

One chapter of this thesis will present a novel synthesis routine for $\text{Cs}_2\text{NaBiCl}_6$ NCs including a tunable Mn doping process. Therefore this compound will be discussed in detail. $\text{Cs}_2\text{NaBiCl}_6$ exhibits a large indirect bandgap of 3.4 eV.¹¹² Despite its less than ideal optical properties, it is highly flexible regarding the ability to incorporate dopants in the structure. A successful doping with manganese was reported by Majher et al in 2019.¹¹² The emission of $\text{Mn}:\text{Cs}_2\text{NaBiCl}_6$ thereby is dominated by a d-d transition of manganese as a color center. The emission wavelength is found to be around 590 nm in macroscopic crystals. NCs of the pristine and doped compounds can be achieved by the same hot injection methods by varying the temperature. It was found that below a reaction temperature of 170 °C cubic NCs are formed while above 170 °C, cuboctahedral shapes are observed.¹¹³ The absorption spectrum of $\text{Cs}_2\text{NaBiCl}_6$ NCs shows a characteristic excitonic peak around 325 nm, associated with the heavy bismuth cations (see Figure 2.16 a, c dashed lines).^{113–115} The PL spectra of different reported $\text{Cs}_2\text{NaBiCl}_6$ NCs open some questions. On the one hand a $\text{Cs}_2\text{NaBiCl}_6$ emission around 375 nm is reported by Reference [114] on the other hand Reference [115] shows an emission peak around 425 nm (see Figure 2.16 a, c bold lines). Upon manganese doping, a broad emission around 585 nm with a PLQY in up to 3 to 5 % is reported.^{114,115}

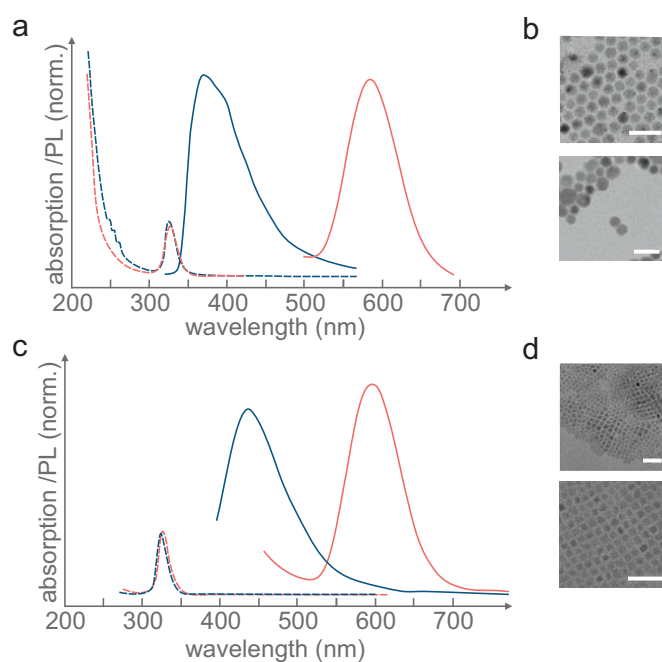


Figure 2.16: Reported Properties of $\text{Mn}:\text{Cs}_2\text{NaBiCl}_6$ Nanocrystals Different synthesis approaches for $\text{Mn}:\text{Cs}_2\text{NaBiCl}_6$ have been shown in literature. (a) and (b) show data published by Yao et al.¹¹⁴ Blue lines correspond to absorption (dashed lines) and PL spectra of undoped $\text{Cs}_2\text{NaBiCl}_6$, red lines correspond to a Mn doped species. TEM images of the undoped and doped species are displayed. (c) and (d) show comparable figures for data published by Han et al.¹¹⁵ Scale bars correspond to 50 nm. Adapted from Reference [114] and Reference [115].

However, most LFDPs are fabricated by hot injection methods requiring high temperatures and an inert atmosphere. The disadvantages of hot injection methods discussed in Subsection 2.2.3 also apply to the fabrication of LFDPs. This limits the large scale production and accessibility to LFDPs for potential applications.¹⁰⁹

2.3 Computational Methods in Nanocrystal Research

A novel approach in nanocrystal research is the utilization of computational methods. Machine learning technology has rapidly entered many research fields and opens new opportunities to discover and test new materials. Traditionally, new materials have been developed by trial and error until the properties match the expectations. This method is time consuming, not purposeful, and potentially expensive. To find correlations between material properties and the structure, simulation methods like DFT, Monte Carlo simulations, and molecular dynamics are already well established.¹¹⁶⁻¹¹⁸ However, they are often highly specified for a certain material or property and only hard to apply to new systems. Additionally, some of these methods require high computational capacities and professional skills. In recent years, artificial intelligence-based processes have made their way into scientific research.¹¹⁹ Machine learning is a powerful tool to extract information from existing data, learn from it and design new materials. Machine learning is successfully used throughout material science, e.g. in superconductor or photovoltaic materials research.^{120,121} In general, machine learning combines engineering, statistics, and computer science to form an artificial intelligence. The main application of machine learning is to evaluate existing data and predict new outcomes after a training process. This is especially useful for applications with an infinite parameter space where trial and error methods are infeasible.¹¹⁹ Also in perovskite research machine learning-based processes have been used successfully, for example to estimate lattice parameters,¹²² predict the perovskite's bandgap¹²³ and in the finding of new perovskite compounds.¹²⁴

3

Materials and Methods

In the following chapter, syntheses routines for perovskite nanocrystals and their variations are presented. Different techniques for structural characterization will be described, including transmission electron microscopy, X-ray scattering, and dynamic light scattering to gain insight into different properties. Furthermore, the techniques with which the basic optical properties of the nanomaterials were analyzed, absorption-, and PL spectroscopy and PL quantum yield determination, are explained. Lastly, some computational methods will be introduced, which were used in the scope of this thesis to improve the development of nanocrystal syntheses.

3.1 Nanocrystal Synthesis

All used chemicals are listed in table [Table 3.1](#) and were employed as received.

Table 3.1: Chemicals Required for the Syntheses.

Material	Formula/Abbreviation	Supplier	Purity
acetone	C ₃ H ₆ O	Merck	≥99.98
bismuth (III) acetate	Bi(CH ₃ COO) ₃ /BiOAc ₃	Alfa Aesar	≥99.999 %
cesium carbonate	Cs ₂ CO ₃	Sigma Aldrich	99 %
cesium bromide	CsBr	Alfa Aesar	99.999 %
cesium chloride	CsCl	VWR chemicals	99.9 %
cesium iodide	CsI	Alfa Aesar	99.999 %
formamidineum bromide	FABr	Ossila	99.5 %
formamidineum hydrochloride	FACl	Alfa Aesar	98 %
formamidineum iodide	FAI	Ossila	99.5 %
hexane	C ₆ H ₁₂	VWR chemicals	97 %
iso-propanol	C ₃ H ₈ O/IPA	Merck	≥99.98 %
methylammonium bromide	MABr	Ossila	99.5 %
methylammonium chloride	MACl	Sigma Aldrich	99.5 %
methylammonium iodide	MAI	Ossila	99.9 %
manganese (II) acetate	Mn(CH ₃ COO) ₂ /MnOAc ₂	ACROS Organics	≥98 %
oleic acid	C ₁₈ H ₃₄ O ₂	Sigma Aldrich	technical grade, 90 %
oleylamine	C ₁₈ H ₃₇ N	Sigma Aldrich	technical grade, 70 %
lead(II) bromide	PbBr ₂	Merck	98 %
lead(II) chloride	PbCl ₂	Sigma Aldrich	98 %
lead(II) iodide	PbI ₂	Alfa Aesar	98.5 %
sodium acetate	NaCH ₃ COO/NaOAc	Alfa Aesar	≥99.997 %
toluene	C ₇ H ₈	VWR chemicals	≥99.9 %
trimethylsilyl chloride	(CH ₃) ₃ SiCl/TMSCl	Merck	MQ100
Diblock copolymer	PS(266)-PVP(41)	polymersource Inc	pure
Diblock copolymer	PS(153)-PVP(33)	polymersource Inc	pure
Diblock copolymer	PS(259)-PVP(11)	polymersource Inc	pure
Diblock copolymer	PS(113)-PVP(143)	polymersource Inc	pure
Diblock copolymer	PS(221)-PVP(133)	polymersource Inc	pure
Diblock copolymer	PS(394)-PVP(143)	polymersource Inc	pure

3.1.1 Diblock Copolymer-Templated Synthesis

Basic Synthesis Procedure

Perovskite NCs were obtained in a block copolymer-templated wet synthesis. The polymer ($1.56 \cdot 10^{-6}$ mol) was dissolved in toluene (5 ml) and stirred overnight to ensure the complete formation of the micelles. Lead- and A-cation halides were used as precursors. To grow crystals in the micelles, an A-cation halide (AX, A = Cs, MA, FA; X = Cl, Br, I; $6.40 \cdot 10^{-5}$ mol) was added to the polymer solution and stirred vigorously for 5 hours. Afterwards, a lead halide (PbX_2 , X = Cl, Br, I; $6.40 \cdot 10^{-5}$ mol) was added and the solution was stirred again for at least 24 hours. In case of mixed halides, PbX_2 , AX and AY were used for $\text{APbX}_{3-z}\text{Y}_z$ (A = Cs, MA, FA; X, Y = Cl, Br, I) perovskites with the ratio 3 : z : 3-z. The same approach was used for mixed A-cation samples. For further purification, the suspension was centrifuged for 10 min at 2800 g. The supernatant was subsequently centrifuged a second time for 20 min at 16 000 g. The resulting supernatant was analyzed further.

Ligand-Assisted Synthesis Procedure

Similar to the basic synthesis a polymer ($1.56 \cdot 10^{-6}$ mol) was dissolved in toluene (5 ml) and stirred overnight to ensure complete formation of the micelles. An A-cation halide (AX, A = Cs, MA, FA; X = Cl, Br, I; $6.40 \cdot 10^{-5}$ mol) was added to the polymer solution and stirred vigorously for 5 hours. A lead halide salt (0.1 mmol) was dissolved in toluene (500 μl) with an acid ligand (0.14 mmol) and an amine ligand (0.38 mmol) as the lead precursor. The lead precursor (30 μl) was added into the AX-polymer mixture and stirred for at least 24 hours. The reaction mixture was centrifuged for 10 min at 11 200 g for purification. The supernatant was subsequently centrifuged for 30 min at 16 000 g and further used for characterization.

3.1.2 $\text{Cs}_{n-1}\text{Pb}_n\text{Br}_{3n+1}$ Nanoplatelets

This synthesis is based on the original procedure by Bohn et al.⁷¹ For the synthesis of $\text{Cs}_{n-1}\text{Pb}_n\text{Br}_{3n+1}$ NPLs, three separate solutions are required.

Cs-oleate precursor

Cs_2CO_3 (0.1 mmol) is dissolved in oleic acid (10 ml) at 85°C under continuous stirring for 1h. The precursor is stored airtight under continuous stirring and used for 30 days.

PbBr₂-ligand-precursor

PbBr_2 (0.1 mmol) and 100 μl of each oleic acid and oleylamine are dissolved in toluene (10 ml) at 85°C under continuous stirring for 3 h. The precursor is stored airtight under continuous stirring and used within 48 h and only if no discoloration is visible.

Enhancement solution

PbX_2 (X = Cl, Br, I) (0.1 mmol) and 100 μl of each oleic acid and oleylamine are dissolved in hexane (10 ml) at 85°C under continuous stirring for 3 h. The enhancement solution is stored airtight under continuous stirring and used for 10 days as long as no discoloration is visible.

Synthesis

The synthesis was carried out under ambient atmosphere at RT. All precursors were stored in closed glass vials under continuous stirring. A vial was charged with the PbBr_2 precursor solution and a Cs precursor solution was added under stirring at 1200 rpm. The corresponding volumes for different thicknesses are listed in Table 3.2. After 10 s, acetone (2 ml) was added and the reaction mixture stirred for 1 min. The mixture was centrifuged at 1800 g for 3 min and the precipitate was redispersed in hexane (2 ml). To enhance the stability and emission properties of the NPLs, they were redispersed in a 1:10 dilution of the enhancement solution. Different ratios of hexane and enhancement solution were used for halide ion exchange experiments.

Table 3.2: Precursor Amounts for Nanoplatelets with Different Thicknesses The original precursor and acetone amounts for achieving NPLs of different thicknesses according to Bohn et al. are listed.⁷¹

	PbBr ₂ (ml)	Cs-oleate (μl)	acetone (ml)
2 ML	3	150	2
3 ML	1.5	150	2
4 ML	1.2	150	2
5 ML	1	200	2
6 ML	1	200	2.5

3.1.3 Lead-Free Perovskite Nanocrystals

For the general synthesis of a LFDP with a composition of $\text{Mn}:\text{Cs}_2\text{NaBiCl}_6$, stoichiometric amounts of the metal carbonate and acetate precursors Cs_2CO_3 (0.05 mmol, 1 eq), NaOAc (0.05 mmol, 1 eq), BiOAc_3 (0.05-x mmol, 1-x eq) and MnOAc_x (x mmol, x eq) were dissolved in oleic acid (250 μl) under vigorous stirring at 140 °C on a hot plate until a transparent solution was obtained. After letting the solution cool down to 115 °C, first toluene (2 ml) and then oleylamine (125 μl) were added. This precursor solution was then kept on the hot plate at 115 °C for at least another 15 min to ensure thorough mixing and temperature equalization. Then, it was removed from the hot plate and immediately afterwards TMSCl (0.45 mmol, 9 eq) was injected into the hot solution under vigorous stirring. After 10 s, acetone (4 ml) was added as the anti-solvent and the resulting dispersion was stirred for 1 min before centrifuging it at 11 000 g, for 10 min. The supernatant was discarded. If no further purification was performed, the precipitate was redispersed in toluene (5 ml). Lastly, this dispersion was then centrifuged (1800 g, 10 min) to remove any potential bulk material and the supernatant was used for further analysis.

In case the optional purification protocol was carried out, it was implemented directly after the first centrifugation of the reaction product. Similar to the last step in the ordinary synthesis, the precipitate containing the reaction product was redispersed in toluene (3 ml). Furthermore, small amounts of oleic acid (10 μl) and oleylamine (10 μl) were added. Afterwards, acetone (6 ml) was used to again precipitate the product from the solution, followed by another centrifugation step (11 000 g, 10 min) and subsequent discarding of the supernatant. This procedure constitutes one washing step, and depending on the sample, it was repeated up to a total amount of three times. Then, the precipitate was redispersed in toluene (5 ml) and centrifuged (1800 g, 10 min) to remove potential bulk material in accordance to the proceedings of the not purified samples. Correspondingly, the final supernatant was used for further analysis.

Table 3.3: Precursor Amounts for Lead-Free Double Perovskites Exemplary precursor amounts for Mn:Cs₂NaBiCl₆ with 10% Mn content

Precursor	Amount (mmol)	Amount (mg)	Volume (μl)	Equivalent
Cs ₂ CO ₃	0.050	16.3	57	1.0
NaOAc	0.050	4.1		1.0
BiOAc ₃	0.045	17.4		0.9
MnOAc ₂	0.005	0.9		0.1
TMSCl	0.450			9.0

3.2 Structural Characterization

3.2.1 Transmission Electron Microscopy

Imaging nanocrystals can be quite challenging due to their extremely small sizes. Standard light microscopy is the first method coming to mind regarding imaging. However, due to the restriction of the Abbe limit light microscopy only provides a resolution of around 200 nm:

$$\rho = \frac{\lambda}{n \sin(\alpha)} \quad (3.1)$$

With n being the refractive index of the materials, λ the wavelength of the used light and α the angle of the incoming light. Nanocrystals investigated in this thesis have sizes around 2-40 nm consequently imaging wavelengths of similar scale are necessary. This can be achieved by using accelerated electrons. Their wavelength is significantly smaller than the visible light range according to de Broglie:

$$\lambda_e = \frac{h}{p_e} = \frac{h}{m_e v_e} = \frac{h}{\sqrt{2m_e e U_b}} \quad (3.2)$$

With this method, the resolution limits of an electron microscope can be optimized down to 0.5 nm. A transmission electron microscope (TEM) can be compared with a conventional light microscope. Electrons are generated in a field emission gun, thereby, a strong electric field is applied to extract electrons. They are accelerated through an electric field. The electron beam is defined and focused through different electromagnetic lenses. After traversing through the sample, the electrons are detected either by a fluorescing screen or a charge-coupled device (CCD) camera. Since the detector is situated behind the sample, the transmission of electrons needs to be guaranteed, therefore, the sample cannot be thicker than around 100 nm.²⁰

In this thesis, images were taken on a JEM-1011 by JOEL, provided by the group of Prof. Joachim Rädler. It is operated at an acceleration voltage of 80 kV. Samples were produced on copper grids coated with carbon (1 nm) and formvar (10 nm) purchased from *Electron Microscopy Sciences*. Interpreting TEM images can be challenging due to some factors. Firstly the obtained image constitutes a combination of the internal structure and the surface of the sample; therefore, it can not be distinguished between the surface and inner volume of a crystal. Secondly, the high energy electron beam can impact the sample itself and lead to degradation during illumination.

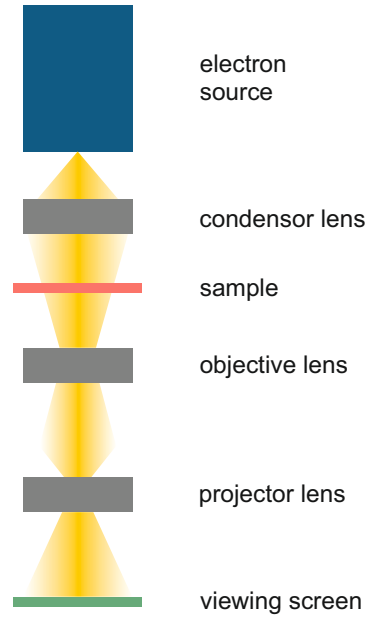


Figure 3.1: Transmission Electron Microscope Schematic representation of a transmission electron microscope

3.2.2 X-ray Scattering

X-ray scattering is a non-invasive method to investigate the different properties of crystals and crystal-like structures. In this thesis, it is used to analyze the structure and size of crystals and the assembly of nanoparticles under different conditions. X-rays were discovered by Wilhelm C. Röntgen in 1895 and their application for diffraction in crystals was found by Max von Laue in 1914. Both discoveries were awarded a Nobel Prize in 1901 and 1914, respectively.^{125,126} Ever since, many different applications and methods employing X-rays have been developed. The basic physical process is the same for all methods and will be briefly introduced in the following. X-ray scattering or diffraction is based on how X-rays, similar to other electromagnetic waves, are diffracted by a grating. Since X-rays can employ comparable wavelengths to the distance in crystal lattices, they can be used to analyze the structure of nanocrystals and ordered structures. The structure of an ordered material is directly related to its characteristic diffraction pattern. This pattern results from constructive and destructive interferences of diffracted X-rays at different angles. Bragg's Law defines the angles under which constructive interference occurs:^{19,20}

$$n\lambda = 2d \cdot \sin \theta \quad (3.3)$$

With the wavelength λ , the half angle θ , the refractive index n and the distance between scattering planes d .

With Bragg's Law and the known wavelength of the X-ray, the spacing d in a crystal structure can be calculated. Together with the peak intensities at different angles, these values can be used to identify a crystal structure or a more macroscopic pattern. While working with X-ray scattering, the critical variable is the scattering vector q which describes the difference between the wave vectors of the incoming and outgoing waves. It is defined as:

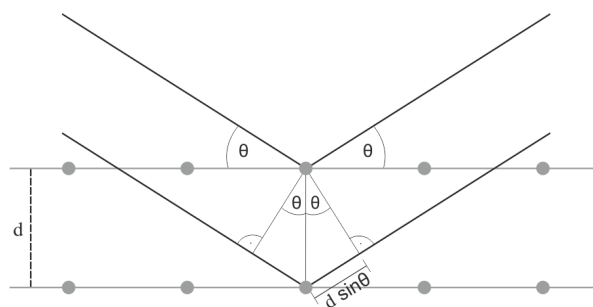


Figure 3.2: Bragg's Law Schematic depiction of X-ray diffraction and Bragg's law

$$|q| = \frac{4\pi}{\lambda} \sin\theta \quad (3.4)$$

With the wavelength λ and the half angle θ .

The methods employed in this thesis are Small Angle X-ray Scattering (SAXS) and Wide Angle X-ray Scattering (WAXS). The essential difference between both techniques is the angle of detection. WAXS corresponds to angles from 1° to 45° , which equals q -values from 0.1 \AA^{-1} to 5 \AA^{-1} , allowing real space analysis of structures of 6 nm to angstrom range. SAXS, on the other hand, is used to investigate larger structures in the range of up to 100 nm with angles smaller than 1° - corresponding to q -values below 0.1 \AA^{-1} . GISAXS and GIWAXS are established methods to investigate nanoparticle thin films, Where 'GI' represents 'Grazing Incidence', indicating a different experimental setup. Thereby the X-ray beam is directed towards the surface of a thin film on a substrate. The angle is controlled using a sample tilt stage and is usually in the range of 0.05° to 0.50° . The beam is efficiently reflected from the sample and substrate surfaces at these angles. This allows a detailed analysis of the sample surface.

Steady-state measurements of SAXS and WAXS were conducted at the in-house setup from PD Bert Nickel. The X-ray source is a molybdenum K_α microfocus source with $\lambda = 0.71 \text{ \AA}^{-1}$. The beam is collimated and focused on the sample placed on a motorized xyz stage. After passing a vacuum tube, the beam is detected by a detector (*Pilatus 300K* or *Pilatus 100K*). The sample detector distance can be varied to choose an appropriate q range. A more detailed description of the setup can be found in [Reference \[127\]](#).

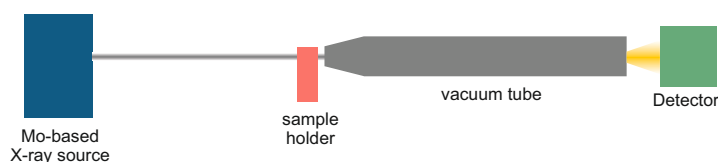


Figure 3.3: Schematic Depiction of the Mo-based Small-Angle X-Ray Scattering Setup A Mo-anode is used to generate X-rays that are collimated onto a sample. Behind the sample, the scattered beam propagates through a vacuum tube and is directed to a hybrid pixel detector. The setup is optimized for SAXS measurements but can also be adapted to fit WAXS measurements. Adapted from [Reference \[127\]](#).

In-situ and degradation measurements were done at the beamlines P62 and P07 at the PETRA III storage ring at the 'Deutsches Elektronen Synchrotron' (DESY). At P62, in-situ SAXS experiments were performed at 20 keV. Different SAXS and WAXS detectors enabled the simultaneous measurement of both methods. To investigate the synthesis process of perovskite NPLs, a setup was developed, which could be installed at the beamlines and controlled remotely. A reaction cell with stepper motor-based syringe pumps, including the possibility to heat and stir, was built. NPL syntheses were conducted

with different parameters and monitored during the process. Additionally, all finished products were measured and analyzed as well as all necessary reference measurements. Details on the beamlines can be found in Reference [128] and Reference [129].

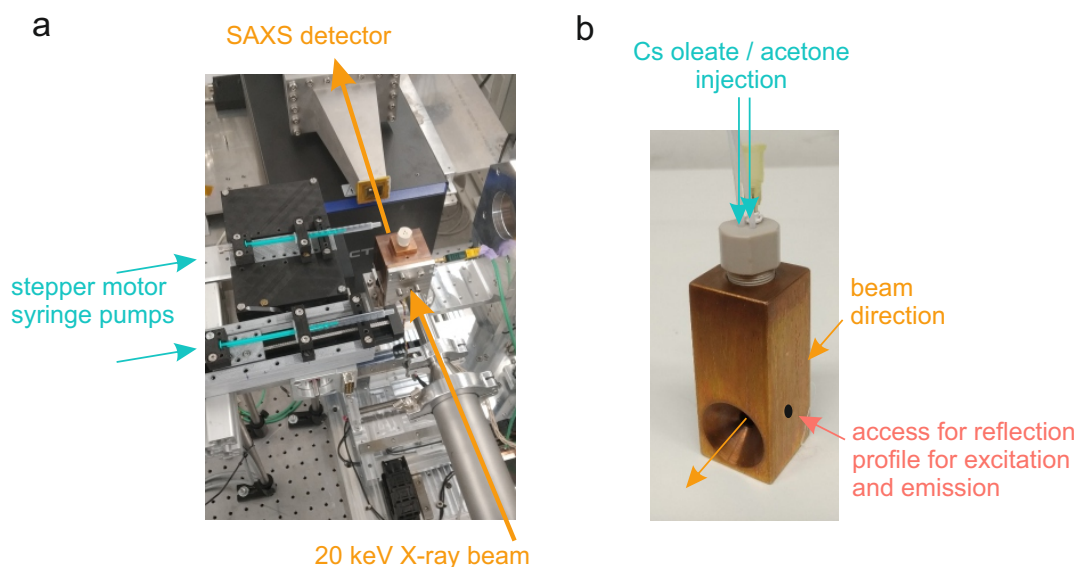


Figure 3.4: Schematic Description of the In-situ Synthesis Setup (a) Photograph of the in-situ cell mounted in the beamline. Two stepper motor-based syringe pumps are used to inject Cs-oleate and acetone, respectively. A 20 keV X-ray beam is used for the experiments and detected on the SAXS detector behind the sample. (b) A glass capillary inside a copper block is used for the synthesis. The X-ray beam direction is indicated by orange arrows. Perpendicular to the beam, a reflection profile can be inserted to excite the sample and simultaneously detect the emission.

The processing of data obtained from X-ray scattering experiments was kindly done by Kilian Frank.

3.2.3 Dynamic Light Scattering

Dynamic light scattering (DLS) is a standard non-invasive technique to measure size distributions of nanoparticle dispersions.¹³⁰ DLS, also called photon correlation spectroscopy (PCS) is based on the interaction of light with nanoparticles. For this, a laser beam passes through a nanoparticle dispersion, and scattered photons are recorded by a detector. Since particles in a dispersion constantly undergo Brownian motion, the intensity of scattered photons will fluctuate. By analyzing the intensity fluctuations, the velocity of the Brownian motion can be calculated. Larger particles move slower, leading to longer intensity fluctuations, while smaller particles result in faster intensity fluctuations. With the Stokes-Einstein equation, the particle size can be calculated from the diffusion coefficient D :¹³¹

$$R = \frac{k_B T}{6\pi\eta D} \quad (3.5)$$

with k_B as the Boltzmann constant, temperature T , viscosity η and the hydrodynamic radius R . It needs to be noted, that the hydrodynamic radius does not refer to the actual particle size but anything affecting the diffusion speed of the particle, including the Debye length, which is an electric double layer of the solvent caused by ionic interactions. DLS is a quick method to determine particle sizes in the range of 0.3 nm to 10 μm . For this thesis, all measurements were conducted on the Zetasizer Pro from *Malvern Panalytical*. The samples were excited with a He-Ne laser ($\lambda = 633 \text{ nm}$) at a constant temperature of 25 °C. 1 ml of the sample was analyzed in 10x10 mm quartz glass cuvettes (*Hellma Analytics*). The input parameters for the measurements are the solvent, the material, and the corresponding refractive index and extinction coefficient.

3.3 Optical Characterization

Absorption and photoluminescence measurements were conducted on a Fluoromax4 Plus (*Horiba*), including the absorption/transmission accessory and an integrating sphere (Quanta- ϕ). The device uses a xenon arc lamp as light source with a spectral range from 300 to 850 nm. A monochromator is used to isolate a desired wavelength range for the excitation. The sample chamber can either be equipped with a holder for 10x10 mm cuvettes or a holder for substrates of various sizes. Optical characterization was done in 10x10 mm quartz glass cuvettes (*Hellma Analytics*) if not stated otherwise. The excitation path is the same for all spectroscopy methods in this device. The detection path will be discussed for each method in the following

Absorption

For absorption, the transmission of light through the sample is measured. The excitation light is directed onto the sample, interacting with the sample. The intensity of the transmitted light is recorded and can be examined from the obtained extinction spectrum and is commonly given as the optical density (OD) of the sample. The correlation is provided by the ratio of the intensity of the transmitted light $I(\lambda)$ to the intensity of the reference sample $I_0(\lambda)$. Since the intensity decreases exponentially

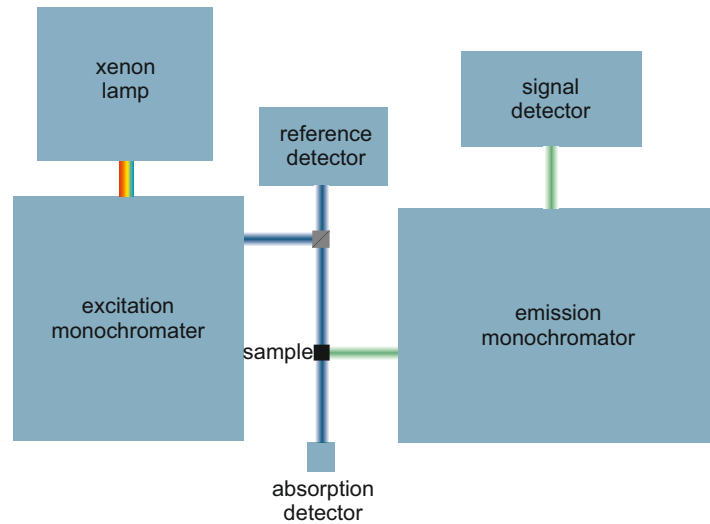


Figure 3.5: Schematic Description of the Fluoromax4-Plus A Xenon lamp is used as a white light source. The excitation monochromator selects the desired wavelength directed onto the sample. Simultaneously a small fraction of the beam is directed on a reference detector to monitor the excitation source. In a 90° angle to the excitation, the emission is collected through the emission monochromator, and the signal is detected on a photomultiplier. In the direction of excitation, an absorption/transmission measurement option is added. The absorption detector detects the intensity for each wavelength. For PLQY, the sample is placed in a highly reflective integrating sphere using the same excitation and emission paths.

according to the Beer-Lambert law, the OD of the dispersion must be kept low enough to ensure only one scattering or absorption event per photon.

$$T(\lambda) = \frac{I(\lambda)}{I_0(\lambda)} = 10^{-OD(\lambda)} \quad (3.6)$$

For absorption measurements the absorbance/transmission accessory from *Horiba* is necessary. It includes an additional detector in the direction of the excitation light. A cuvette with the corresponding solvent was used in all cases as a reference.

Photoluminescence

The isotropic PL emission is collected in a 90° angle to the excitation. A monochromator is used to separate the emission and a photon counting detector evaluates the signal intensity for each desired wavelength. PL measurements were conducted with slit sizes of 1 nm, an integrating time of 0.1 s and a spectral resolution of 1 nm. The excitation wavelength is varied between 350 and 550 nm depending on the type of sample and the expected emission. If needed, the PL emission can be measured time-dependently by so-called 'time correlated single photon counting' (TCSPC). Thereby, the time between excitation and emission of single photons is detected, which indicates the lifetime of charge carriers in a semiconductor.

Photoluminescence Quantum Yield

For PLQY measurements, an integrating sphere (Quanta- ϕ , *Horiba*) is used. This is coated with a highly reflective material to measure the emission and scattering of the sample in all directions to quantify the number of photons. PLQY is given by the ratio of emitted (N_{em}) to absorbed photons (N_{abs}):

$$PLQY = \frac{N_{em}}{N_{abs}} \quad (3.7)$$

Therefore four spectra need to be taken in total. The excitation and emission spectra need to be measured for a reference (usually the corresponding solvent in a comparable cuvette) and the sample. The difference in the excitation peak area of the reference and sample measurements is proportional to the number of absorbed photons while the difference in the emission peak areas is proportional to the number of emitted photons. The resulting PLQY can be strongly affected by the reabsorption of photons. Therefore, the sample should exhibit an OD equal to or smaller than 0.1 at the desired excitation wavelength.

3.4 Computational Methods

A machine learning-based algorithm to predict NPL syntheses was developed and implemented in collaboration with Ionnis Kouroudis and Milan Harth in the group of Prof. Alessio Gagliardi at the Technical University Munich. The basics will be presented here briefly.

Prediction of the PL peak quality

PL spectra of the samples were evaluated to quantify their quality. The spectra are normalized, and the half width half maximum (hwhm) is determined, which functioned as criteria for the narrowness of the spectra (f_{narr}). The symmetry of the spectra was rated depending on its skewness. By treating the PL spectra as a probability distribution, the final quality factor QF is given by:

$$QF = \frac{1}{f_{sym} + f_{narr}} \quad \text{with} \quad f_{sym} = 100 \cdot \frac{\bar{X} - \tilde{X}}{\bar{X}} \quad (3.8)$$

With \bar{X} representing the mean of the spectrum and \tilde{X} the median of the spectrum. A Gaussian Process predictor was implemented using 'scikit-learn'.¹³² It was used to predict the quality factor values based on precursor ratios. The kernel employed was the sum of a radial basis function and a Matern covariance function whose parameters were optimized by maximizing the log-marginal-likelihood.

Prediction of the NPL thickness

The NPL thickness was predicted using a neural network implemented through the TensorFlow library.¹³³ Historical data was used to train the neural network consisting of 3 hidden layers with five neurons and an output layer with one neuron. A Root Mean Squared Propagation with exponential decaying learning rate was used as an optimizer. The network was evaluated employing a 10-fold validation and found to have a median relative error of 0.91%.

Prediction of the homogeneity of NPLs

A random forest classifier was trained with the library scikit-learn to identify inhomogeneous samples with multiple PL maxima. The random forest has a maximum depth of 150 and evaluates with stratified 10-fold validation.

Constraints from experimental experience

Soft Lagrange multipliers were used to implement constraints based on general experimental experience and laboratory limitations. Following restrictions were implemented: the amount of acetone must be at least 30 vol% of the synthesis, and the volume fraction of PbBr_2 must be the same or larger than the amount of Cs-oleate.

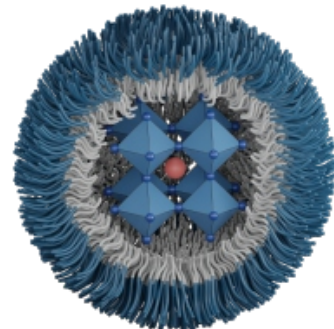
Optimization process

The above mentioned algorithms were combined in a Bayesian Optimization framework. In this specific work, the Improvement Maximization acquisition function was used to determine the balance between exploration and exploitation. For each NPL thickness, a set of 100.000 random three-dimensional vectors was generated representing the ratio of the three precursors. For every vector, the QF was predicted as well as the peak position and multi peak behavior. For each thickness, the suggestions with the highest QF were synthesized and added to the data pool.

4

Stability of Lead Halide Perovskites

This chapter presents a novel synthesis routine for perovskite nanocrystals. Within this scope, diblock copolymer micelles comprising polystyrene and polyvinyl pyridine are introduced as nanoreactors. While the use of micelle nanoreactors supports the fabrication of very homogeneous samples and thin films, they also increase the durability of the perovskite phase. Micelle-encapsulated nanocrystals show a greatly enhanced stability towards external degradation factors like oxygen, light, and water. Even in complete submersion, micelle-encapsulated NC thin films show no noteworthy change in optical properties after more than 70 days. To further improve the synthesis routine, DLS was used to analyze distinct synthesis steps. An adaption of the amounts used for the synthesis as well as of the time demand is investigated. Lastly, organic ligands are introduced in the synthesis procedure to improve the optical properties. Thereby a confinement effect is discovered, which is induced by different ligand lengths. Results and figures presented in [Section 4.1](#) and [Section 4.3](#) have been published in [Reference \[134\]](#) and [Reference \[135\]](#), respectively.



4.1 Diblock Copolymer Micelles as Nanoreactors

To circumvent stability issues induced by external forces and avoid using organic ligands, diblock copolymer micelles will be introduced as nanoreactors to synthesize LHP NCs. The well-defined homogeneous size of polymer micelles limits the growth of NCs inside, resulting in highly monodisperse samples. The chosen diblock copolymer PS-PVP is well understood regarding its behavior in organic solvents and has already been reported in the successful synthesis of metal nanoparticles.⁵⁶ For the synthesis here, PS(266)-PVP(41) is dissolved in toluene, wherein the polymer self assembles in micelles with a PS shell and a PVP core due to the different solubilities of the polymer blocks. Precursor salts are added to the solution inducing an accumulation of ions in the micellar cores, where they spontaneously form perovskite NCs. The synthesis yields LHP-filled micelles, whose optical properties are immediately characterized. PL measurements show narrow PL spectra for methylammonium lead halide-filled micelles, with a single PL peak between 400 and 765 nm depending on their halide composition (see Figure 4.1). The spectral positions indicate very weak or no quantum confinement effects corresponding to NC sizes of at least the size of the exciton Bohr radius (3 to 5 nm) of methylammonium LHPs. The PL spectra exhibit a narrow fwhm around 80 to 100 meV for $\text{Cl}_{1-x}\text{Br}_x$ compounds and a fwhm of 100 to 215 meV for $\text{Br}_{1-x}\text{I}_x$ compounds. Broadening of the emission spectrum can originate in inhomogeneous halide distribution or inhomogeneous NC shapes and morphologies. The PLQY of the samples reaches up to 65% for pure halide compounds and is slightly lower for mixed halide samples.

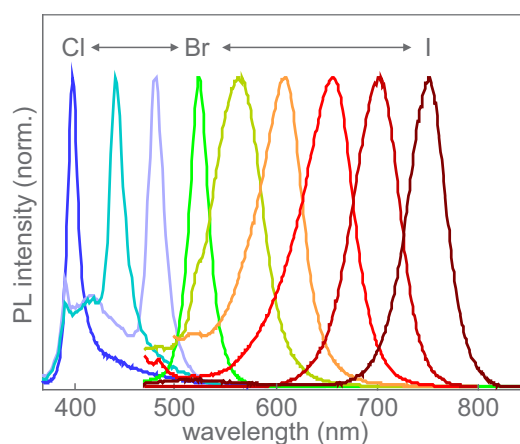


Figure 4.1: Photoluminescence Spectra of Micelle-Encapsulated Methylammonium Halide Perovskites As the halide composition is varied from Cl to Br to I, the maximum position of the single PL peak shifts from 400 to 505 to 765 nm, spanning the whole visible spectrum. Adapted from Reference [134].

The synthesis can be conducted with any organic-inorganic perovskite compositions, as can be seen in Figure 4.2. FA-based perovskite samples show narrow PL spectra with fwhm ranging from 104 to 112 meV (Figure 4.2 a). Interestingly, especially the iodide rich compounds exhibit more narrow PL peaks than the MA-based perovskites. However, no pure FAPbCl_3 sample was obtained. This is an expected behavior since FAPbCl_3 exhibits a Goldschmidt factor of 1.02 which is at the limit for stable perovskite phases (compare Figure 2.7). Cs-based perovskites exhibit fwhm from 102 to 135 meV in the whole spectral range (Figure 4.2 a). It appears, that MA-based perovskites are prone to broaden PL spectra, this can be an indication for inhomogeneous NC size distributions. The PLQYs of FA and Cs perovskite samples are comparable to the MA compounds with values around 30 to 60%. In general, Cs- and FA-based perovskite samples show more narrow and more symmetric PL peaks than the

MA-based samples. A reason for that can be the asymmetry of the MA molecule. Another explanation would be different reaction kinetics of the respective combinations. A slow growth of the NCs would result in a more homogenous size distribution and consequently in a narrower and more symmetric PL peak. However, to find the origin of spectral differences, detailed studies on the mechanism of the synthesis and spectroscopy on single particles are necessary. **Figure 4.2 c** shows the PL spectra of mixed cation LHP, $\text{Cs}_a\text{MA}_b\text{FA}_c\text{PbBr}_3$ with $a + b + c = 1$. The PL maximum positions vary between 524 and 530 nm depending on the cation composition with PLQYs up to 84 %. With increasing Cs-content the PL is shifted towards the pure CsPbBr_3 PL signature which has a PL maximum at 520 nm. An increasing fraction of large A-cations (FA) red-shifts the PL maximum towards the band gap energies of MAPbBr_3 (528 nm) and FAPbBr_3 (536 nm). Compared to the halide ion position, the A-cation has only little impact on the band gap due to deep lying energetic states as shown in **Figure 2.8**.

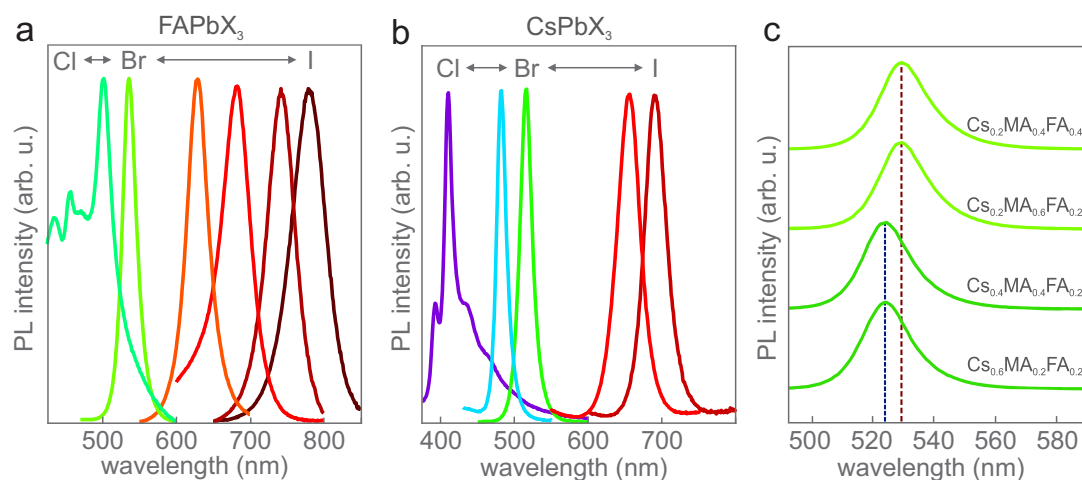


Figure 4.2: Photoluminescence Spectra of Micelle-Encapsulated Mixed Perovskites PL spectra of (a) formamidinium based LHP, FAPbX_3 with $X = \text{Cl}, \text{Br}, \text{I}$ and (b) cesium based LHP, CsPbX_3 with $X = \text{Cl}, \text{Br}, \text{I}$. By combination of halide ions the whole visible spectrum can be covered as long as the ion composition is suitable for a perovskite structure which is not the case for FAPbCl_3 . (c) PL spectra of mixed cation LHP, $\text{Cs}_a\text{MA}_b\text{FA}_c\text{PbBr}_3$ with $a + b + c = 1$. PLQYs of up to 84 % can be achieved.

Figure 4.3 shows TEM images and atomic force microscopy (AFM) images of micellar monolayers along with the corresponding micellar size distribution and film roughness. As reported by Lohmüller et al., PS-PVP micelles arrange in a quasi-hexagonal pattern upon dip coating, which could be visualized well in AFM and TEM analysis.⁵⁶ AFM measurements of dip coated micelle samples reveal a homogeneous monolayer film over the range of several μm (see **Figure 4.3 a**). A surface coverage of 99.5% with a roughness of less than 2 nm is obtained. By measuring the height of a monolayer, a micelle size of around 12 ± 2 nm is obtained. This is supported by the corresponding TEM image showing micellar core sizes of around 11 ± 2 nm (see **Figure 4.3 b**). Importantly in TEM images, only high contrast material like the perovskite is visible but not the low contrast polymer. It can be concluded that the polymer collapses to a very thin layer around the perovskite in thin films as the difference in micelle size from AFM and the micellar core size from TEM is only around 1 nm. High-Resolution TEM reveals an irregular shape of the micellar cores (see **Figure 4.3 c**). Furthermore, no distinct NC shapes or borders are noticeable. The different shapes of the micelles and the absence of distinct NCs indicate the presence of multiple NCs per micelle. Another reason for enlarged NC population in single micelles is the nature of the PVP monomers. The nitrogen in PVP can act as a coordination centre for lead ions.¹³⁶ Strong coordinated N-Pb bonds can form and act as a nucleation centre for LHP NCs. Since they are locally fixed in the micelle core which consists of numerous PVP monomers, several NCs can

grow simultaneously and independently resulting in inhomogeneous NC sizing. Therefore we assume several NCs per micellar core.

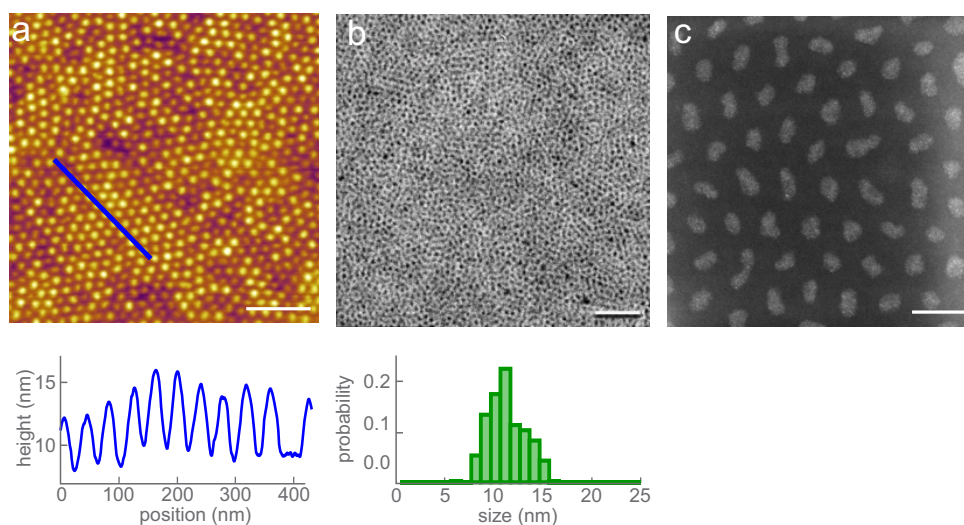


Figure 4.3: TEM and AFM images of Micelle Monolayers (a) AFM measurements measurement of a dip-coated perovskite-filled micelle thin film. A highly homogeneous film is observed with a surface roughness of less than 2 nm as shown in the height profile along the blue line. The surface coverage is determined to be 99.5 %. Scale bar correspond to 200 nm. Adapted from Reference [134]. (b) TEM image with the corresponding micelle core size distribution for micelle-encapsulated MAPbI₃ NCs. An average micelle core size of 11 nm is obtained. Scale bar correspond to 200 nm. Adapted from Reference [134]. (c) High-Resolution TEM image of micelle-encapsulated MAPbI₃ NCs. A irregular shape of micelle cores is observed along with the quasi-hexagonal pattern. No distinct NCs are obvious in the high-resolution image indicating a arbitrary NC population in the micellar cores. Scale bar correspond to 50 nm.

Different polymer lengths were tested to investigate the effect of the polymer block size in diblock copolymer micelles. Figure 4.4 shows TEM images of micelle-encapsulated MAPbI₃ NCs with different polymer lengths. By comparing the images, it is obvious that the micellar core size varies in the range from 6 to 27 nm. Taking the polymer length into account, it appears that the PVP chain length correlates linearly with the micellar core size (compare Figure 4.5). Interestingly, it shows no dependence on the PS content. By further comparing the TEM images, different center-to-center distances are measured and the spacing between micellar cores is determined. The results from the analysis are summarized in Table 4.1. The increasing micelle core size with increasing PVP content can nicely be seen from the table. Interestingly, the center-to-center distance correlates with the micelle core size but not with the overall polymer length. This indicates a non-linear behavior of the PS chain upon drying on a substrate as the polymer chains are not a rigid system but variable and can adapt different stackings and foldings depending on their environment.

Table 4.1: Micelle Sizes and Spacings Obtained From TEM Imaging Micellar core sizes and center-to-center distances for different polymer lengths.

polymer	core size (nm)	center-to-center distance (nm)	spacing between micelle cores (nm)
PS(259)-PVP(11)	6±1	11±2	5±1
PS(153)-PVP(33)	9±1	19±3	10±2
PS(266)-PVP(41)	11±2	27±4	16±3
PS(113)-PVP(143)	27±2	40±3	13±2

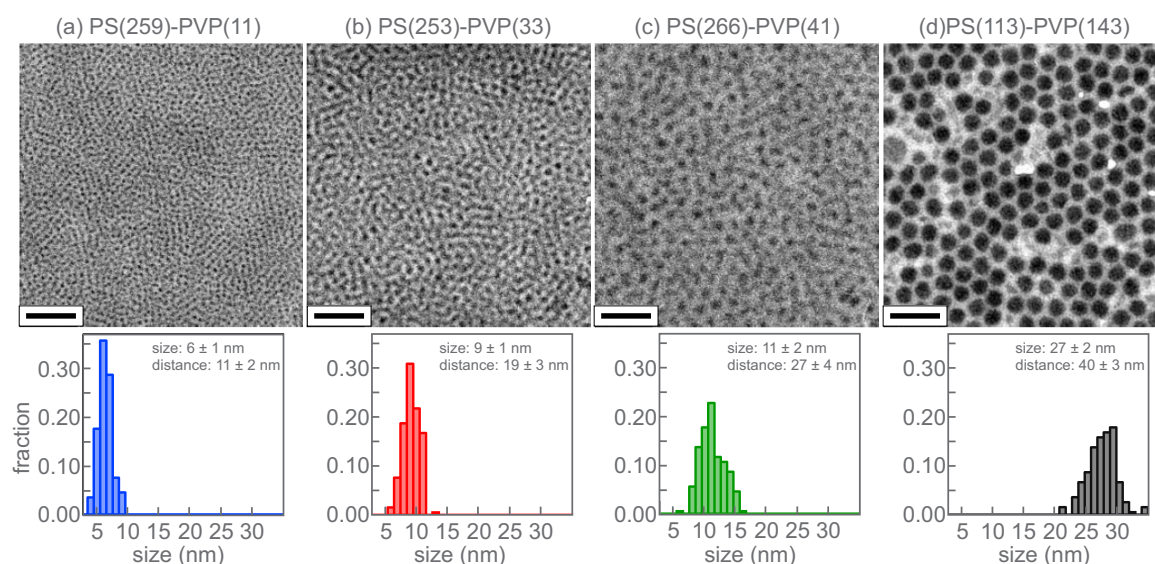


Figure 4.4: TEM Images and Corresponding Size Distributions for Different PS-PVP Polymer Lengths TEM images and corresponding size distributions for following polymers: (a) PS(259)-PVP(11) (b) PS(153)-PVP(33) (c) PS(266)-PVP(41) and (d) PS(113)-PVP(143). The obtained sizes are 6 ± 1 nm, 9 ± 1 nm, 11 ± 2 nm and 27 ± 2 nm, respectively. Scale bars correspond to 100 nm. Adapted from Reference [134].

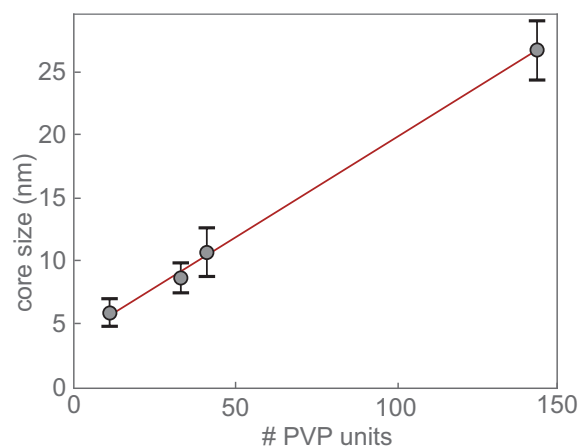


Figure 4.5: Size Dependence of PS-PVP Micelles The size of the perovskite cores is linearly dependent on the number of PVP units of the respective polymer and independent of the PS part. This allows a precise tuning of the desired NC sizes. Adapted from Reference [134].

To gain more insight into the internal structure of the samples, WAXS analyses were performed on micelle-encapsulated MAPbI_3 nanocrystals. Figure 4.6 shows a perfect alignment of measured WAXS intensity (red curve) and previously obtained data for bulk MAPbI_3 .¹³⁷ This confirms the formation of highly crystalline MAPbI_3 in the micelle. Additionally, SAXS was performed to analyze the micelle structure. The diffraction profile of empty micelles shows a broad diffraction at $q = 0.8 \text{ \AA}^{-1}$ and $q = 1.4 \text{ \AA}^{-1}$ indicating refraction of bulk PS, which resembles the fingerprint of micelles.¹³⁸

The ultimate purpose of introducing PS-PVP nanoreactors was to enhance the durability of LHP nanocrystals. Thus, multiple thin film samples were fabricated and exposed to different levels of degradation factors. The test environments comprise ambient atmosphere and submersion in water. As reference, thin films of conventional ligand-passivated MAPbI_3 NCs were treated in similar conditions. Samples in ambient conditions experienced daylight illumination and a relative humidity of approximately 40%. Within 13 days, the reference MAPbI_3 NCs exhibit a rapid blueshift and simultaneously a complete loss of PL intensity (compare Figure 4.7 a). Figure 4.8 a shows the relative PL intensity of

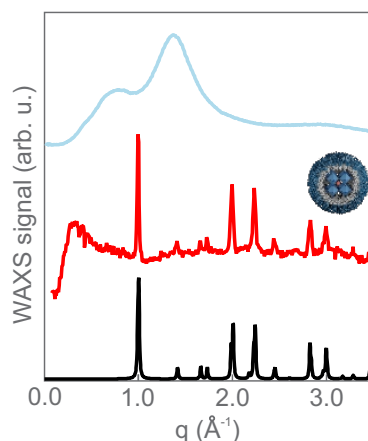


Figure 4.6: WAXS and SAXS analysis of Micelle Encapsulated Nanocrystals WAXS analysis of micelle-encapsulated MAPbI₃ NCs (red line) perfectly aligns with WAXS signal obtained for bulk MAPI crystals (black line).¹³⁷ Additionally, empty micelles were analyzed (blue line). The SAXS signal shows two broad peaks, resembling the fingerprint of bulk PS. Adapted from Reference [134].

the corresponding samples, with the black line indicating the rapid degradation of reference MAPbI₃ samples. The green curve depicts the development of the PL intensity of micelle-encapsulated NCs in ambient conditions. The PL intensity decreases significantly slower while maintaining the initial sample's shape and PL maximum position. After 150 days, the sample still exhibits 50% of the initial PL intensity, leveling out around 40% after 220 days with similar spectral features as the initial sample, as can be seen in Figure 4.7 b. The resilience of micelle-encapsulated NCs against oxygen, light, and humidity exposure increases drastically by a factor of 15 compared to common MAPbI₃ NCs. To find the durability limits of micelle-encapsulated NCs, films were directly submerged in water while tracking their PL intensity. Reference samples degrade upon contact with water and are therefore not shown in the graph. Micelle-encapsulated NCs, however, withstand the water-induced degradation. A steady decrease in PL intensity is observed, as can be seen in the blue curve in Figure 4.8 a. Nevertheless, the immersed NC samples retain more than 40% of the initial PL intensity after 13 days and exhibit a distinct PL signal even after 75 days (see Figure 4.7 c). The micelle nanoreactor's shell drastically enhances the stability of LHP NCs exposed to air, light, and water while retaining the optical properties completely.

A second important factor for the stability of LHPs is the migration of halide ions, which hinders the application of mixed halide samples and the fabrication of heterostructures. We show that micelle-encapsulated NCs in films are impermeable for halide ions widening the application potential of these. Therefore, to examine the ability to suppress halide ion migration, thin films of MAPbBr₃-filled micelles were submerged in aqueous solutions saturated with either PbCl₂ or PbI₂. Even after several days of submersion, no significant effect on the samples is observed. Figure 4.8 b shows the corresponding PL spectra of micelle-encapsulated MAPbBr₃ NCs before (green) and after submersion in either a PbCl₂ solution (blue) or a PbI₂ solution (red). No shape change or shift of the PL maximum peak is visible, proving a successful suppression of the halide ion migration in films. Thus the PS-PVP polymer shell prevents not only degradation but also ion migration, providing a stable and spectrally constant emission source for future applications.

The question may arise how a NC encapsulated in insulating material should be integrated into an electric device. Since the direct charge injection into the NC is not possible here due to the polymer micelle shell, we prove the accessibility for applications by another charge carrier injection strategy,

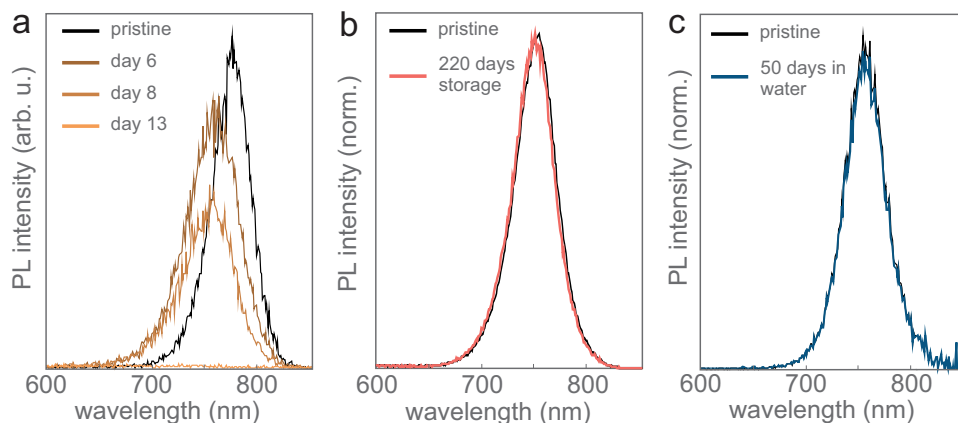


Figure 4.7: Photoluminescence Analysis of Differently Fabricated and Stored LHP NC Films Before and After Stability Experiments (a) PL spectra of ligand passivated MAPbI₃ NCs over 13 days of storage in ambient conditions. A steady decrease of intensity and blueshift of the spectral position indicates a fast degradation of unprotected NCs. (b) Normalized PL spectra of micelle-encapsulated LHP NCs before and after 220 days of storage in ambient conditions. The shape and position of the emission remain constant. (c) Normalized PL spectra of micelle-encapsulated LHP NCs before and after submersion in water for 50 days. The shape and position of the emission remain constant, indicating a vast improvement in the stability of LHP NCs. Adapted from Reference [134].

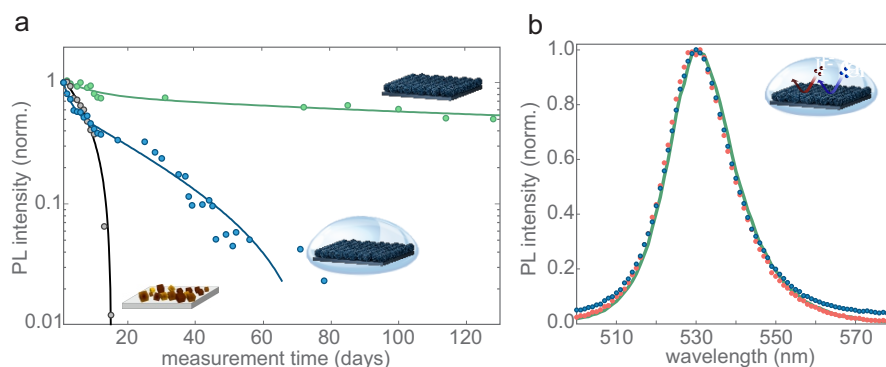


Figure 4.8: Enhanced Stability of Diblock Copolymer Micelle Encapsulated Nanocrystals (a) Temporal development of the relative PL intensity of encapsulated LHP NC thin films. Common organic ligand-passivated MAPbI₃ NCs quickly degrade in ambient conditions within 13 days (black curve). In contrast, micelle-encapsulated NCs retain nearly 60% of the initial PL intensity after 130 days and still exhibit significant PL intensity after 220 days (green curve). Even after complete submersion in water, encapsulated NCs show discernible PL for over 75 days (blue curve). Adapted from Reference [134]. (b) PL spectra of a micelle-encapsulated MAPbBr₃ NC thin film (green line) and of similar films subjected to aqueous solutions of lead halide (blue points, PbCl₂; red points, PbI₂). No noteworthy change in the PL spectra are observed proving the successful suppression of halide ion migration into or out of the micelles. Adapted from Reference [134].

namely Förster Resonance Energy Transfer (FRET). Hereby, energy is exchanged from a donor to an acceptor providing donor emission and acceptor absorption overlap and the corresponding dipole moments align. FRET is known to occur at distances up to 10 nm, which is larger than the polymer shell between adjacent NCs in thin films. For the FRET experiments, a heterostructure of a thick film of micelle-encapsulated MAPbBr₃ NCs is fabricated, and a thin film of MAPbI₃-filled micelles is deposited on top. A schematic structure of the resulting sample is shown in Figure 4.9 a, b together with a schematic representation of the experiment. Figure 4.9 c shows the corresponding PL spectra for each sample type and the PL spectra of the combined heterostructure. The fact that the PL spectra do not change further proves the suppression of halide migration and the ability to build heterostructures. The sample is excited with a laser at 450 nm. It is noteworthy that the PL peak dedicated to the MAPbI₃ NCs is nearly as strong as the MAPbBr₃ component despite being a lot thinner. To verify

the occurrence of FRET, we compare the PL decay of the MAPbBr₃ compound in a pure film and the heterostructure. In both cases, a multiexponential decay is observed. However, for the heterostructure, it is much faster. The PL decay time at which the PL intensity decreases to 1/e has fallen from 0.59 to 0.41 ns (compare Figure 4.9 d). An additional decay pathway can explain this for MAPbBr₃ in the combined sample, which we attribute to FRET-mediated energy transfer. From $\eta_{FRET} = 1 - \frac{\tau'_D}{\tau_D}$ the FRET efficiency and therefore the energy transfer efficiency is determined to be 30.5%. This is a remarkably high number considering the thin MAPbI₃ layer. The occurrence of efficient FRET in micelle-encapsulated samples allows the optoelectronic integration of these. Furthermore, it enables the fabrication of novel structures like cascaded energy transfer systems and energy funnels.

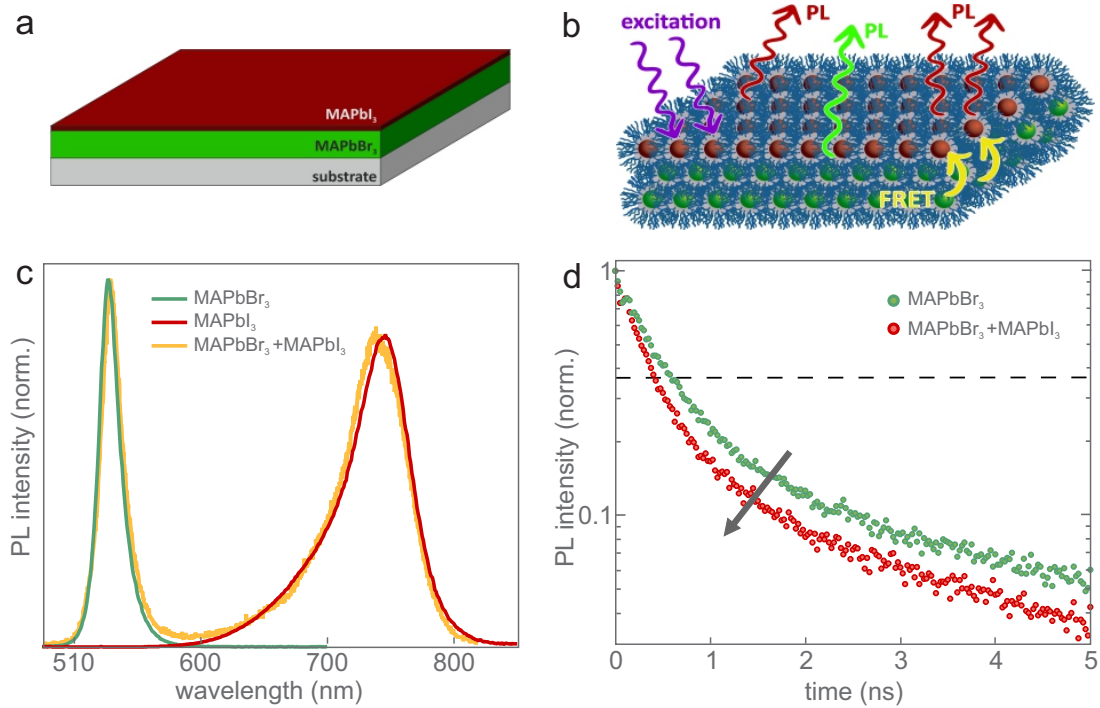


Figure 4.9: Förster Resonance Energy Transfer Between Micelle Encapsulated LHP NCs (a) Scheme of the experimental structure with a thin spin-coated layer of MAPbI₃ NCs on top of a thick layer of MAPbBr₃ NCs. (b) Scheme depicting excitation, emission, and energy transfer in the sample. (c) PL spectra of the pure MAPbBr₃ sample (green), the pure MAPbI₃ sample (red), and the combined structure (yellow). (d) PL decay of the pure MAPbBr₃ sample (green) and of the MAPbBr₃ in the combined structure (yellow) showing an increased decay rate indicating successful FRET. Adapted from Reference [134].

4.2 Optimizing the Synthesis Using Dynamic Light Scattering

By utilizing DLS, the dynamics of the polymer micelle templated synthesis are investigated. The main goal is to improve the synthesis regarding the time demand and cost efficiency. DLS is a non-destructive method to investigate self-assembly processes and nanoparticles in solution, details on the method can be found in [Subsection 3.2.3](#). Firstly, the CMC is determined for different block copolymer lengths, and secondly, the loading with precursor salt is observed. As described in [Subsection 2.2.4](#), the CMC defines the minimum concentration at which micelle formation commences. So far, a high polymer concentration is used for the synthesis to ensure micelle formation. The exact CMC, however, is unknown. The CMC will be determined to reduce and optimize the synthesis cost and procedure, and the effect on the LHP NC's optoelectronic properties will be discussed. In the following, the time dependence of the micelle loading with precursor salt is determined and used to decrease the synthesis duration. Three polymers are investigated in this chapter: PS(113)-PVP(143), PS(221)-PVP(133), and PS(394)-PVP(143). The ratio of PS to PVP is continually increased from 0.79 over 1.66 to 2.76 to elucidate which effect the PS shell thickness has on the NC synthesis.

Critical Micelle Concentration

Different polymer concentrations were measured via DLS, and the resulting intensity spectra were compared to determine the CMC. This method is commonly applied to determine the CMC of block copolymers.¹³⁹ Starting at a high polymer concentration with micelles in the solution, the concentration is subsequently reduced. DLS measurements reveal different particle size distributions for different polymer concentrations. [Figure 4.10 a](#) shows the size distribution for the highest and lowest measured concentrations and the corresponding intensity evolution of the micelle peak for PS(113)-PVP(143). For the lowest concentration (dark green), a peak with a maximum around 1 nm is observed, which is not present for the highest concentration. For the highest concentration (light green) the most pronounced size is around 10 nm accompanied with less pronounced peaks around 60 and 600 nm. The lowest measured concentration should be below the CMC of the polymer, therefore the peak around 1 nm is ascribed to free polymer chains since they are the only population in the solution. In the curve for the highest polymer concentration, the most intense peak around 10 nm is attributed to the micelles. For determining the CMC the intensity of the micelle peak around 10 nm is monitored for each concentration ([Figure 4.10 b](#)). By looking at the graph, three different phases can be identified: First, starting from the lowest concentration no noteworthy change in intensity is recorded (yellow). Secondly, a steep increase in intensity is measured (green). And lastly, a saturation of the peak intensity in a plateau is observed. The CMC is situated between the first and second phase. To determine it, a linear trend is fitted in the yellow region. The steep increase in intensity is fitted by a logarithmic function. The intersection of both fits marks the CMC of the respective polymer. The third phase region is not included in the CMC determination since more complex structures than micelles can occur at high concentrations which would falsify the CMC.

The evolution of the size distributions with varying polymer concentration can nicely be seen in a contour plot. [Figure 4.11](#) shows the corresponding graphs for the three polymers used, which illustrates the expected behavior of a 1 nm size peak for lower concentration transforming in a 10 nm size peak for higher concentrations. Additional larger size peaks (>100 nm) can be attributed to artifacts due to

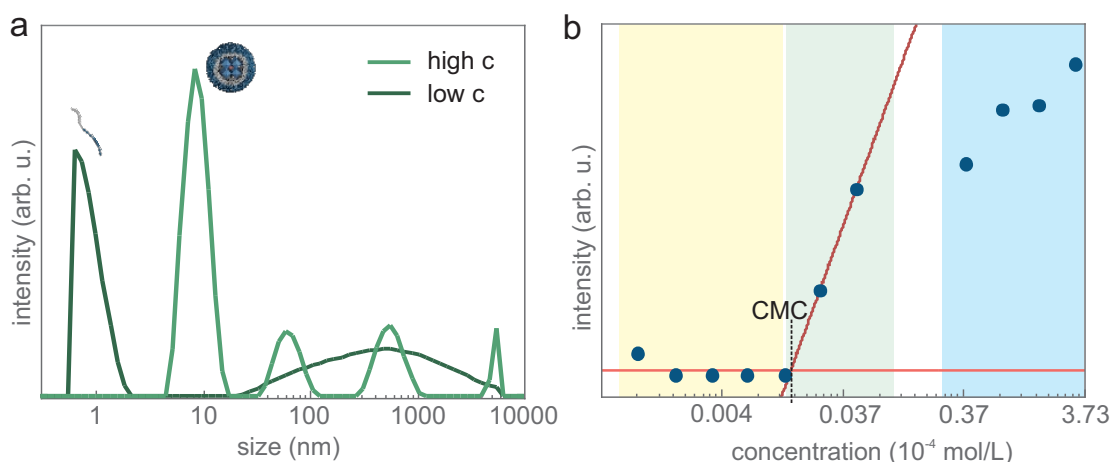


Figure 4.10: Exemplary Analysis of DLS Measurements of PS(113)-PVP(143) (a) Size distribution for the highest and lowest measured polymer concentration obtained from DLS. A peak around 1 nm is ascribed to free polymer chains and a peak around 10 nm is assigned to empty polymer micelles. (b) Intensity of the 10 nm micelle peak for every measured polymer concentration. A slow linear increase is observed in the yellow area, while in the green area a rapid logarithmic increase of the intensity is observed. For high polymer concentrations, a saturation of the peak intensity shows up (blue area).

high polymer concentrations. All polymers were analyzed, and the CMC was determined by fitting the micelle peak intensity as shown in Figure 4.10. The resulting CMCs are:

$$\text{PS(113)-PVP(143): CMC} = 1.3810^{-6} \text{ mol/l}$$

$$\text{PS(221)-PVP(133): CMC} = 3.5710^{-6} \text{ mol/l}$$

$$\text{PS(394)-PVP(143): CMC} = 6.0710^{-7} \text{ mol/l}$$

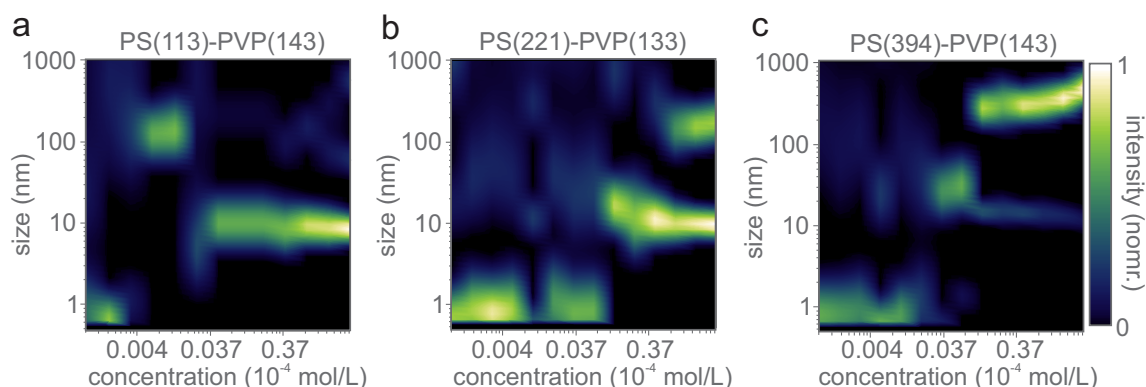


Figure 4.11: Diblock Copolymer Size Distribution Obtained from DLS Measurements Size distribution obtained from DLS measurements depending on the polymer concentrations for (a) PS(113)-PVP(143), (b) PS(221)-PVP(133) and (c) PS(394)-PVP(143). A disappearance of the 1 nm polymer peak and a development of the 10 nm micelle peak signifies the micelle formation.

Precursor Salt Loading

To further improve the understanding of the synthesis process of micelle-encapsulated LHP NCs, the diffusion of a precursor salt into the micellar core is analyzed. For this purpose, MABr is added to the micelle solution, similar to the synthesis process described in Subsection 3.1.1, and the solution is monitored via DLS in 10 min time intervals. As discussed in the previous section, a peak around 10 nm size is ascribed to empty micelles. A change in refractive index and density is expected by introducing the precursor salts. Consequently, it is observed at which point in the synthesis the 10 nm

micelle peak changes or disappears. The temporal development of the size distributions can be seen in Figure 4.12. For PS(113)-PVP(143) the micelle peak starts to lose intensity already after 20 min. A similar behavior is observed for (221)-PVP(133) with a beginning change in intensity after 20 min. Only for PS(394)-PVP(143) the micelle peak remains unchanged for 60 min before the intensity drops. It can be concluded that the five hour time interval in the conventional synthesis (see Subsection 3.1.1) is overestimated, and the micelle loading is finished after 20 to 60 min depending on the polymer length. Only the polymer with the highest PS content requires a longer diffusion time. This is an expected behavior since the ions need to pass a larger volume of unipolar PS to reach the inner micelle part.

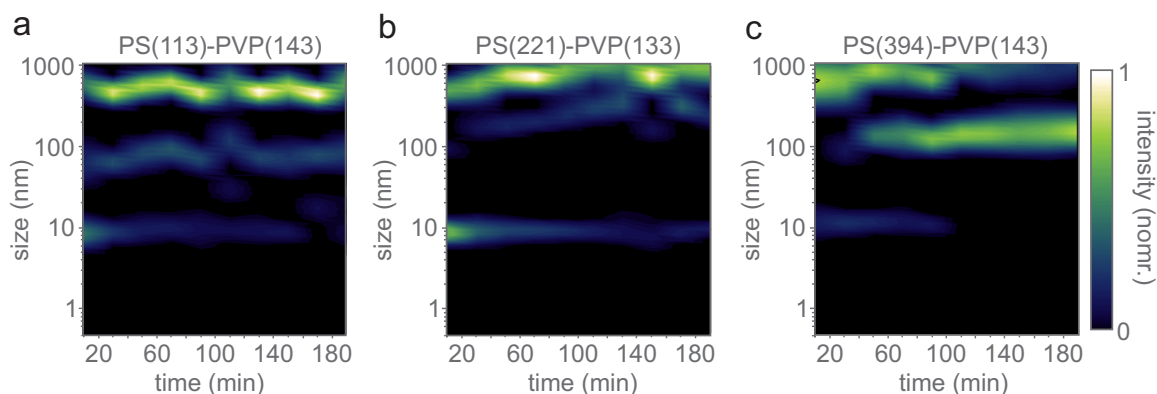


Figure 4.12: Time Dependent Size Distributions Upon MABr Injection in Polymer Micelle Solutions Temporal development of the size distribution obtained from DLS upon MABr addition to the polymer micelle solution for (a) PS(113)-PVP(143), (b) PS(221)-PVP(133) and (c) PS(394)-PVP(143). A vanishing of the 10 nm micelle peak indicate the loading with MABr.

Effect on the Optical Properties

After gaining insight into the CMC and micelle loading time, the synthesis protocol is updated with the findings. The micelle-encapsulated MAPbBr₃ NCs are synthesized accordingly and compared to NCs synthesized with the conventional parameters. Table 4.2 summarizes the original and optimized synthesis parameters. The updated polymer concentration is still higher than the CMC but reduced as far as a logarithmic trend in the micelle peak evolution was observed.

Table 4.2: New Synthesis Parameter for Micelle Encapsulated LHP NCs The concentrations and used loading times for the original and optimized synthesis.

polymer	$c_{original} \left(\frac{mol}{L}\right)$	$c_{optimized} \left(\frac{mol}{L}\right)$	$t_{original} \text{ (min)}$	$t_{optimized} \text{ (min)}$
PS(113)-PVP(143)	3.1310^{-4}	1.1210^{-4}	300	20
PS(221)-PVP(133)	3.1210^{-4}	1.0810^{-4}	300	20
PS(394)-PVP(143)	3.1310^{-4}	1.4310^{-4}	300	60

Figure 4.13 compares PL spectra of samples synthesized with the conventional (dashed lines) and updated (bold lines) synthesis parameter. No noteworthy change in the spectral shape is observed for all three polymers. The PL maximum positions shift depending on the polymer. For PS(113)-PVP(143) the PL position remains constant and the fwhm increases only slightly from 99 to 105 meV. For PS(221)-PVP(133) a shift from 528 to 527 nm is observed with a fwhm increase from 85 to 94 meV. The difference in PL emission is most pronounced for PS(394)-PVP(143) with a PL shift from 521 to 523 nm, interestingly, here the fwhm decreases from 109 to 104 meV. The updated parameters seem to affect the PL properties in a minimal manner. More detailed studies on the synthesis mechanisms are necessary

to elucidate the reasons for the minimal deviations. Additionally, the PLQY was monitored for all samples. The results are listed in Table 4.3. Herein, it can be seen that the PLQY of the encapsulated NCs remains constant at high values above 70% for PS(113)-PVP(143) and PS(394)-PVP(143) or improves, as is the case for PS(221)-PVP(133) from 20 to nearly 50%. The reduced polymer concentration and the shortened micelle loading time have no negative effect on the optoelectronic properties. The samples retain their quality or even gain enhanced optical performance.

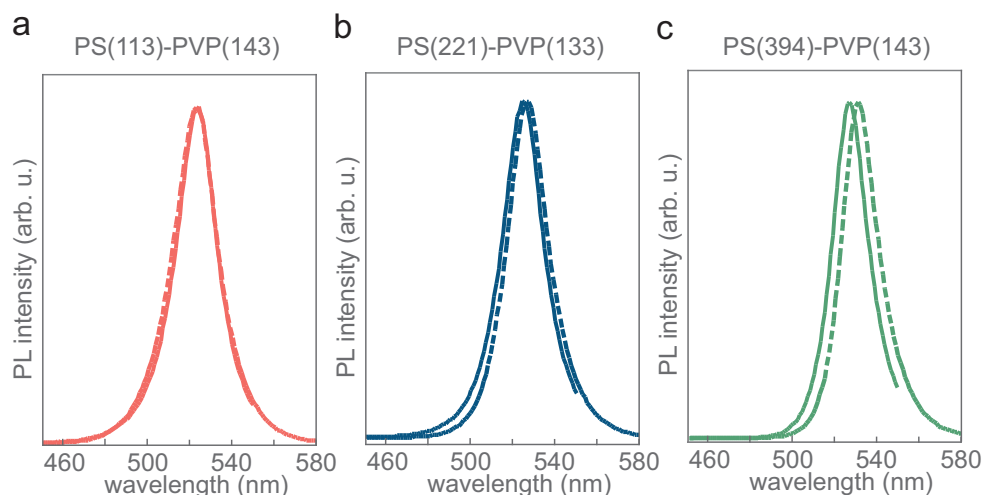


Figure 4.13: Photoluminescence Spectra of Micelle-Encapsulated MAPbBr₃ NCs Synthesized With Original and Optimized Synthesis Parameter PL spectra of micelle-encapsulated MAPbBr₃ NCs with original (dashed lines) and optimized parameters (bold lines) show no only slight change in the emission features: (a) PS(113)-PVP(143), (b) PS(221)-PVP(133), (c) PS(394)-PVP(143)

Table 4.3: PLQY of Micelle-Encapsulated MAPbBr₃ NCs Synthesized With Original and Optimized Parameters PLQY was measured immediately after the synthesis for samples synthesized according to the original and optimized parameters

polymer	$PLQY_{original}$ (%)	$PLQY_{optimized}$ (%)
PS(113)-PVP(143)	87.0	79.5
PS(221)-PVP(133)	19.8	47.5
PS(394)-PVP(143)	78.5	77.5

To conclude this chapter, the CMC and diffusion time of ionic salts in PS-PVP micelles have been analyzed. Thereby, the amount of polymer and the time required for the synthesis steps could be drastically reduced, facilitating the overall synthesis and improving long-term cost efficiency. While optimizing the synthesis parameters, no major drawbacks in the optical performance were observed. On the contrary, for PS(221)-PVP(133) the PLQY could be drastically enhanced by a factor of 2.4. DLS proves itself as a fast, non-invasive method to analyze and identify synthesis processes in solution under laboratory conditions.

4.3 Integrating Organic Ligands

Nanoreactors are the ideal candidates to fabricate stable and durable NCs. Nevertheless, non-ideal PLQY for still prevents the application as efficient emitter material. With PLQY only up to 80% for halide pure compounds, there is still room for improvement. The likely reason for this is the abandonment of organic ligands, which are, until now, crucial for near unity PLQY emitters. Accordingly, we integrate organic ligands into the micelle-templated synthesis. Figures and results from this chapter are published in Reference [135]. The organic ligands fulfill two main tasks: Firstly, they enhance the solubility of the precursors and, therefore, ease the uptake into the polymer micelles. Secondly, organic ligands passivate surface traps and vacancies, reducing non-radiative recombination. Consequently, the implementation of organic ligands should yield a higher amount of nanoparticles with a more efficient emission. The synthesis procedure starts, as described in Subsection 3.1.1, by dissolving the polymer in toluene and adding MAX ($X = \text{Br}, \text{I}$) as a first precursor salt. PbBr_2 is added in a PbBr_2 -ligand solution comprising oleic acid and oleylamine as ligands. The resulting dispersions exhibit single and narrow PL emission peaks ranging from 520 nm to 716 nm depending on the bromide/iodide ratio (see Figure 4.14 a). The PLQY is exceedingly high for all samples, peaking at 95% for the pure bromide compound. TEM images of the sample reveal the same morphology as for the non-ligand sample with a quasi-hexagonal pattern of micelles with core diameters of 8 ± 2 nm. AFM imaging further shows the same pattern and proves the great homogeneity of the sample over a large surface area with a surface roughness of around 1.5 nm (see Figure 4.14 b, c).

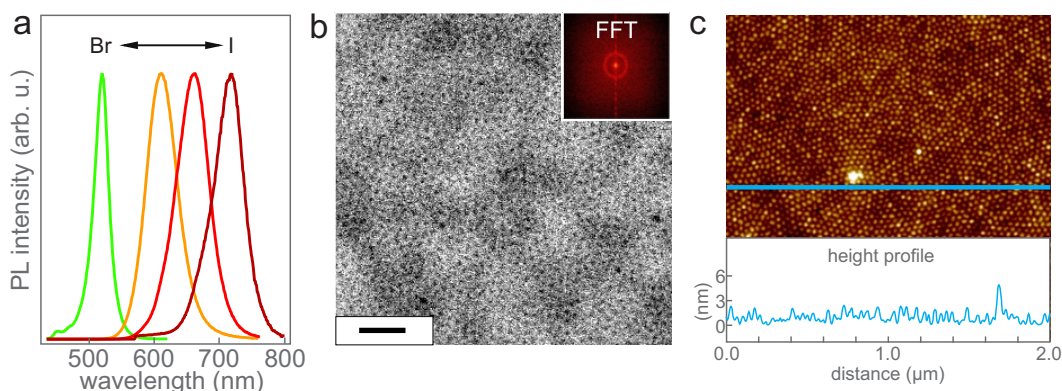


Figure 4.14: General Characterization of Doubly Stabilized LHP NCs Films (a) PL spectra of doubly stabilized MAPbX_3 ($X = \text{Br}, \text{I}$) NCs. By mixing bromide and iodide anions the desired emission wavelength can be chosen. (b) TEM images of doubly stabilized LHP NCs reveal a high homogeneity of the thin films resembling a quasi hexagonal pattern. A micelle core size of 8 ± 2 nm is obtained. FFT of the image (inset) results in a value of 18 ± 2 nm for the NC spacing. Scale bar corresponds to 50 nm (c) AFM imaging shows a high surface coverage for a large film size. The height profile (inset) gives a surface roughness of less than 2 nm.

GISAXS was used to analyze multilayer films of the doubly stabilized NCs to investigate their properties. Figure 4.15 b shows a circular diffraction signal at $p = 0.035 \text{ \AA}^{-1}$ indicating isotropically packed micelles with a center-to-center distance of 20.7 nm. This size is in good agreement with the size obtained from TEM imaging but slightly larger than the sizes obtained from the non-ligand synthesis procedure. The additional ligand molecules could induce swelling of the micelles explaining the increase in diameter. GIWAXS was used to investigate the NCs' crystallinity (Figure 4.15), which shows distinct diffraction peaks (green curve) matching those of a calculated cubic MAPbBr_3 structure (black lines) to verify the desired crystal structure. A Scherrer analysis of the peak widths reveals a NC size of 10.3 ± 2.6 nm. The

refraction pattern further shows additional peaks at small scattering angles (yellow marked curve). This footprint is known for lamellar structures ordered parallel to the substrates, a detailed analysis reveals a spacing of 3.96 ± 0.03 nm. Considering the approximate length of one oleylamine molecule, this diffraction signal can be attributed to a multilamellar ligand phase of oleylamine and oleic acid. Considering all these findings, we propose a film of micelle-encapsulated MAPbBr₃ NCs passivated with organic ligands. The micelles self-assemble in closely packed layers, with residual ligands forming lamellar structures around the doubly stabilized NCs. A schematic representation of the proposed film morphology is shown in Figure 4.16.

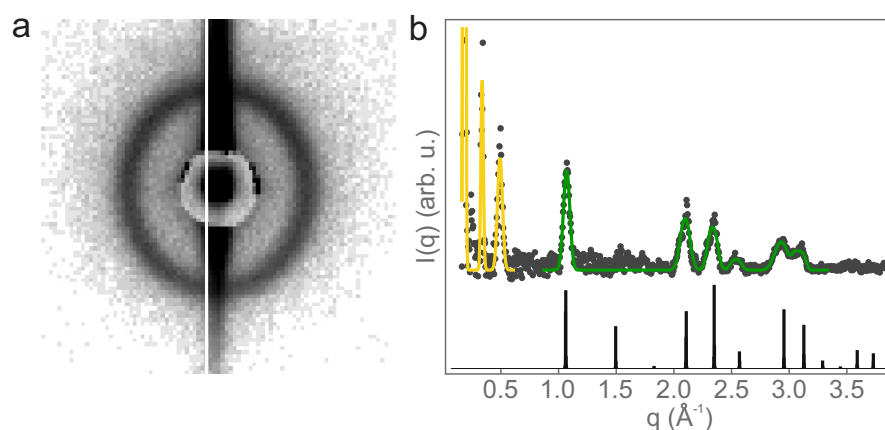


Figure 4.15: XRD Analysis of Doubly Stabilized Nanocrystals (a) A GISAXS detector image of empty polymer micelles mixed with dodecylamine ligands reveals a spacing of 20.7 nm. (b) GIWAXS data of doubly stabilized MAPbBr₃ NCs with oleylamine ligands (grey dots) show Bragg peaks matching DFT calculations of the cubic MAPbBr₃ structure (black lines). Scherrer analysis of the peak widths (green line) yields micelle core sizes of 10.3 ± 2.6 nm. Sharp peaks at small scattering angles (yellow line) correspond to a lamellar ligand bilayer phase with a spacing of 3.96 nm.

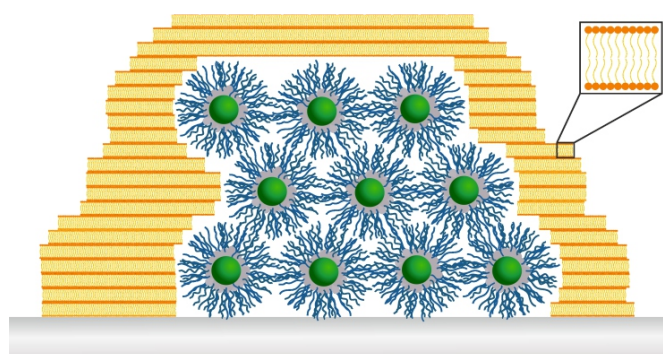


Figure 4.16: Schematic Depiction of a Thin Film Comprising Doubly Stabilized LHP NCs The proposed film morphology of doubly stabilized LHP NCs comprises tightly packed doubly stabilized NC assemblies embedded in ligand bilayers.

Since GIWAXS suggested the formation of a ligand bilayer, different ligand lengths were tested to investigate the effect of the organic molecules further. Surprisingly, the length of the amine ligand had a pronounced effect on the spectral PL position. By decreasing the amine ligand length from 18 to 6 carbon atoms, a gradual blue shift of the emission of MAPbBr₃ NCs from 520 nm to 491 nm

was observed (Figure 4.17 a). The same shift can be seen in absorption spectra of the corresponding samples (Figure 4.17 c). A comparable behavior is observed for MAPbI₃ NCs with a shift from 670 to 610 nm of the emission maximum (Figure 4.17 b). The blueshift indicates quantum confinement effects (see Subsection 2.1.4) induced by the ligands. TEM analyses of MAPbBr₃-filled micelles with different ligand compositions, however, reveal a negligible size dependence of the micellar cores (Figure 4.18). For all amine ligand lengths from 6 to 18 carbon atoms, an average micellar core size of 8 to 10 nm is observed. Therefore, we assume that the micelle core size remains unaltered by the ligands and that each micelle contains more than one NC on average, which are, however, not resolvable in TEM. Since quantum confinement effects occur, it can be concluded that the NC sizes have to range from 3 to 15 nm. To expand on this observation, a ligand with an extremely short hydrocarbon chain like butylamine was tested in the synthesis. The resulting PL spectrum shows hardly any luminescence with a weak intensity. Due to its high volatility, butylamine tends to evaporate, significantly reducing its concentration and consequently not participating in the synthesis resulting in poor optical properties (see Figure 4.19 a). Interestingly, the effect of using a short acidic ligand is less significant. By using hexanoic acid instead of oleic acid, a PL blue shift of only 9 nm is observed, significantly lower than the 29 nm shift for the amine chain length variation (compare Figure 4.19 b). The PLQY of samples comprising ligands with 6 to 18 carbon atoms exhibits high values, on average 90%, with the lowest for dodecylamine with 78% and the highest for oleylamine with 95%. This proves the necessity of organic ligands in the synthesis for near unity PLQYs, a main condition for lighting application.

Aliphatic ligands are an additional factor in the protection of LHP NCs. As reported in Reference [134] diblock copolymer micelle nanoreactors significantly enhance the long-term stability of LHP NCs towards environmentally-induced degradation. We conducted similar stability experiments. To this end, thin films of doubly stabilized NCs were submerged in water, and the PL spectra were monitored for several hours. All films retained the spectral positions and shape of their PL spectra, albeit with a lower overall (see Figure 4.20 a). The decrease in PL intensity is most prominent for the shortest ligand, hexylamine, where it drops to 46% of the initial value. In contrast, for the oleylamine sample, 86% of PL intensity is retained after a 12 h submersion in water. This effect is likely due to the increasing hydrophobicity for increasing aliphatic chain lengths, which shields the NCs more efficiently. Figure 4.20 b shows the development of PLQY of doubly stabilized NC thin films stored in ambient atmosphere. The films exhibit a high PLQY of 60%, which slowly decreases to 37% within 30 days. This is far superior to most nanomaterial thin films.^{140,141} Adding to storage and atmosphere testing, we investigated the behavior of doubly stabilized NCs under UV illumination. For this, samples were continuously illuminated with a 365 nm lamp (8 W) and the PL intensity was monitored. For this, NC dispersions were analyzed instead of NC thin films to exclude the combined effects of UV illumination and oxygen. The results are presented in Figure 4.20 c. The samples showed no noteworthy change in PL spectra or intensity over 24h. In comparison, common ligand passivated MAPbBr₃ NCs showed a rapid decrease of PL intensity to zero after only 150 min. Concerning potential device integration of NC materials, this is a major improvement for the stability and integrability of LHP NCs.

Nevertheless, the addition of additional organic material in the samples could impede the integrability of the LHP NCs in lighting applications. To ensure the functionality of the samples, we show a proof-of-concept integration of doubly stabilized NCs as optical downconverters, similar to commercial fluorophores, e.g., in QD displays. Therefore, we developed a downconverter-organic-LED (DC-OLED) in cooperation with the group of Wolfgang Brütting at the University of Augsburg. Details on the

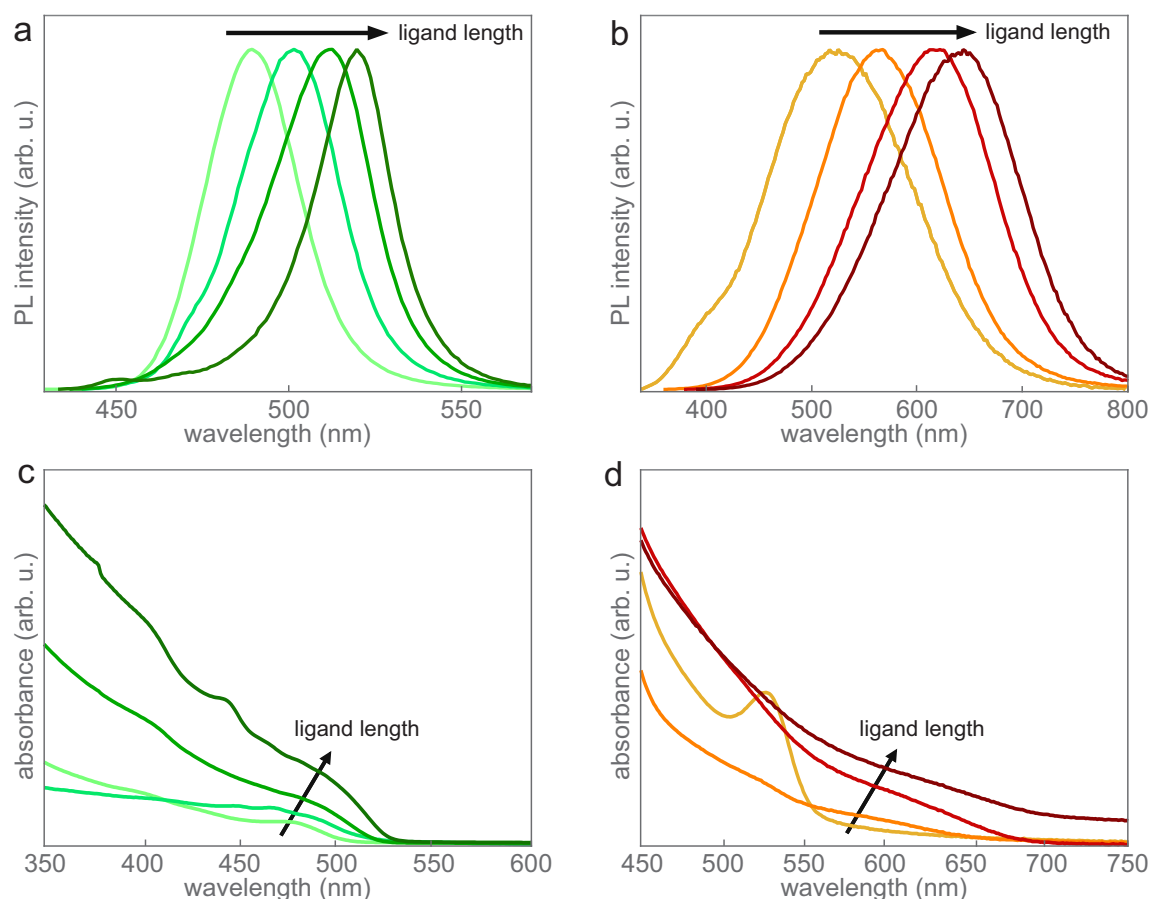


Figure 4.17: Optical Properties of Doubly Stabilized LHP NCs (a) and (c) show PL and absorption spectra of doubly stabilized MAPbBr₃ NCs with hexylamine, octylamine, dodecylamine and oleylamine as amine ligand, respectively. A continuous blueshift with decreasing ligand length is observed in PL and absorption spectra. (b) and (d) show PL and absorption spectra of doubly stabilized MAPbI₃ NCs with hexylamine, octylamine, dodecylamine and oleylamine as amine ligand, respectively. Similar to the bromide compound, a blueshift of the optical features with decreasing ligand length is observed.

device can be found in Reference [135], a schematic depiction of the fabricated device is shown in Figure 4.21 a. The polymer micelle nanoreactors were concentrated and deposited on the back of the OLED's glass substrate, absorbing almost all blue light and converting it into green emission. The OLED itself has a turn-on voltage of about 3 V, a spectral emission peaking at 405 nm and reaches a luminance of more than 1000 cd m⁻² at 10 V. The EQE peaks at 0.4% at low current densities and starts rolling off above 10 mA cm⁻² due to exciton-exciton and exciton-polaron quenching.¹⁴² The DC-OLED shows a strong luminescence with an emission maximum at 532 nm with a narrow fwhm of 24 nm (see Figure 4.21 b). The downconverter device shows comparable characteristics to the initial OLED, however, the luminance increases to a maximum of 2650 cd m⁻² at 10 V (Figure 4.21 c). Additionally, the EQE of the DC-OLED is enhanced, which can be explained by an improved outcoupling of the blue OLED pump into the perovskite layer and of the light emitted by the perovskite NCs (Figure 4.21 d). This seems to overcompensate the loss in the luminescence downconversion process.

This chapter discussed the integration of organic ligands in a diblock copolymer micelle nanoreactor templated wet synthesis. The aliphatic molecules drastically increase the PLQY of LHP NCs to near unity. Furthermore, different lengths of amine ligands can be used to fine-tune the optical properties of bromide and iodide compounds, inducing a blue shift of the emission and absorption properties by short chain ligand incorporation. Additionally, the organic ligands and the polymer micelle form a

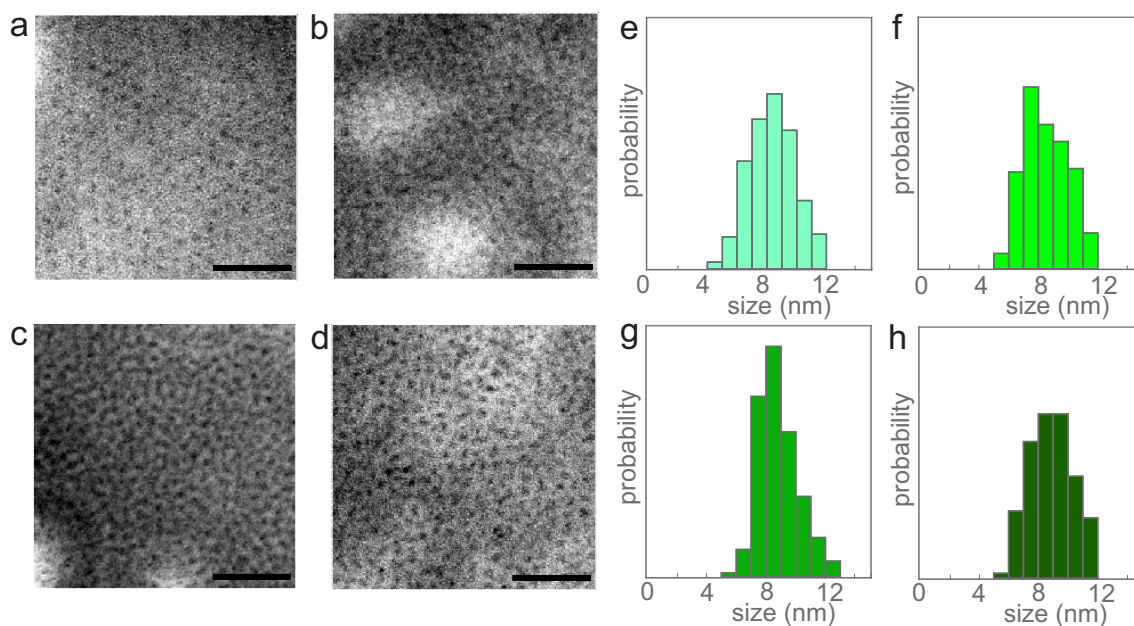


Figure 4.18: TEM Analysis of Doubly Stabilized LHP NCs TEM images and corresponding size distributions of doubly stabilized MAPbBr₃ NCs synthesized with different ligands ((a), (e): hexylamine; (b), (f): octylamine; (c), (g): dodecylamine; (d), (h): oleylamine). Scale bars correspond to 100 nm.

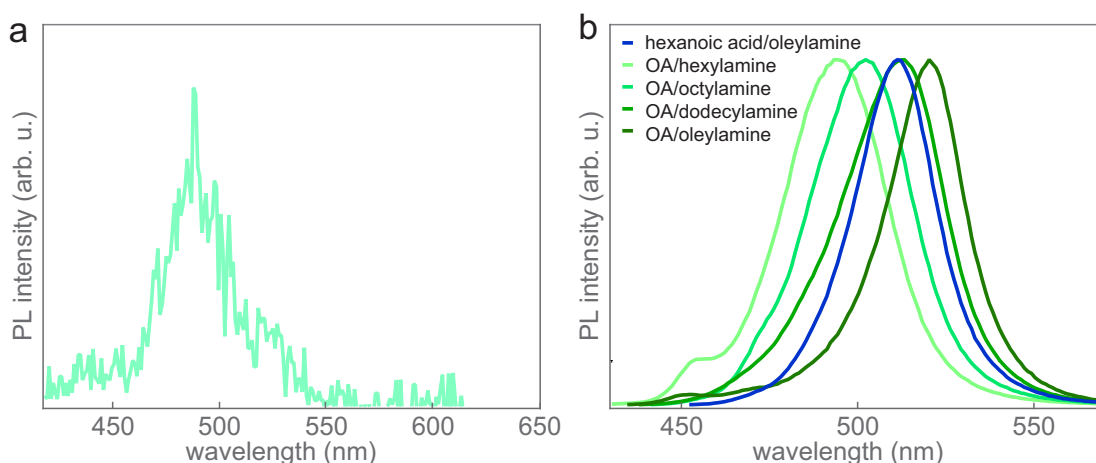


Figure 4.19: Optical Properties of Doubly Stabilized LHP NCs Synthesized with Organic Ligands (a) PL spectrum of doubly stabilized MAPbBr₃ NCs comprising butylamine and oleic acid. Due to the high volatility of butylamine, it hardly participates in the synthesis and the PL intensity of the resulting NCs is weak. (b) PL spectra of doubly stabilized MAPbBr₃ NCs comprising different ligand lengths. Green curves correspond to samples synthesized with oleic acid and different amine ligands, the blue curve shows the PL of a sample comprising a shorter acid ligand (hexanoic acid) and oleylamine.

stabilized system around the LHP NCs, efficiently protecting them from degradation through water, heat, and UV illumination. To show the integrability of doubly stabilized NCs, a downconverter device comprising a blue OLED and doubly stabilized MAPbBr₃ NCs was fabricated. A strong and spectrally pure green luminescence was observed, proving the possibilities this synthesis method provides. Doubly stabilized LHP NCs combine high stability and excellent optoelectronic properties and are ideal candidates for lighting applications. To further push their limits and allow direct charge and energy injection, additional research towards conducting polymers and ligands is necessary and ongoing.

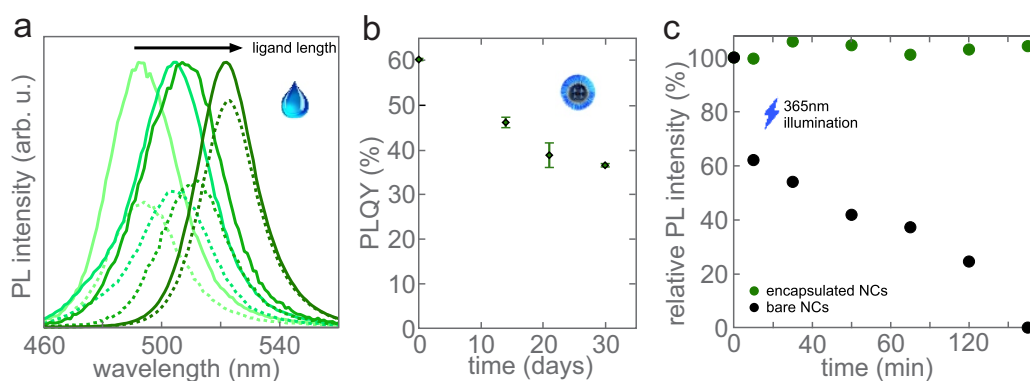


Figure 4.20: Stability of Doubly Stabilized LHP NCs (a) PL spectra of doubly stabilized MAPbBr₃ NC films with varying amine ligand length after synthesis (solid lines) and after submersion in water for 12 hours (dashed lines). (b) Evolution of the PLQY of doubly stabilized perovskite NC films stored in ambient conditions for 30 days. (c) Development of the PL intensity of perovskite NC dispersions comprising doubly stabilized NCs (green) and ligand encapsulated NCs (black) illuminated with UV light.

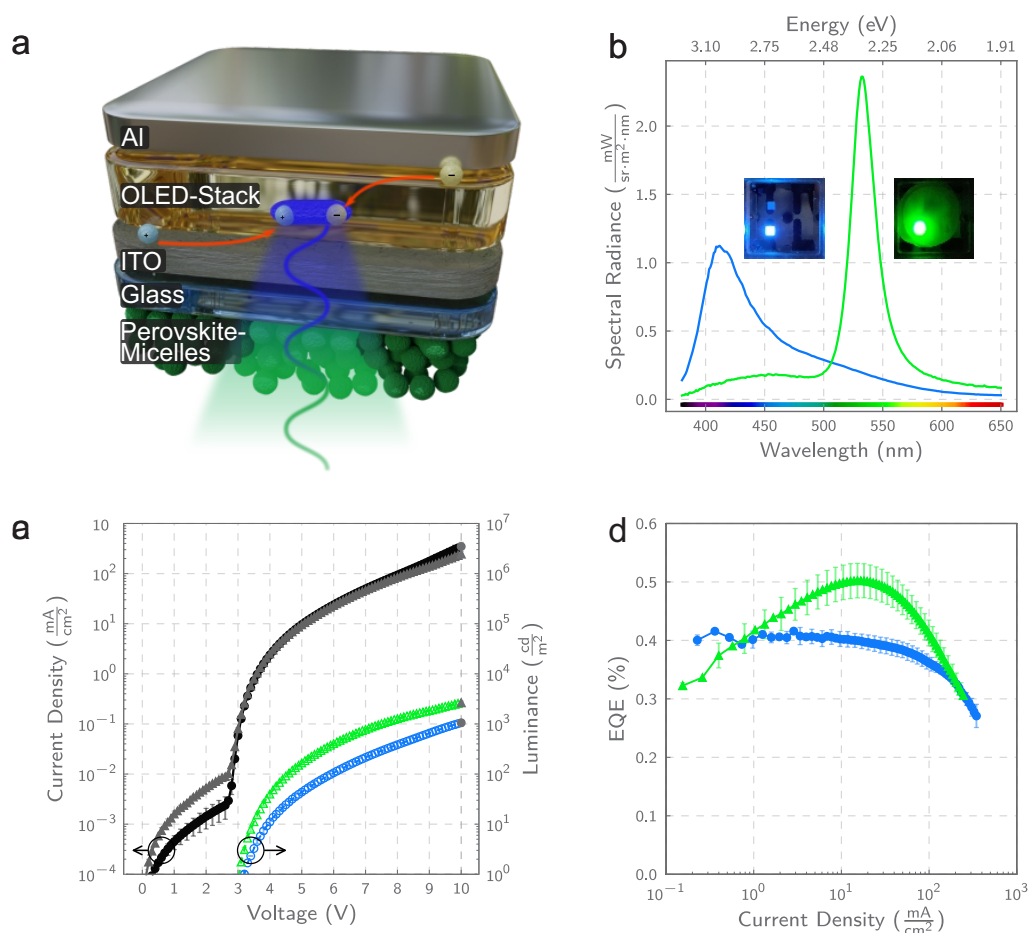


Figure 4.21: Perovskite Downconverter-OLED (a) Schematic OLED stack of the blue pump OLED on the top side of a glass substrate with the perovskite NC downconversion layer applied to the bottom side of the glass substrate. (b) Electroluminescence (EL) emission of the OLED (blue) and the DC-OLED (green). Photographs of the two devices are shown as insets. (c) Current density and luminance of the bare OLED (black, blue) and the entire device (grey, green) dependent on the driving voltage. (d) EQE of the bare OLED (blue) and the DC-OLED (green) as a function of the current density.

4.4 Summary

In summary, we introduced a ligand-free wet synthesis routine for LHP NCs. Diblock copolymer micelles are used as nanoreactors to grow NCs in protected and confined environments. The emission of encapsulated LHP NCs can be varied in the visible spectrum by adjusting the halide ion composition. The samples display a remarkable durability with thin films of micelle-encapsulated NCs retaining an astoundingly high PL intensity after 200 days in ambient conditions. The polymer shell effectively improves the resistance against external degradation factors like UV light and oxygen. Additionally, encapsulated NCs thin films show pronounced PL emission after 70 days submerged in water and are completely impermeable for halide ion migration. This opens up numerous options for deploying micelle-encapsulated LHP NCs, for example, in heterostructures, energy funnels, and lighting applications.

To enhance the synthesis yield and optimize the synthesis parameter, DLS was used to elucidate distinct synthesis steps. The CMC was determined for different polymers, and the amount of used polymer could be at least halved, drastically reducing the costs. Furthermore, the time necessary for ions to diffuse into the micellar core was analyzed, and the synthesis routine was adapted to a more time-efficient procedure.

Lastly, the synthesis routine was extended by introducing organic ligands to enhance the optical performance of LHP NCs. With the use of organic ligands, the PLQY of micelle-encapsulated NCs could be boosted to near unity while simultaneously introducing additional protection from the environment. The NCs' emission can be further fine-tuned by using different ligand lengths since shorter amine ligands cause a blueshift of the PL maximum. Finally, doubly stabilized LHP NCs were successfully used as optical downconverters with an OLED to prove the applicability of the doubly stabilized system.

5

Optimizing the Emission Properties of Perovskites Nanocrystals

This chapter introduces and analyzes the synthesis and properties of $\text{Cs}_{n-1}\text{Pb}_n\text{Br}_{3n+1}$ nanoplatelets. Firstly, the advantages of using anisotropic nanocrystals as light sources are discussed by simulating their optical performance limits based on the orientation of the transition dipole moment. The anisotropic morphology emphasizes the light outcoupling in one direction. In a second step, machine learning algorithms are applied to optimize and fine-tune the synthesis parameters to obtain more homogeneous nanoplatelet samples. Thereby new nanoplatelet thicknesses are discovered and fabricated. The tunability of the emission color of quasi-two-dimensional nanocrystals further emphasizes their qualification for lighting applications. Lastly, the synthesis procedure is investigated in-situ by simultaneous time-resolved X-ray diffraction and PL spectroscopy. This allows the identification and optimization of distinct synthesis steps.



5.1 Directional Emission in Quasi-2D Nanoplatelets

LHPs have drawn a lot of attention due to their unique optoelectronic properties, as discussed in [Subsection 2.2.3](#). Recently they are handled as promising candidates for light emission applications. Especially LHP NCs, with their high defect tolerance, easy processibility, and high PLQY, are at the center of attention. Nowadays, they are typically used as optical downconverters competing with conventional quantum dots like InP. In addition to optically pumped systems, the direct electrical excitation of LHP NC emitters is also still under extensive investigation. The first perovskite-based LED (PeLED) was reported in 2014 by Tan et al.¹⁰ with EQEs of 0.1% (green emission) and 0.23% (red emission). Current PeLEDs have been improved to around 20% EQE for green and red emission.^{31,143} However, blue emitting devices are still lagging with an EQE of around 2%.¹⁴⁴ Reasons for that are low PLQYs for Cl-containing perovskite systems and difficulties in the charge injection into CB and VB. As described in [Subsection 2.2.3](#), Bohn et al. developed a synthetic process for obtaining inorganic $\text{Cs}_{n-1}\text{Pb}_n\text{Br}_{3n+1}$ NPLs with high PLQY and narrow and tunable emission. For these systems, strong quantum confinement effects are exploited to select a specific emission wavelength by controlling the thickness of the NPL with a monolayer sized precision. Concerning display applications especially blue emission with wavelengths less than 475 nm is of great interest to meet the requirements for the BT2020 television standard.¹⁴⁵ To optimize the integration of LHP NCs in lighting applications, a fundamental understanding of the factors regarding the efficiency is required. In cooperation with the group of Prof. Wolfgang Brütting at the University of Augsburg, we investigated the theoretical performance limit depending on the emissive properties of perovskites NCs. Figures and results from this chapter are published in [Reference \[146\]](#).

The performance of an LED is often expressed in the EQE as follows:

$$\eta_{EQE} = \gamma \cdot q_{eff} \cdot \eta_{out} \quad (5.1)$$

In this case, γ denotes the charge carrier balance, i. e., the ratio of electrons and holes in the emitter layer. It is controlled through the device structure and assumed to be unity here. The effective radiative quantum yield q_{eff} contains material specific properties like the intrinsic QY (directly measurable via PLQY) and the influence of the Purcell effect. Lastly, η_{out} describes the outcoupling efficiency of the emission, which can not be measured but needs to be derived from numerical simulations. For this, individual properties of the emitter layer, like the film thickness and the refractive indices, are important input parameters. An additional factor to the outcoupling efficiency is the emitter's radiation pattern, which is dependent on the orientation of the transition dipole moments (TDM) and the refractive index of the emitter layer (EML). Herein, we introduce a figure of merit that combines these factors. The so-called alignment constant quantifies the angular distribution of emitted power as follows:

$$\zeta = \frac{\sin^2 \varphi_{TDM}}{n_{EML}^4 - \sin^2 \varphi_{TDM} (n_{EML}^4 - 1)} \quad (5.2)$$

With n_{EML} resembling the refractive index of the EML and φ_{TDM} the angle of the emissive TDM with respect to the substrate surface. The dimensionless alignment constant takes values between 0 and 1; thereby, 0 corresponds to a horizontally oriented TDM and 1 to a vertically oriented one ([Figure 5.1](#)).

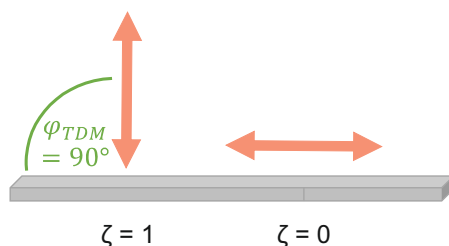


Figure 5.1: Schematic Description of the Alignment Constant The alignment constant describes the orientation of the transition dipole moment (TDM) of an emitter. A value of 1 describes a TDM vertically oriented to the substrate surface, contrary to an alignment constant of 0 which describes a horizontal orientation.

For a maximized outcoupling efficiency, the alignment constant is desired to be as small as possible to enhance the outcoupling of the emitted light out of a device. According to Equation 5.2, this can be achieved by reducing the TDM angle or by increasing the refractive index of the emitter. Optical simulations were performed to determine the effect of these parameters, assuming LHP NCs as emitters in a classic OLED stack. The simulations extract the alignment constant depending on the TDM angle, the refractive index, and the resulting theoretical outcoupling efficiency. The results can be seen in Figure 5.2 a. LHP emitter layers, in general, show a higher possible EQE than, e.g. organic emitters due to their high refractive index from heavy elements like lead. The refractive index for a perovskite EML is approximated by the Bruggemann approach by a combination of a high refractive index of the inorganic perovskites and a low refractive index of the organic ligands. The TDM angle for LHPs is highly dependent on the morphology of the NCs. CsPbBr₃ nanocubes show only weak confinement in all dimensions and thus exhibit no preferential alignment of the TDM (Figure 5.2 b). CsPbBr₃-based NPLs, however, show strong confinement effects in one dimension, consequently restricting the TDM in its orientation in the plane of the NPL. Thus, enhanced light extraction can be achieved by purposely aligning the NPLs parallel to the substrate surface.

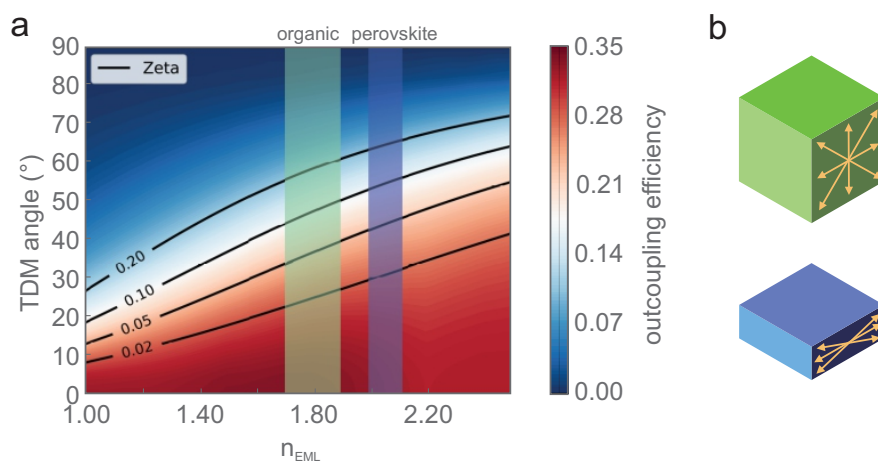


Figure 5.2: Simulations of the Outcoupling Efficiency Depending on the Refractive Index and TDM Angle of an Emitter (a) The outcoupling efficiency was simulated depending on the refractive index and the TDM angle of an emitter. The resulting alignment constant is indicated in black lines along the graph. Green and blue marked areas indicate current positions of common organic and perovskite emitters, respectively. A beneficial behavior for materials with a higher refractive index and reduced TDM angle is obvious. (b) Schematic depiction of the TDM orientation (orange) in 3D materials (green) and confined 2D materials (blue). Confinement of the TDM angle increases the outcoupling efficiency.

Radiation patterns were measured and analyzed to prove the advantageous emission properties of one-dimensionally confined NPLs. Thin films comprising flat-lying NPLs were fabricated, and angular

dependent radiation patterns were taken. A resulting emission pattern is shown in Figure 5.3 for 3 ML NPLs. The spectra can be modeled by a process described in the literature; the fit shows a good agreement of the data.¹⁴⁷ The value of the alignment constant can be extracted from the fit and in the case of 3 ML NPLs, yields an alignment constant of 0.025.

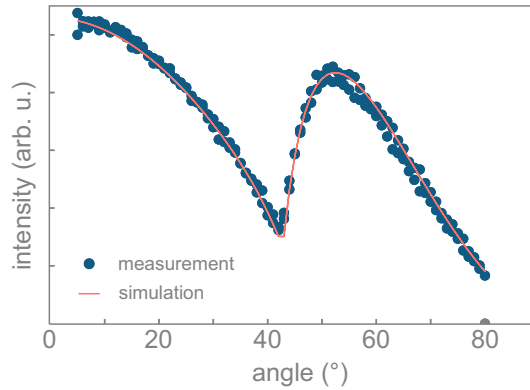


Figure 5.3: Angular Dependent Radiation Pattern of 3 ML NPL Angular dependent radiation pattern of 3 ML NPLs (blue dots) and the simulated pattern (red line). The simulation is used to obtain the alignment constant.

The alignment constant was determined for each NPL thickness (2-6 ML). The results are shown in Figure 5.4. 6 ML NPL exhibit the highest value with an alignment constant of 0.062, which is slightly lower than the one of weakly confined CsPbBr₃ nanocubes from literature, as expected.¹⁴⁷ With decreasing NPL thickness, the alignment constant decreases as well, down to 0.018 for 2 ML NPLs.

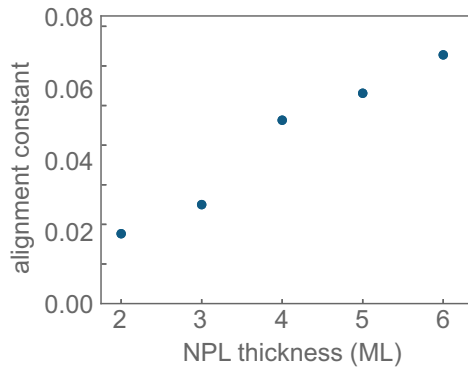


Figure 5.4: Alignment Constant of Each NPL Thickness Values of the alignment constant for each NPL thickness between 2 and 6 ML. As the thickness of the NPL decreases, the TDM becomes progressively more confined to a horizontal orientation, beneficial for enhanced outcoupling.

Figure 5.5 shows the theoretic outcoupling efficiency of LHP nanocubes and NPLs as well as the ones of common organic emitters in dependence of the TDM angle, and the refractive index of the emitter. The benefit of the higher refractive index of LHP emitters is clearly visible by a higher overall outcoupling efficiency. The optimized outcoupling is most likely based on a decreased surface plasmon polariton coupling which is inversely correlated to the TDM angle.

Figure 5.6 shows the theoretical EQE of the related materials with respect to their alignment constant and intrinsic PLQY. For CsPbBr₃ nanocubes with near-unity PLQY the maximum device efficiency (EQE) is limited to 20% due to their alignment constant of 0.07. For NPLs, the alignment constants are significantly lower, which pushes the limits of maximum EQE to higher values, up to 28% for 2 ML NPLs. At the current state, however, NPLs can only reach EQEs of around 15% since their enhanced

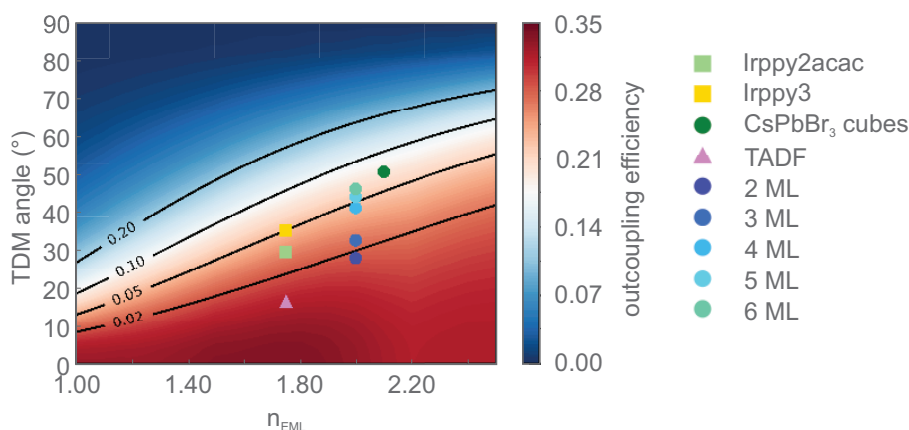


Figure 5.5: Outcoupling Efficiency Limits of Perovskite-Based LEDs The theoretic outcoupling efficiency limit for LHP NCs and some prototypical organic emitters¹⁴⁸ in dependence of the TDM angle and the refractive index of the EML. The values of the alignment constant decrease for decreasing NPL thickness and, consequently, light outcoupling increases.

outcoupling is compensated by their non-ideal PLQY in the range of 50 to 70%. To improve the EQE further, the intrinsic PLQY of the samples needs to be improved by optimizing the synthesis including post-synthetic treatments. Furthermore, an encapsulation of the emitter in a high refractive index material can be beneficial for the outcoupling properties, as previously demonstrated in Reference [149].

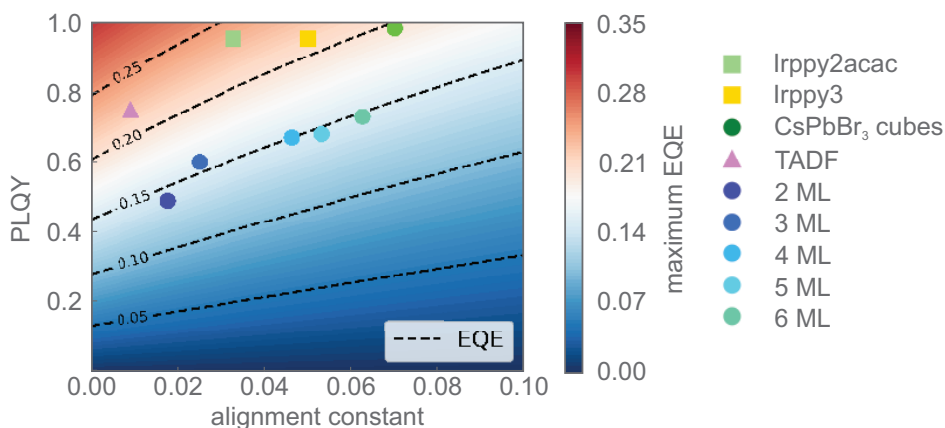


Figure 5.6: EQE Limits of Perovskite-Based LEDs Performance limit of the investigated exemplary PeLED stack for different PLQYs and alignment constants of the emissive NCs. Colored dots indicate the EQE limit of different LHP NCs and common organic emitters. While nanocubes are close to their theoretical maximum of about 20 %, device performance for NPLs could be enhanced by increasing the PLQY of the emissive perovskite. PLQY values were taken from the literature.⁷¹

This chapter shows the superior emissive properties of one-dimensionally confined LHP NCs as emitter in lighting applications. The confinement restricts the TDM in the NCs and allows for an enhanced outcoupling in one direction. Simulations reveal a performance limit of up to 28% for the anisotropic emitter. Nevertheless, Figure 5.6 shows only theoretical performance limits of LHPs as emitter in lighting applications. In reality, blue PeLEDs comprising LHP NPLs exhibit EQEs of less than 1%.¹⁴⁴ The limiting factor, in this case, is not the emitter itself or the emission outcoupling but the energetic states of the VB. The deep-lying bands form an energetic barrier for hole injection, enhancing nonradiative recombination in the device stack. Additionally, further investigations towards enhanced synthesis procedures for achieving higher intrinsic PLQYs and optimized charge injection are necessary.

5.2 Machine Learning Based Synthesis Optimization

Section 5.3 discussed the benefits of using anisotropic $\text{Cs}_{n-1}\text{Pb}_n\text{Br}_{3n+1}$ NPLs as emitters. Confinement in one direction enhances the outcoupling of light emission while their precise tunability of the thickness and, therefore the narrow emission bands allow for a wider color gamut in future applications. The NPLs are fabricated in a wet synthesis, where the resulting NPL thickness is controlled by the ratio of three different precursor solutions as reported in Reference [71] (Subsection 2.2.3). However, the synthesis procedure typically does not yield exclusively the desired NPL thickness, especially for thicker NPLs (4-6 ML), the spectra become broader and more inhomogeneous, indicating insufficiently accurate synthesis parameters. Adapting the routine towards optimized parameters seems crucial to achieve reproducible and highly efficient light emission. Nevertheless, optimizing an emitter regarding the optoelectronic properties suffers from the vast possible number of composition and fabrication parameter combinations, making synthesizing anything but a small percentage of them infeasible. However, most of the common methods for using artificial intelligence require a huge database to begin with. Often open databases for structural and electronic properties are used to train the algorithm, which are not available for our specific synthesis. Therefore, one of the main challenges of this project is the limited starting data set of only 70 syntheses. Consequently, an optimization scheme was needed which could be satisfied with a limited number of data points. In cooperation with the group around Prof. Alessio Gagliardi at the TU München, a unified framework for the accelerated optimization scheme of the synthesis was developed.

The aim was to optimize the synthesis to obtain reproducible, more symmetric, and narrower PL emission by altering the relative ratios of the three precursors, namely Cs-oleate, a PbBr_2 organic ligand solution, and acetone. A spectral quality factor was approximated using Gaussian processes, as of all the Bayesian methods, this proved to be the most suitable for the limited number of available data. The optimization scheme chosen was Bayesian optimization. The process was constrained based on general experimental experience and laboratory constraints in the form of soft Lagrange multipliers. This allowed a decrease in the data demand, as already acquired knowledge was hardcoded into the optimizer. A further constraint was implemented in the form of the output of a random forest classifier that predicts whether a specific composition will result in a monodisperse perovskite sample, allowing the classification of a significant portion of the composition space as infeasible. These constraints alleviated the data strain and allowed for additional tailoring of the process. As a further optimization capability, the determination of compositions resulting in a specific thickness of NPLs, as well as narrow and symmetric PL spectra, was implemented. A neural network was trained to predict the position of the PL maximum and used to constrain the precursor compositions to fall within the emission range ascribed to a specific NPL thickness. The combination of these algorithms produced a robust, data-efficient, and highly targeted optimization scheme that produced tailored compositional suggestions dependent on the desired properties of the NPL sample. The full process of an optimization cycle is schematically shown in Figure 5.7. Existing data sets are analyzed, fed into the algorithm, and used to predict new combinations, which are subsequently synthesized, analyzed, and used for further optimization.

During the NPL synthesis (Subsection 3.1.2), Cs-oleate is added to a PbBr_2 -ligand-toluene solution under vigorous stirring. After 10s, acetone is added as an anti-solvent. After a reaction time of 1 min, the mixture is centrifuged, and the obtained NPLs are redispersed in hexane. For all tested

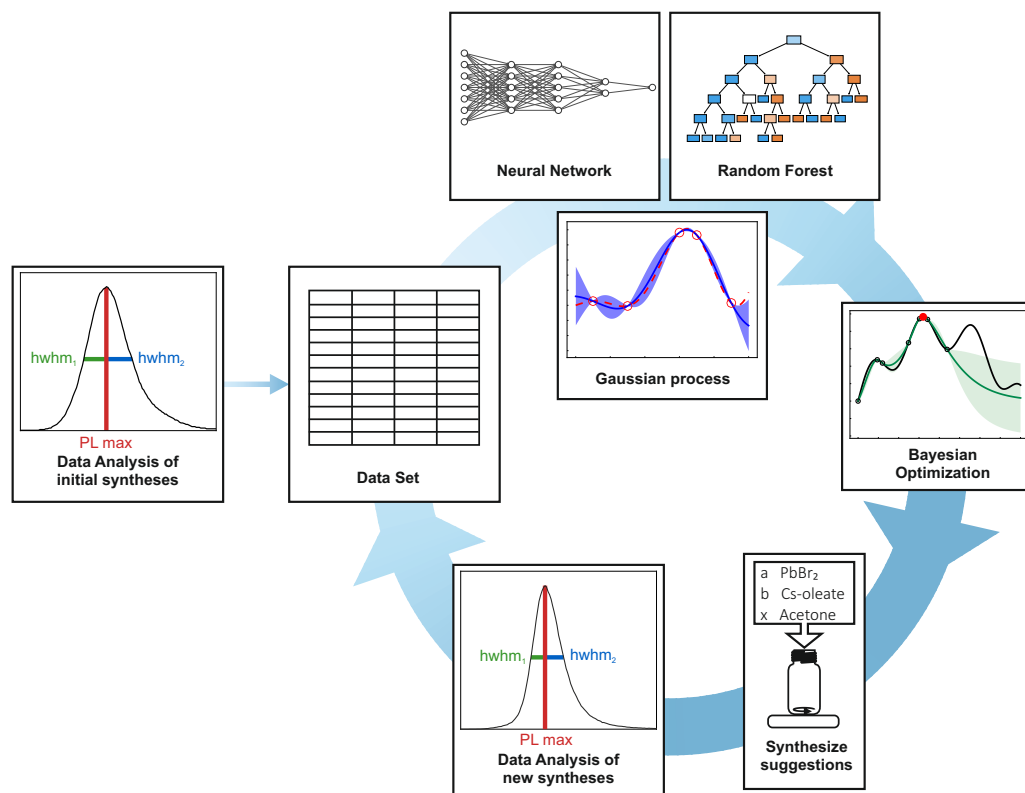


Figure 5.7: Scheme of the Optimization Process Existing data sets are analyzed and fed into the algorithm. Predictions were made and synthesized accordingly via Gaussian processes, random forests, and a neural network. The old and new data sets were used to train the algorithm further. The cycle was repeated up to eight times.

compositions, this procedure remained the same, solely, the volumes of the three precursors were changed.

It is already known that the thickness of a NPL decreases with a decreasing Cs/Pb ratio, as the deficit of the A-site cation limits the amount of perovskite being formed.⁶⁶ Additionally, a larger amount of acetone is reported to be necessary for thicker NPLs.⁷¹ The thickness of a NPL between 2 and 6 ML was found to correlate directly to a specific PL maximum position. This allows a facile characterization of the sample. Since the desired emission for quantum emitters should be as color pure as possible, a quality criterium for syntheses was based on the PL spectra of the samples. The quality factor of a sample considers the narrowness and symmetry of the PL maximum. The quality factor was obtained from normalized PL spectra. This had the dual effect of transforming the spectra in a consistent and comparative manner and giving them the characteristics of a probability distribution. The narrowness (f_{narr}) of a spectrum is traditionally defined by the half-width at half maximum (hwhm). For the symmetry factor (f_{sym}), the PL spectrum is treated as a probability distribution. Both the narrowness and symmetry factors were normalized, bringing both to the range [0, 1]. The final quality factor was chosen as follows:

$$QF = \frac{1}{f_{sym} + f_{narr}} \quad \text{with} \quad f_{sym} = 100 \cdot \frac{\bar{X} - \tilde{X}}{\bar{X}} \quad (5.3)$$

Here, \bar{X} defines the mean of the spectrum and \tilde{X} the median of the spectrum. Each synthesis was evaluated according to the quality factor. Thus, a good synthesis provides a quality factor of 1 while,

a bad synthesis yields a factor of 0. The goal of the optimization process was to maximize the quality factor while predicting the parameters for the desired NPL thickness. The parameters for the optimization process were constrained with soft Lagrange multipliers based on general experimental experience and laboratory limitations. The following restrictions were implemented: the amount of acetone must be at least 30% of the total volume of the synthesis to ensure the function as antisolvent, and the amount of PbBr_2 must be the same or larger than the amount of Cs-oleate to introduce a deficit of A-site cations. Additionally, the syntheses were tested within the applicable ranges of equipment of the laboratory (overall synthesis volume, pipette volume, etc.).

The algorithm was not only used to optimize established NPL thicknesses but also to predict the synthetic parameters for 7 and 8 ML NPLs which had not been isolated to date. Therefore, the PL positions were estimated and used for the prediction. The PL maximum positions used for the optimization are presented in Table 5.1. Each thickness was given an upper and lower limit for the peak maximum to help the algorithm learn.

Table 5.1: Emission Optimum, Minimum and Maximum Position for Each Nanoplatelets Thickness NPL thicknesses and corresponding PL maximum positions including upper and lower limits for the algorithm.

	2 ML	3 ML	4 ML	5 ML	6 ML	7 ML	8 ML
PL maximum (nm)	435	460	477	487	495	501	505
lower limit (nm)	427	455	472	484	491	499	504
upper limit (nm)	438	467	479	489	498	503	507

The algorithm was deployed and generated multiple predictions for seven different NPL thicknesses. The most promising 14 compositions were conducted, and the products were characterized and added to the data set. This cycle was executed eight times. The resulting compositions and their emission color can be seen in Figure 5.8 a in dependence of the three parameters mentioned above. All compositions align along a plane due to the previous set constraints of upper and lower limits for precursor volumes. It can be observed that there is a higher concentration of compositions along the lower part of the graph. This is due to the process of initially exploring the space and later converging to a region and refining the most promising compositions (exploration vs. exploitation). The graph reflects the expected behavior of the synthesis parameter. Thinner NPLs (deep blue emission) were constantly observed for the smallest Cs/Pb ratios. Interestingly the amount of acetone was not as crucial as expected, as all emission colors were observed for a wide range of acetone volumes. This effect will be further analyzed later in this chapter.

During several optimization cycles, the overall peak quality increased significantly, as can be seen exemplary on 5 ML NPLs in Figure 5.8 b. While the spectrum consists of a broad plateau in the starting round, it developed to a more symmetric and narrow shape during several optimization cycles. The PL maximum position was shifted to the desired wavelength, and the optimized parameters provided reproducible results. The improvements can further be seen in Figure 5.9 for all thicknesses, and the impact of the experimental guiding can be clearly observed. The colored lines show the optimized synthesis parameter compared to typically obtained pre-optimization spectra. For each thickness, an improvement is obvious. The PL position and corresponding fwhm are listed in Table 5.2. The fwhm was below 100 meV even for the thicker 5 ML NPL samples, going down to 85 meV for the 2 ML sample. Additionally, 7 and 8 ML NPLs were synthesized and isolated for the first time with this method. They could be synthesized repeatedly with a fwhm of 131 meV and PL maxima at 501 nm

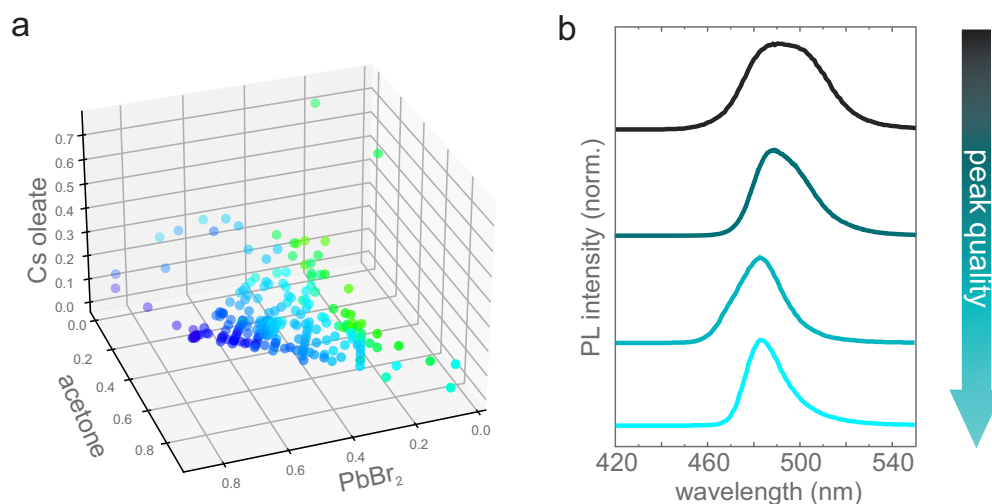


Figure 5.8: Photoluminescence Data from the Optimization (a) All synthesized compositions in the three dimensional parameter space. The data points are colored in their respective emission color and situated along a plane due to restrictions in the parameter space. (b) Evolution of the PL spectra for 5ML NPLs through multiple rounds of applying the optimization algorithm. A significant improvement of the peak shape and position can be observed for each step.

and 505 nm, respectively. The number of syntheses it took for the compositions to converge to these values of approximately 100 is very small, reflecting the algorithm's data efficiency and robustness. The optimized and conventional synthesis parameters can be found in Table 5.3. The parameters still reflect the expected behavior: Increasing Cs/Pb ratio for increasing thickness and additionally a large amount of acetone for thicker NPLs.

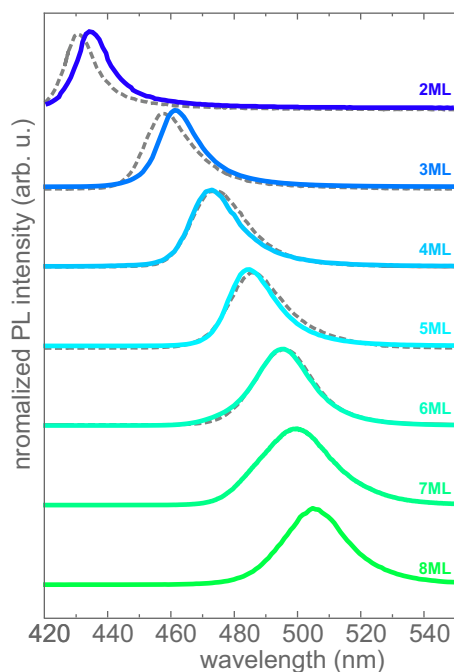


Figure 5.9: Optimized Nanoplatelet Properties PL emission of experimentally verified best syntheses (colored lines) compared to conventional synthesis parameters (dashed gray lines) from Bohn et al.⁷¹

In summary, we have developed a data-efficient framework for optimizing the synthesis parameters for distinct Cs_{n-1}Pb_nBr_{3n+1} NPL thicknesses. The main goal was to reliably synthesize NPLs with narrow and symmetric PL emission at a targeted position. To this end, a Gaussian Process was trained to predict a quality factor based on the narrowness and symmetry of the emission features. The Bayesian

Table 5.2: Characteristic PL Features of Nanoplatelets After Original and Optimized Parameters The PL maxima positions and fwhm for the optimized as well as the initial syntheses of different NPL thicknesses are listed. Data for the conventional NPLs is taken from the literature.⁷¹

	Conventional ratios			Optimized ratios		
	PL position (nm)	fwhm (nm)	fwhm (eV)	PL position (nm)	fwhm (nm)	fwhm (eV)
2 ML	432	11	73	436	13	85
3 ML	459	17	100	461	15	87
4 ML	475	20	109	476	21	114
5 ML	486	21	110	486	19	99
6 ML	496	22	111	494	22	111
7 ML	-	-	-	501	27	133
8 ML	-	-	-	505	27	131

Table 5.3: Precursor Ratios for Conventional and Optimized Nanoplatelet Syntheses The precursor amounts for the optimized as well as the initial synthesis of different NPL thicknesses are listed.⁷¹

	Conventional ratios			Optimized ratios		
	PbBr ₂	Cs-oleate	acetone	PbBr ₂	Cs-oleate	acetone
2 ML	0.583	0.029	0.388	0.680	0.016	0.304
3 ML	0.411	0.041	0.548	0.488	0.024	0.488
4 ML	0.358	0.045	0.597	0.472	0.127	0.401
5 ML	0.294	0.059	0.647	0.299	0.084	0.617
6 ML	0.247	0.062	0.691	0.218	0.020	0.762
7 ML	-	-	-	0.302	0.132	0.566
8 ML	-	-	-	0.096	0.030	0.814

nature of the algorithm helps counter the limited amount of data available by quantifying and analyzing the uncertainty of every prediction. Furthermore, the limited amount of data was compensated by incorporating experimental intuition to identify infeasible domains in the compositional space. These constraints were kept as loose as possible to avoid introducing bias while at the same time cordoning off obviously unsuitable compositions. Lastly, a neural network was trained to predict the peak position, and it proved remarkably accurate, even for a limited number of data points. Consequently, the algorithm was not only able to predict narrow and symmetric PL emission spectra but provided the ability to select a desirable peak position which also allowed the exploration of new samples. New thicknesses were synthesized and immediately used for further analysis of basic physical properties of confined NC systems.¹⁵⁰ The interplay of the above mentioned methods created a robust, data-efficient algorithm that provided synthesis parameters resulting in vastly improved and highly tailored emission properties and additionally enabled the establishment of entirely new samples.

5.3 Color Tunability of Nanoplatelets

After optimizing NPLs for blue emitters, the question arises whether this concept is applicable to the whole visible color spectrum. Fine-tuning of every emitter and its wavelength would widen the color gamut for any display application and allow precise color rendering. The most facile way for perovskite-based systems to achieve this is by changing the halide ion composition. As described in [Figure 2.2.3](#) halide transmutation is widely used to edit emission colors in various samples. In the case of the applied NPL synthesis described in [Subsection 3.1.2](#), it was not successful to directly synthesize either CsPbCl_3 or CsPbI_3 . Thus, a halide ion exchange is conducted to allow precise color picking. The combination of confinement effects and halide content tuning allows for a variety of applications. For the halide exchange, the synthesis is performed in the usual manner as described in [Subsection 3.1.2](#), however, instead of a PbBr_2 enhancement solution, a solution with the desired halide anion is used. By varying the amount of CsPbBr_3 -based NPLs and PbX_2 -enhancement solution various emission colors can be achieved. In case of 5 ML NPL this was done with an enhancement volume of 10, 30 and 50 vol% for PbCl_2 , PbBr_2 and PbI_2 enhancement. [Figure 5.10](#) shows a photograph of the resulting dispersions under UV illumination and [Figure 5.11](#) the corresponding optical characterization. For PbBr_2 , it can be seen nicely that the color does not change but remains sky blue at 487 nm, however appearing brighter with increasing amounts of enhancement solution, the reasons for which will be discussed later. For PbCl_2 enhancement, a clear blue shift of the PL emission can be observed from 477 to 427 nm with 10 to 50 vol% enhancement solution added. The most prominent color change is seen for PbI_2 enhancement treatment. For 10 vol%, the initially blue-emitting 5 ML NPLs show a bright green emission at 514 nm, for 30 vol% it shifts to yellow at 578 nm and for 50 vol% enhancement, an orange/red emission at 612 nm is observed.

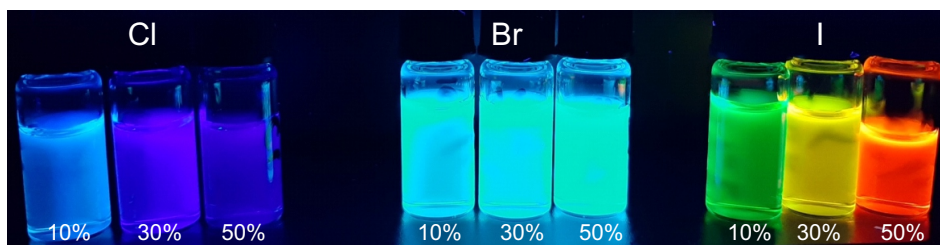


Figure 5.10: Image of Mixed Halide 5 ML Nanoplatelets Under UV illumination Photograph of 5ML CsPbBr_3 -based NPLs treated with 10, 30 or 50 vol% of PbCl_2 , PbBr_2 or PbI_2 enhancement solution, respectively, under UV illumination. The image shows no color change for Br compounds. An increasing blue shift for increasing Cl content is visible. The major changes are observed for different iodide contents, shifting over green and yellow to an orange/red emission.

The corresponding PL spectra illustrate the various trends discussed above in [Figure 5.11](#). By taking the PLQY into account, we can clearly see the effect of the enhancement solution for the Br compounds. The enhancement solution seems to passivate defects in the crystal structure of the NPLs in dispersion as the addition of larger volumes (10 vol% to 50 vol%) facilitates an increase in PLQY from 26% to 75%, causing the solutions to appear brighter. As expected, the PLQY of Cl compounds is weak compared to Br samples but is still high with 16.70 % for the 50 vol% enhancement sample regarding the not optimal structure of CsPbCl_3 and the nonideal excitation wavelength at 400 nm which is near the band edge of CsPbCl_3 compounds. Interestingly, the PLQYs for PbI_2 compounds behave unexpectedly. While the lowest iodide content results in a PLQY of only 7%, it rises for the 30 vol% compound to 47% and up to

94% for the highest iodide content. The near-unity PLQY promotes this sample as a serious contender for red light emission.

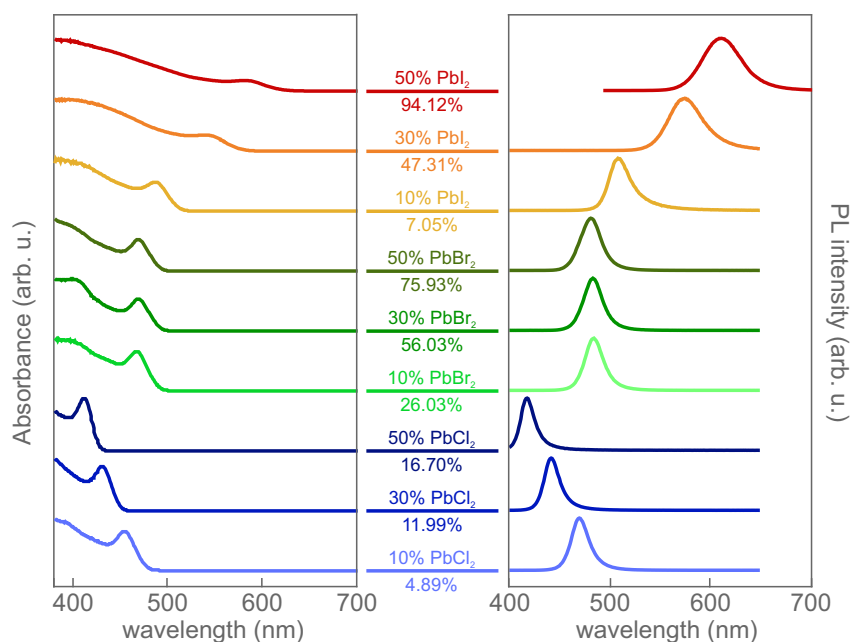


Figure 5.11: Absorption and Photoluminescence Spectra of Mixed Halide 5 ML Nanoplatelets

Absorption and PL spectra of 5ML CsPbBr₃-based NPL treated with 10, 30 or 50 vol% of PbCl₂, PbBr₂ or PbI₂ enhancement solution. The treatment and corresponding PLQY are indicated in the legend situated in the middle section. The absorption spectra show a nice shift of the onset depending on the perovskite composition. Especially for iodide components, the excitonic absorption peak is less pronounced. A similar shift is seen in the corresponding PL spectra. For the bromide compounds, no wavelength shift is observed, only the PLQY vastly increases due to intensified surface trap repair with larger enhancement solution volume.

During the halide ion exchange, the NPLs seem to retain their morphology, as evidenced by TEM imaging of NPLs with different halide compositions. Figure 5.12 shows TEM images of 5ML NPL with 50 vol% of PbCl₂, PbBr₂ or PbI₂ enhancement solution, respectively. For all samples, clear NPL structures are observable.

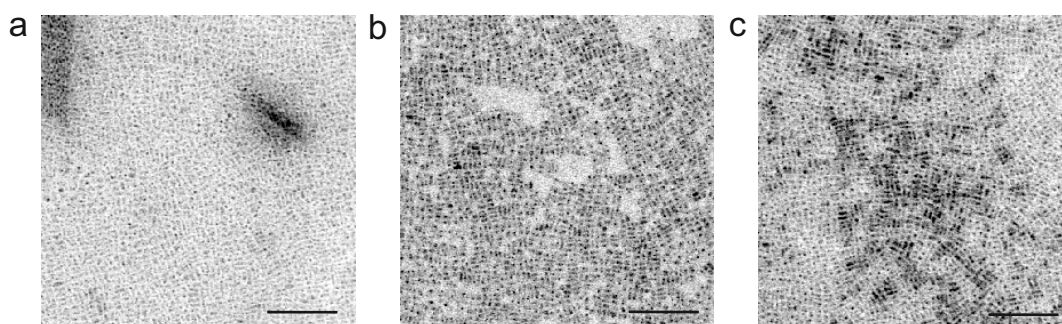


Figure 5.12: TEM Images of Mixed Halide 5 ML Nanoplatelets TEM images of 5ML CsPbBr₃-based NPL treated with 50 vol% of PbCl₂ (a), PbBr₂ (b) or PbI₂ (c) enhancement solution, respectively. In all cases NPL structures are observabel. Scale bars correspond to 100 nm.

The same halide ion exchange concept can be applied to NPLs of different thicknesses of NPLs. The analogous procedure for 4ML NPL yields comparable results with slightly more blueshifted spectra due to stronger quantum confinement. Still, the 50% iodide sample yields the highest PLQY with 79.23%, as can be seen in Figure 5.13.

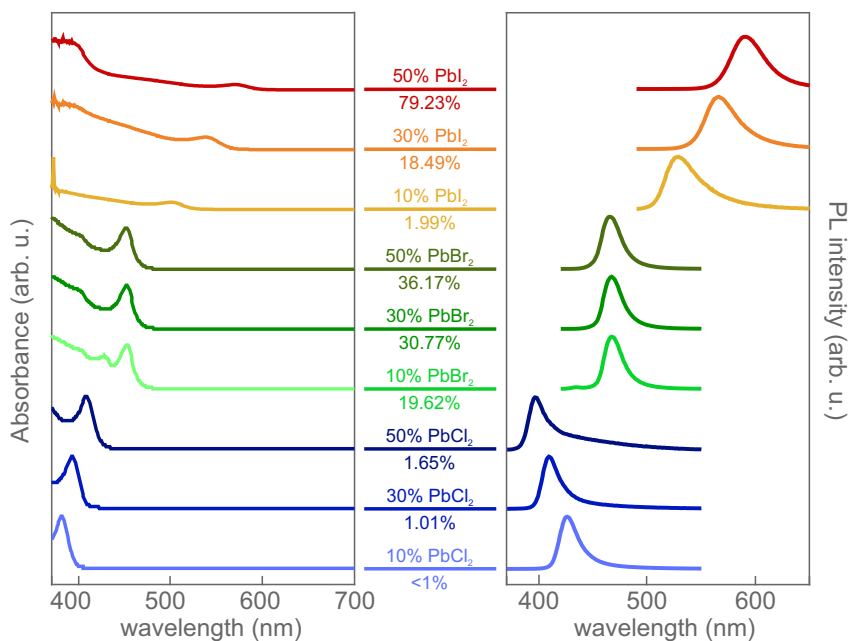


Figure 5.13: Absorption and Photoluminescence Spectra of Mixed Halide 4 ML Nanoplatelets

Absorption and PL spectra of 4ML CsPbBr₃-based NPLs treated with 10, 30 or 50 vol% of PbCl₂, PbBr₂ or PbI₂ enhancement solution, respectively. The treatment and corresponding PLQY is indicated in the legend situated in the middle section. The absorption spectra show a clear shift of the onset depending on the perovskite composition. Especially for iodide components, the excitonic absorption peak is less pronounced. A similar shift is seen in the corresponding PL spectra. For the bromide compounds, no wavelength shift is observed, only the PLQY significantly increases due to intensified surface trap repair with larger enhancement solution volume.

In general, the NPLs seem to retain their morphology and structure during the halide exchange. Even confinement effects appear to remain during the process. Figure 5.14 shows the PL spectra of 2, 3, 4 and 5 ML CsPbBr₃-based NPLs before and after the same PbI₂ enhancement treatment. The intervals between different NPL PL maxima show the same proportions as for pristine Cs_{n-1}Pb_nBr_{3n+1} NPLs. Interestingly, a broadening of the 2 ML emission is observed, this could originate in the mixing of the halide, introducing strain in the perovskite lattice, especially on the lattice surface. Since 2 ML NPLs are built almost exclusively from surface ions, the effect would be more pronounced for thinner NPLs. The stability of mixed halide NPLs was investigated as well. For this, dispersions were characterized by PL spectroscopy immediately after the synthesis and after four months of storage in ambient conditions. Figure 5.15 summarizes the results. Overall, all samples show good stability in dispersion. None or only slight shifts of the PL maximum position are observed, the most change is seen for the 10 % PbCl₂ and 30% PbI₂ samples with a shift of 10 and 12 nm towards the initial sample after the synthesis, respectively.

To sum up, changing the halide ion composition of Cs_{n-1}Pb_nBr_{3n+1} NPLs by a post-synthetic treatment is a fast and easy method to obtain highly efficient emitters with the desired emission in the range of 400 to 620 nm. The NPLs not only keep their morphology but gain stability for well over 60 days. Thereby especially redshifted emitters show a vastly enhanced PLQY approaching unity.

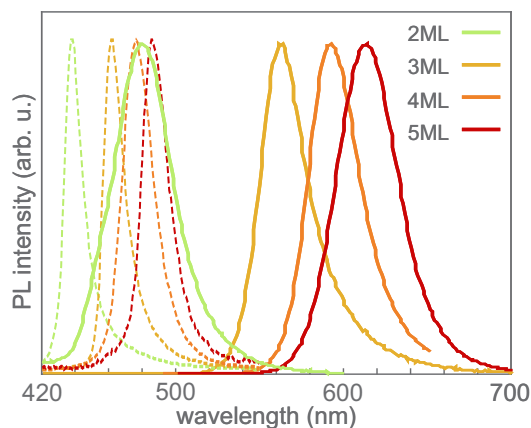


Figure 5.14: Photoluminescence Spectra of CsPbBr₃-based Nanoplatelets with Similar PbI₂ Treatment PL spectra of CsPbBr₃-based NPLs of different thicknesses (2ML, 3ML, 4ML, 5ML) before (dashed lines) and after (bold lines) treatment with the same amount of PbI₂ enhancement. The conservation of the thickness-dependent quantum confinement-induced PL blueshift can be observed.

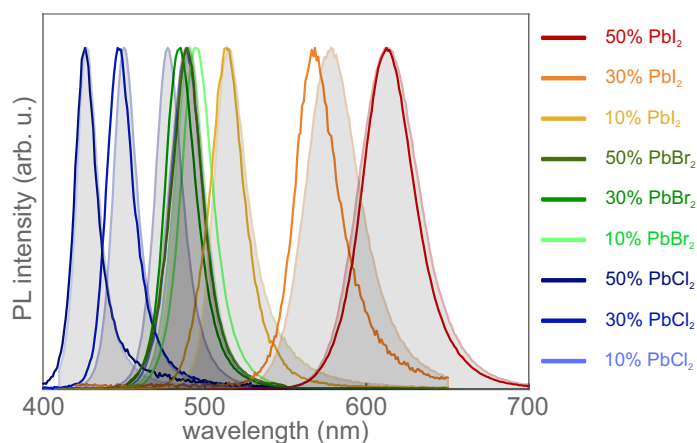


Figure 5.15: Photoluminescence Spectra of Mixed Halide 5 ML Nanoplatelets Before and After 4 Months Storage PL spectra of 5ML CsPbBr₃-based NPL treated with 10, 30 or 50 vol% of PbCl₂, PbBr₂ or PbI₂ enhancement solution, respectively, directly after synthesis (colored lines) and after 4 months of storage in ambient conditions (grey areas). In general, the PL properties are conserved over the time span indicating a great stability of mixed halide NPL dispersions.

5.4 Analyzing Syntheses Processes

To understand and possibly further optimize the NPL synthesis, it is necessary to know what happens at each time interval during the synthesis. Therefore a setup was developed which allowed simultaneous in-situ X-ray scattering and PL spectroscopy. Experiments were performed in Hamburg at the DESY in cooperation with PD Bert Nickel and Kilian Frank, who was also chiefly responsible for processing and analyzing the data obtained from DESY. To control the synthesis remotely, we built a small in-situ cell with stepper motor controlled syringe pumps to inject the precursor solutions (for details see [Subsection 3.2.2](#)). The synthesis itself runs in a glass capillary inside a copper block. The reaction volume is accessible from each side, allowing the simultaneous measurement of SAXS and PL. For a synthesis, the capillary was loaded with the PbBr_2 -ligand-toluene precursor solution and installed in the beamline. The experiments were started remotely, thereby, first, a desired amount Cs-oleate, and after a specific delay time, the acetone was injected. Typically, the synthesis is terminated after 60 s of stirring, however, we elongated the measurement time at DESY to 10 min to investigate possible effects of longer reaction times.

During the experiment, the SAXS signal continuously changes. From the in-situ synthesis of 3 ML NPLs (see [Figure 5.16 a](#)), we identify four different phases (schematically shown in [Figure 5.16 b](#)):

- phase I Initially the background signal of the PbBr_2 -ligand-toluene precursor is visible.
- phase II NPLs begin to form immediately upon Cs-oleate injection. By comparing the ex-situ SAXS signal of 3ML NPLs and the signal at the moment after Cs-oleate injection, we clearly see the existence of 3 ML NPL as the characteristic form factor of NPLs is visible. [Figure 5.16 c](#) compares the characteristic NPL form factor of a finished and purified 3 ML NPL synthesis (blue) and phase II of the in-situ process (orange). The same characteristic features are observable, namely a plateau-like behavior for smaller q , continuing in an intensity drop. Slightly different curve outlines can be attributed to different chemical environments during the measurement. This is particularly interesting since Bohn et al. postulate the formation of NPLs starts with the injection of acetone. Obviously, this is not the case here. Over the time in phase II the SAXS signal for NPLs intensifies indicating slow but gradual growth of the NPLs.
- phase III After the acetone injection, a distinct peak emerges at around 0.05 \AA^{-1} in the SAXS signal. This indicates the formation of larger structures, probably stacks of NPLs. This is caused by a change in the solubility of NPLs in the precursor solution, which is drastically reduced by acetone. By stacking on each other, NPLs can minimize the interaction with the solvent.
- phase IV Over a longer timespan, this 'superstructure' peak becomes sharper and shifts to smaller q values, indicating a continuous growth of the superstructure. Moreover, the second and third order peaks of the superstructure are also visible. This is also an indication for very homogeneous samples and highly structured assemblies.

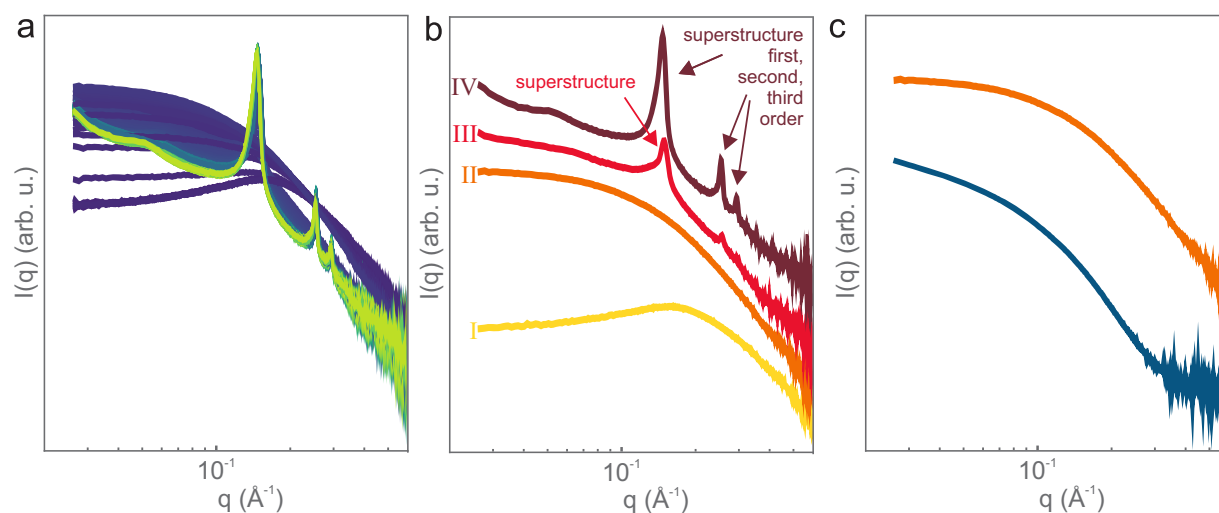


Figure 5.16: In-Situ SAXS on a 3 ML Nanoplatelet Synthesis (a) In-situ SAXS measurements of a 3 ML synthesis over a time span of 10 min. After Cs-oleate injection, an immediate formation of NPLs can be observed while the acetone injection induces the formation of a superstructure which intensifies over time. (b) Clarification of the four identified phases, with single curves from (a); (c) Comparison of phase II (orange) and ex-situ (blue) NPL SAXS signal.

The same behavior can be observed for a 5 ML NPL synthesis, as shown in Figure 5.17. However, the NPLs' structure factor is more pronounced, indicating the formation of thicker NPLs with a larger volume. As for the 3ML synthesis, the four phases are visible in the graph. The superstructure peak emerging after acetone injection is much broader than for 3 ML NPLs. A reason for that could be a more inhomogeneous NPL size distribution.

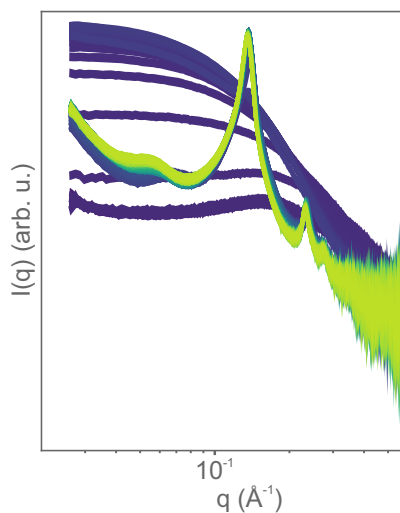


Figure 5.17: In-Situ SAXS on a 5 ML Nanoplatelet Synthesis In-situ SAXS measurements of a 5 ML synthesis over a time span of 10 min. The four different synthesis phases can clearly be seen for thicker NPLs, too.

The in-situ PL measurements of 3 ML NPLs further support the immediate formation of NPLs. After the Cs-oleate injection immediately a PL signal starts to develop at 452 nm quickly shifting towards 460 nm and intensifies over time. An effect through acetone injection after 10 s cannot be observed for the PL measurements. Apparently, the acetone injection does not affect the NC growth. Over the time span of the experiment (10 min), the fwhm decreases continually from 230 to around 150 meV and continues to decrease. The same can be seen for the PL intensity, which slowly continues to increase. Interestingly, even after 10 min of reaction time, no thicker NPLs develop, which raises the

question of why the synthesis is stopped after 60 s. A longer synthesis time seems to improve the optical properties of the resulting NPLs.

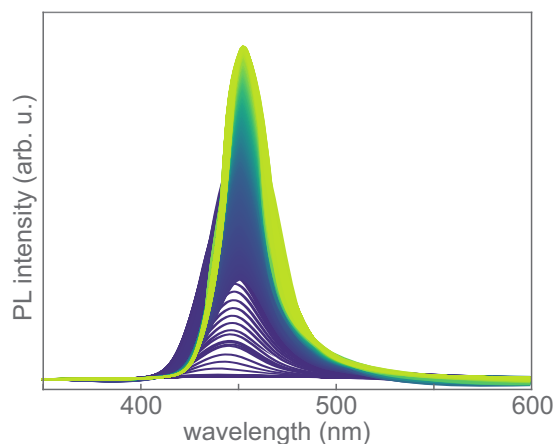


Figure 5.18: In-Situ PL Measurement During the Synthesis of 3 ML Nanoplatelets PL measurements during the synthesis reveal a fast development of the characteristic 3 ML PL emission. The time resolution of the shown graph is 100 ms

Since the NPL formation is induced by the Cs-oleate injection instead of the antisolvent injection, it was investigated what effect the acetone injection actually does. Therefore acetone was injected at different times during the synthesis. The different delay times between the Cs-oleate and acetone injection are chosen as 0, 1, and 100 s and one synthesis was done with first acetone and subsequent Cs-oleate injection (labeled with -10 s). The in-situ SAXS data is shown in [Figure 5.19](#). In all cases, phases I and IV are visible. Phase III, however, is differently pronounced. A clear trend is seen that a more pronounced NPL structure factor is observable with increasing delay time indicating a slow but continuous growth of the NPLs. Only for the -10 s sample, a direct change from precursor to supercrystal signal is seen. Apparently, NPLs form with the Cs-oleate injection and immediately assemble in superstructures if acetone is already present in the precursor solution. This means that contrary to [Subsection 2.2.3](#), the NPL synthesis is not a LARP synthesis but only uses distinct precursor ratios to obtain desired NPL thicknesses independently of an antisolvent or solubilities. The acetone only results in the formation of superstructures which slows the NPL growth and enables the precipitation via centrifuge to separate the NPLs from the precursor solution and change the solvent. Having investigated the standard synthesis, we next focussed on understanding the enhancement steps with the in-situ setup at DESY. To this end a distinct volume (10 vol%) of enhancement solution (PbBr_2 or PbI_2) was injected stepwise into the NPL dispersion after a certain delay time and SAXS and PL signals were acquired for 10 min. This was repeated five more times, for varying enhancement solution volumes. For PbBr_2 enhancement, overall, the PL maximum position redshifts 2 nm after the first enhancement injection but remains constant for every additional injection. Furthermore, with the first enhancement injection, the PL intensity increases by a factor of 2.5 ([Figure 5.20 a](#)). For each following injection the PL intensity first drops followed by a slow and steady increase in intensity but never becomes significantly more than the intensity after the first enhancement injection. This further supports our approach to use only 10 vol% enhancement solution for our synthesis to maximize the effect of enhancing the PL while not adding too many ligands. Furthermore, the SAXS signal develops a kink with increasing enhancement volume ([Figure 5.20 b](#)). Possibly this is caused by a local order of NPLs accompanied with an increasing polydispersity. To make a clear statement about the reason for a change in the SAXS signal, simulations will be critical to find the origin of the SAXS development.

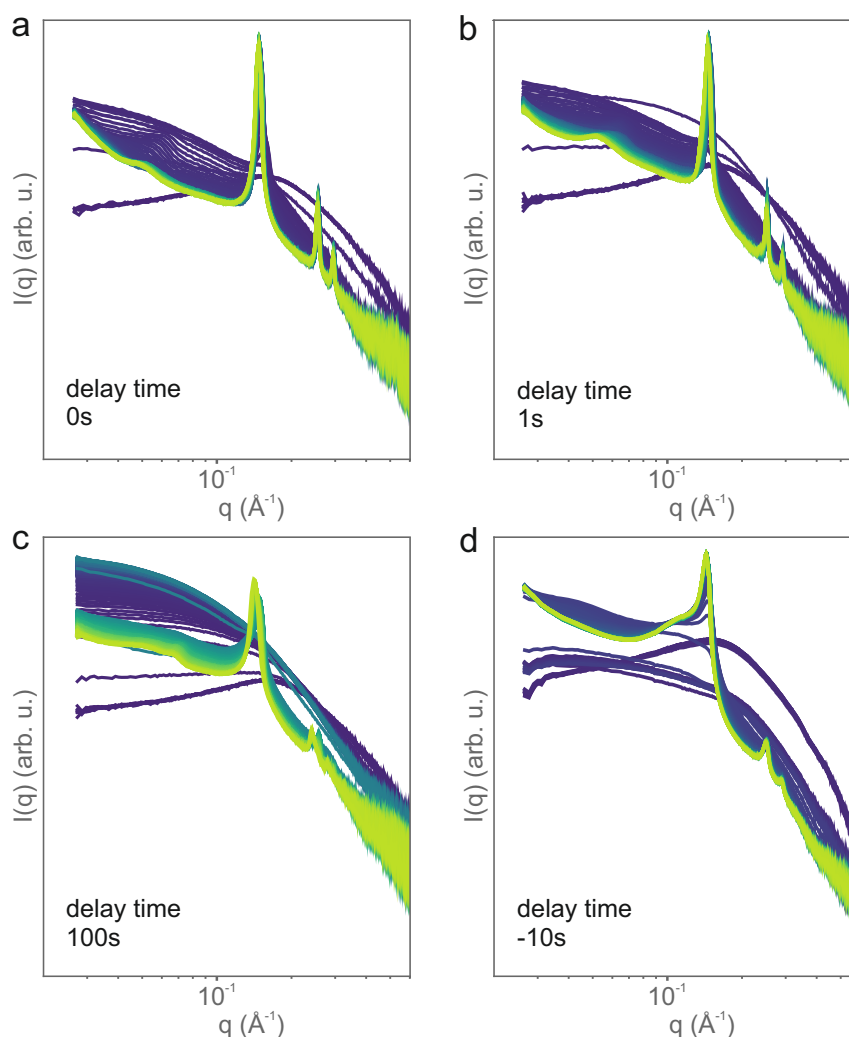


Figure 5.19: In-Situ SAXS on 3 ML Nanoplatelet Syntheses With Varying Delay Time Between Precursor Injections In-situ SAXS on 3 ML NPL synthesis with different delay times between Cs-oleate and acetone injection: (a) 0 s (b) 1 s (c) 100 s and (d) -10 s.

For PbI_2 enhancement, however, the situation is different. In the spectral PL position, the six injection times are clearly observable (Figure 5.21 a). The first injection slowly shifts the PL from 450 to 505 nm. Interestingly, the PL intensity vastly decreases to around 50% of the initial intensity. This indicates an introduction of numerous (surface) traps, enhancing non-radiative recombination paths due to different sized halide ions. With increasing PbI_2 enhancement, the PL shift commences, albeit at a slower rate, while the intensity arises continually. With each injection the PL positions shifts within seconds and remains constant for the following 10 min, except for the first injection. After 50 vol% enhancement (after six injections), the PL maximum is located at 575 nm and the PL intensity 1.5 times the initial one. This is in good agreement with the previous chapter where enhanced PLQYs were found for red emitting NPLs. Interestingly, a small PL emission at 660 nm emerges indicating a complete halide ion exchange for a small fraction of NPLs. Furthermore the same behavior in the SAXS signal as for PbBr_2 enhancement is observed (Figure 5.21 b), the development of a kink for increasing enhancement volumes. Again simulations are necessary to make a detailed statement on the reason of this.

In conclusion, this chapter analyzed distinct synthesis steps in the solution-based $\text{Cs}_{n-1}\text{Pb}_n\text{Br}_{3n+1}$ NPL synthesis. Contrary to Bohn et al., it was found that NPLs form immediately upon the combination of

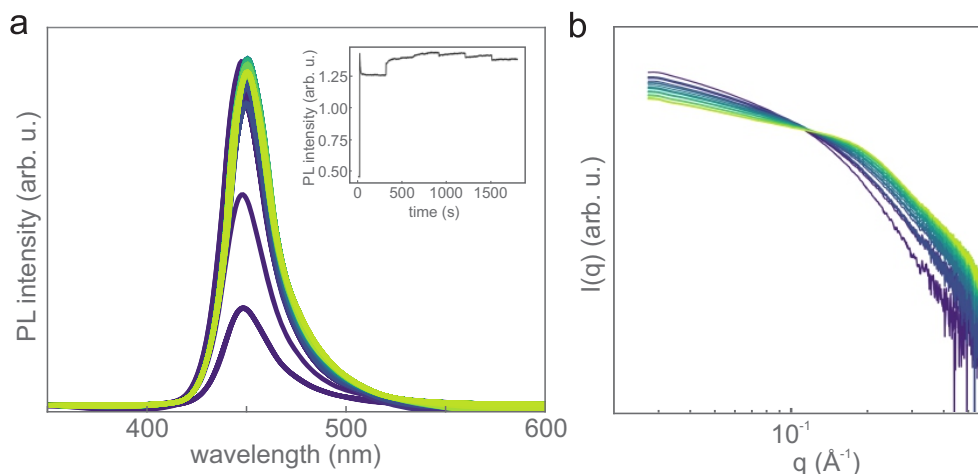


Figure 5.20: In-Situ SAXS on the Enhancement Treatment of 3 ML Nanoplatelets (a) Temporal development of the PL emission during the enhancement process. Subsequent increases of the PL intensity can be observed for each injection step. Inset: Evolution of the PL intensity. Each injection step is clearly observable (b) In-situ SAXS measurement for subsequent injection of PbBr_2 enhancement solution in 3 ML NPLs.

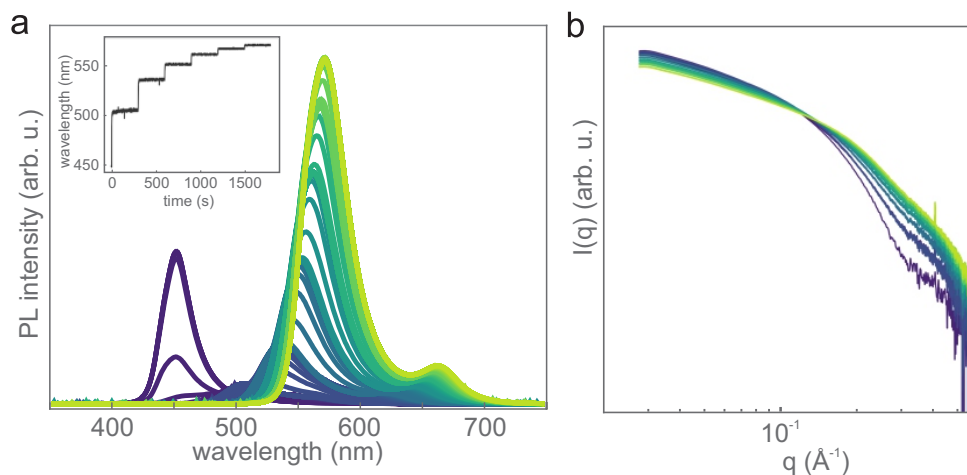


Figure 5.21: In-Situ SAXS on the Enhancement Treatment of 5 ML Nanoplatelets (a) Temporal development of the PL emission during the enhancement process. Subsequent increases of the PL intensity can be observed for each injection step accompanied with a simultaneous PL shift towards larger wavelengths. Inset: Evolution of the PL maximum position over time. (b) In-situ SAXS measurement for subsequent injection of PbI_2 enhancement solution in 5 ML NPLs.

PbBr_2 -ligand-toluene precursor solution and Cs-oleate independently of the anti-solvent. Acetone induces a superstructure formation of ordered NPLs which allows the sedimentation and purification of the sample. This was shown by different delay times of the acetone injection in in-situ synthesis experiments. Furthermore, the structural development of NPLs during lead halide enhancement was investigated. Upon addition of PbBr_2 enhancement the luminescence of NPLs initially increases drastically. For 20 vol% and more, no significant increase in PL intensity is observed, the most prominent effect was observed for the first injection step. For PbI_2 enhancement, a continuous PL shift towards red emission is observed. To date detailed data processing and simulations are necessary to make a statement on the structural change during post-synthetic treatments.

5.5 Summary

This chapter discussed the benefits of using anisotropic $\text{Cs}_{n-1}\text{Pb}_n\text{Br}_{3n+1}$ NPLs as emitters. Firstly, the angular radiation pattern was determined, and the theoretical performance limit in an OLED stack depending on the orientation of the transition dipole moment was calculated. Through this method, a theoretical EQE of 28 % can be reached with NPLs, while isotropic LHP emitters like CsPbBr_3 nanocubes are limited at 20 %. The reason for this is the improved outcoupling efficiency based on the restrictions for the TDM angle introduced by quantum confinement effects.

Secondly, the solution-based synthesis of $\text{Cs}_{n-1}\text{Pb}_n\text{Br}_{3n+1}$ NPLs is analyzed and optimized. The properties of NPLs obtained from a synthesis are mostly dependent on the ratio of three precursors, namely a PbBr_2 -ligand-solution, Cs-oleate, and acetone. Therefore, a machine learning approach is implemented, which predicts the emission pattern and quality of a synthesis based on this ratio. With a training set of only 70 data points, we started to optimize the parameters. After 180 syntheses in total, the emission profile of NPL samples showed a more symmetric shape and was highly reproducible. Additionally, 7 and 8 ML NPLs were predicted and synthesized for the first time with this method. While CsPbBr_3 -based NPL are limited to the emission in the blue to the green region, it is possible to subject the NPLs to a post-synthetic halide ion exchange. Through this, various samples were produced and analyzed that could cover the entire visible spectrum by rationally adjusting the halide composition. Especially red luminescing NPLs with a high iodide content show a remarkably high and well reproducible PLQY of 95 % making them a real competitor for red emission in lighting applications.

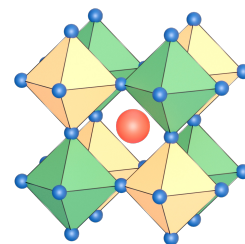
Lastly, in-situ characterization was executed at the DESY in Hamburg to understand the synthesis processes further. The synthesis was conducted in the synchrotron beamline while simultaneously monitoring the PL emission. The exact time point at which the NPLs are formed during the synthesis could be revealed during these experiments. Contrary to the reporting literature, the NPLs form upon Cs-oleate injection in the PbBr_2 -ligand-solution and not only after the acetone injection. The antisolvent injection causes the formation of a superstructure which allows further purification of the sample but is not necessary for the NPL formation. Furthermore, enhancement with PbBr_2 and PbI_2 was investigated in-situ allowing to follow the development of the emission and elucidate the influence of the enhancement solution on the NPLs. While structurally the NPLs remain almost the same, the emission is vastly increased by the enhancement step. This shows the necessity and efficiency of post-synthetic treatments.

$\text{Cs}_{n-1}\text{Pb}_n\text{Br}_{3n+1}$ NPLs are a remarkably versatile and promising research topic. We showed their superior emission features and the easy accessibility of the synthesis process. A detailed understanding of the synthesis and material itself is necessary to further enhance their performance, especially the lack of PLQY.

6

Lead-Free Double Perovskites

This chapter presents a novel synthesis routine for lead-free double perovskite NCs. We combine hot injection and LARP methods to achieve a low temperature-based synthesis for manganese doped $\text{Cs}_2\text{NaBiCl}_6$ NCs. The process is conducted in ambient atmosphere, which drastically enhances the simplicity of the routine. We demonstrate the synthesis of $\text{Mn}:\text{Cs}_2\text{NaBiCl}_6$ NCs with optical properties comparable with data from the literature obtained via hot injection synthesis. Additionally, we identify distinct photoluminescent features of the underlying system and propose strategies to optimize the optical performance. Furthermore, the NCs show great stability in ambient atmosphere, which vastly facilitates the investigations and experiments with lead-free perovskite NCs.



6.1 Manganese Doped $\text{Cs}_2\text{NaBiCl}_6$ Nanocrystals and Their Optical Properties

Research for the synthesis of LFDPs is still ongoing and far from optimized. As described in [Figure 2.2.4](#), most LFDP NC syntheses are hot injection-based and require a complicated inert setup and the knowledge of how to handle it. We worked on a more facile synthesis approach with a combination of hot injection and LARP processes. Herein, we present $\text{Mn}:\text{Cs}_2\text{NaBiCl}_6$ NCs, synthesized in ambient atmosphere at moderate temperatures. For the general synthesis of $\text{E}:\text{A}_2\text{CDX}_6$, stoichiometric amounts of metal precursors, Cs_2CO_3 , NaOAc , BiOAc_3 and MnOAc are dissolved in oleic acid at 140°C . After dissolution, the synthesis mixture is heated to the reaction temperature (varying between RT and 120°C), and toluene, as well as oleylamine, are added. After complete mixing, TMSCl is injected under vigorous stirring, followed by acetone after 10 s. The mixture is stirred for another 60 s before the synthesis is stopped by centrifugation. Optional purification steps using antisolvent can be performed afterward, if desired. The detailed synthesis procedure with exact measurements can be found in [Subsection 3.1.3](#).

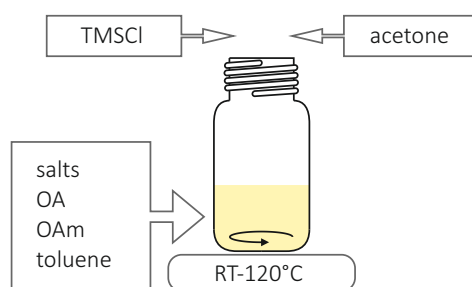


Figure 6.1: Synthesis Scheme for Lead Free Double Perovskites The synthesis for LFDP NCs is a combination of hot injection and LARP processes. Metal salts and organic ligands are dissolved in toluene and brought to reaction temperature (RT to 120°C). Afterwards TMSCl is added followed by acetone after 10 s. After 60 s reaction time the mixture is centrifuged and used as extracted or purified subsequently.

The undoped species $\text{Cs}_2\text{NaBiCl}_6$ can be characterized by an absorption peak around 320 nm and no significant PL emission footprint (compare [Figure 6.2](#) dashed lines). The small PL peak at 400 nm which is present in all samples is assigned to toluene, as confirmed by reference measurements. The lack of emission was expected, since this material is shown to possess an indirect bandgap. This is contrary to previously published data on undoped $\text{Cs}_2\text{NaBiCl}_6$ (see [Figure 2.16](#)) which present luminescence of undoped material around 375 nm and 425 nm, respectively.^{114,115} Reference measurements show that these PL peaks are mistakenly assigned to LFDP structures while they originate in oleate species, as can be seen in [Figure 6.3](#). The synthesis of $\text{Mn}:\text{Cs}_2\text{NaBiCl}_6$, containing 10% Mn, yields a colorless dispersion that exhibits orange luminescence upon UV-illumination (compare [Figure 6.2](#)). UV-Vis spectroscopy reveals a sharp absorption peak around 350 nm, while PL spectroscopy reveals a prominent, broad PL emission peak around 595 nm using a 355 nm excitation. These observations are in excellent agreement with previously published data from $\text{Mn}:\text{Cs}_2\text{NaBiCl}_6$ NCs fabricated by hot injection methods presented in [Figure 2.16](#).^{114,115}

Commonly used purification steps are employed to remove excess ligands or ions from the LFDP dispersion. Acetone is added as an antisolvent before centrifugation and the precipitate is subsequently redispersed in toluene. While the purification steps do not affect the absorption and PL characteristics of the sample, they have an immediate effect on the PLQY. The PLQY increases from nearly zero to

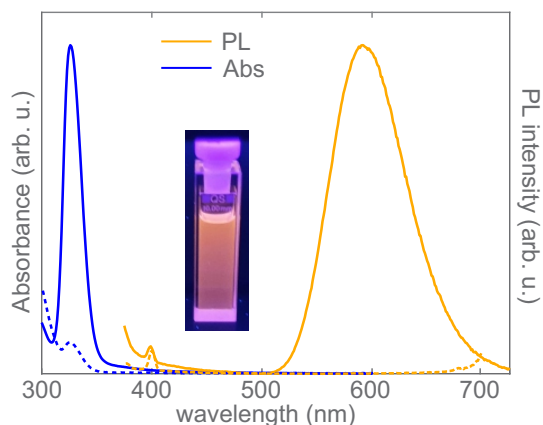


Figure 6.2: Absorption and Photoluminescence of Mn:Cs₂NaBiCl₆ Absorption and PL spectra for undoped (dashed lines) and doped (bold lines) Mn:Cs₂NaBiCl₆. The undoped species shows a small absorption peak at 320 nm and no significant PL emission. The doped sample exhibits a pronounced excitonic absorption peak around 350 nm and a distinct emission centered around 595 nm. The inset shows the emission of the NCs dispersion under UV-illumination.

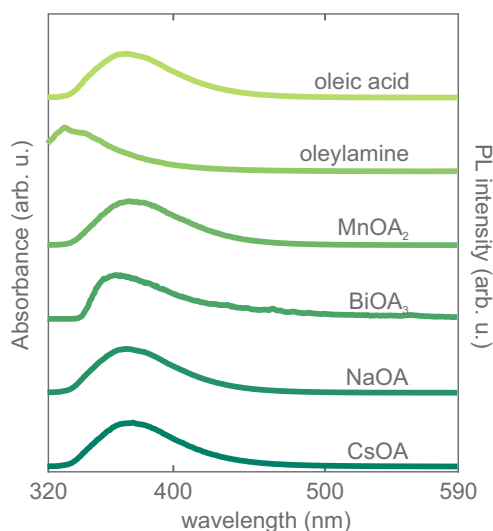


Figure 6.3: Photoluminescence of Metal Oleates PL spectra of toluene, oleic acid, oleylamine and various metal oleate species used in this thesis. Reference PL spectra are used to identify the origin of emission signals.

2.2% within three steps (Figure 6.4). Interestingly, whether or not ligands are incorporated into the purification step has no obvious effect on the resulting optical properties.

Structurally, the synthesis approach yields squarish shaped NCs with a relative size of 10 ± 2 nm upon purification (Figure 6.5 a). Repeated purification steps appear to alter the morphology of the LFDPs drastically (Figure 6.5 b). While they maintain the optical properties of unwashed NCs (see Figure 6.4), TEM images show a greater inhomogeneity in size and shape with sizes ranging from 10 to 30 nm indicating agglomeration and fusion of NCs. This behavior is often observed for NCs in dispersion with a deficit in organic ligands. Interestingly the addition of further ligands did not prevent the morphological changes.

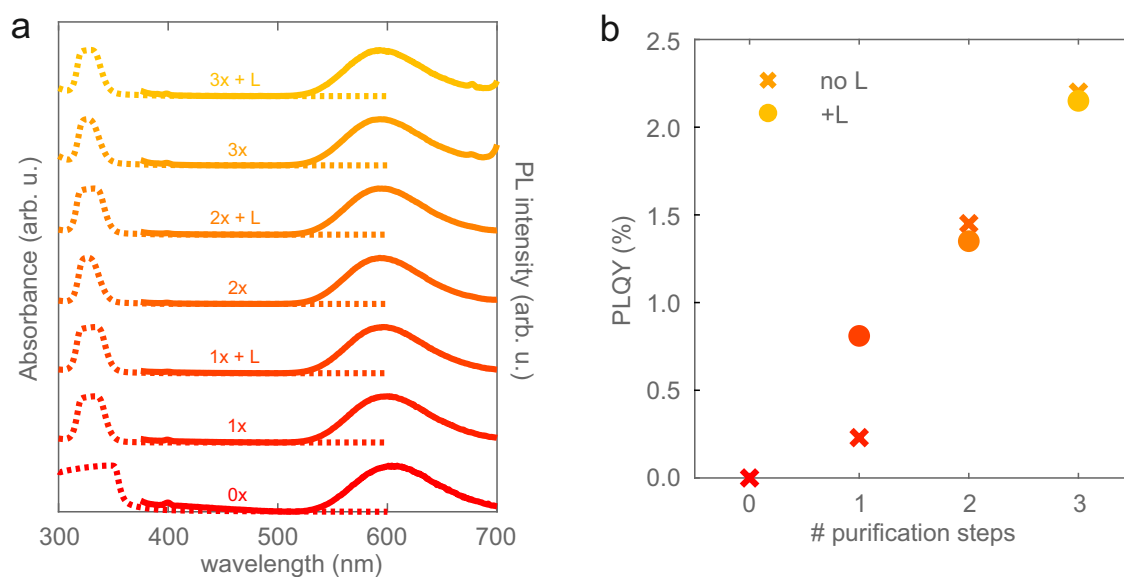


Figure 6.4: Impact of Repeated Purification Multiple purification steps were tested with and without the addition of further ligands (marked with '+L'). While the absorption and PL spectra show no noteworthy change for zero to three purification steps, the PLQY is hugely affected by them. With each purification step, the PLQY increases, resulting in a PL of 2.2% after three steps. Interestingly, the addition of further ligands has no substantial effect.

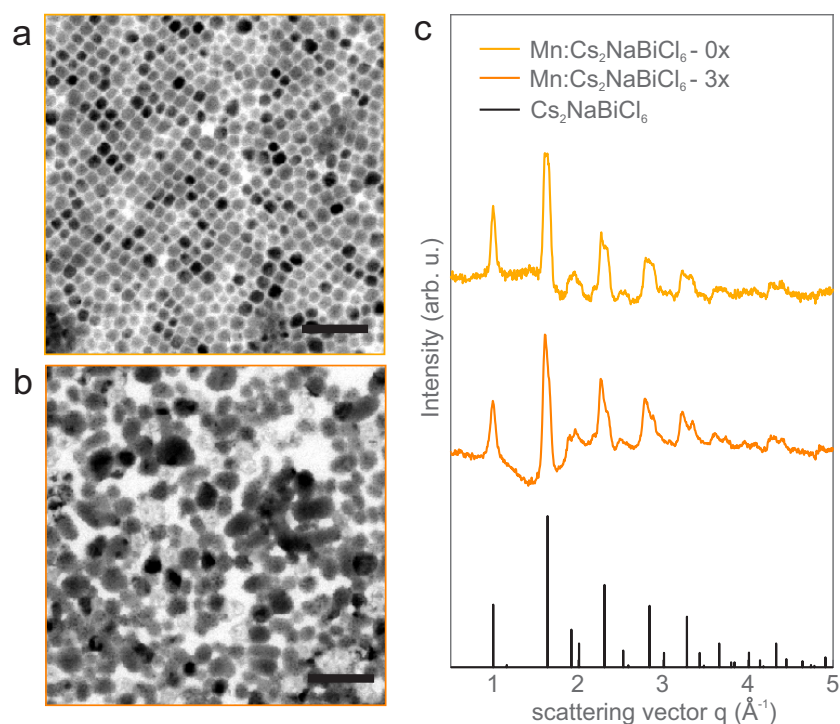


Figure 6.5: Structural Characterization of $\text{Mn}:\text{Cs}_2\text{NaBiCl}_6$ NCs The morphology of the NCs, is hugely affected by the purification. TEM images of unpurified NCs show homogenous, round shaped NCs (a), they lose their integrity after repeated purification steps (b), resulting in a greater size distribution. Scale bars correspond to 100 nm. (c) GIWAXS analysis of unpurified and three times purified $\text{Mn}:\text{Cs}_2\text{NaBiCl}_6$ show that both samples resemble the structure of bulk $\text{Cs}_2\text{NaBiCl}_6$ from literature. Hence, the purification steps do not seem to affect the crystal structure.

GIWAXS of the samples, however, revealed the preservation of the bulk $\text{Cs}_2\text{NaBiCl}_6$ phase upon NC formation and purification (Figure 6.5 c). Comparing the $\text{Cs}_2\text{NaBiCl}_6$ X-ray scattering from literature, all pronounced reflexes are observable in the GIWAXS signal of both unwashed and washed

Mn:Cs₂NaBiCl₆. Summarily, a tradeoff between optoelectronic performance and structural integrity needs to be made depending on the desired properties.

6.2 Impact of Manganese Content on Mn:Cs₂NaBiCl₆ Nanocrystals

Since the emission of Mn:Cs₂NaBiCl₆ is based on d-d transitions in manganese as a color center, the amount of Mn in the LFDP is a crucial factor for its optical properties. We varied the manganese content of the samples from 0 to 25% and analyzed the optical properties (Figure 6.6). Absorption spectra of Mn:Cs₂NaBiCl₆ exhibit a prominent excitonic peak at around 320 nm for all different Mn contents. For the undoped species, a less pronounced absorption is observed. 25% Mn shows no absorption or PL emission, except a toluene reference signal (discussed before), indicating NCs did not form. A Mn content of 25% is probably too high to allow the formation of the LFDP or at least inhibits the optoelectronic properties. For the samples from 0.10% to 15% Mn, a steady intensification of the PL emission around 595 nm is observed. At 20% Mn, the PL intensity decreases notably, indicating a non-ideal stoichiometry in the structure. By comparing the PLQY of different Mn:Cs₂NaBiCl₆ samples, similar behavior can be observed. The PLQY seems to exhibit a maximum of 2% for 10% Mn, with a subsequent drop in PLQY for higher Mn concentrations. The decrease in PLQY for higher Mn concentrations can be ascribed to either the LFDPs not being able to form properly - as indicated by the less optimal optical properties of high Mn samples - or to inadequate absorption characteristics of Mn:Cs₂NaBiCl₆. The weak PLQY for small Mn concentrations is to be expected since the observed characteristic Mn d-d transition is directly connected to the Mn amount. Thus, a manganese concentration of 10% was employed for further experiments and analyses.

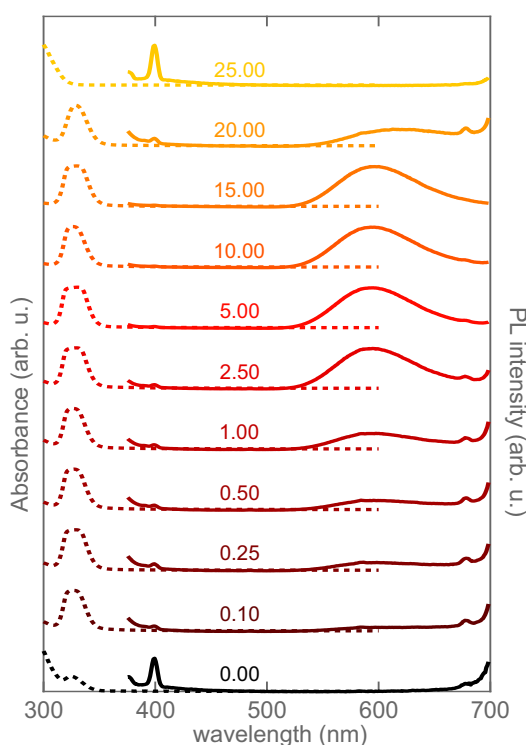


Figure 6.6: Influence of the Manganese Content in Mn:Cs₂NaBiCl₆ The amount of Mn incorporated in the synthesis was varied from 0 to 25%. From 0 to 15% Mn content, a steady increase of a PL emission peak around 595 nm is observed. For higher Mn contents this emission disappears and no optical evidence of a perovskite is found for 25% Mn.

6.3 Reaction Temperature and its Effect

As stated at the beginning of the chapter, a simpler synthesis routine is preferential. A RT-based synthesis would be optimal. While the precursor preparation requires an elevated temperature of 140 °C, it is possible to accomplish the synthesis itself at RT. The impact of the reaction temperature on the optoelectronic properties of Mn:Cs₂NaBiCl₆ NCs (10% Mn) shall be discussed in the following. Figure 6.7 displays absorption and PL spectra of LFDP NCs synthesized at RT, 55 °C, 70 °C, 100 °C and 115 °C. The overall signature of the spectra are comparable for all temperatures with a slight increase in absorption and emission intensity for increasing temperatures. This is further supported by the PLQYs of the respective samples. The PLQY shows a continuous improvement with rising reaction temperature. While the best results are obtained for moderately elevated temperatures this is a proof of concept that this synthesis routine is fully integrable in ambient atmosphere. It should be noted that, throughout the course of these experiments, the humidity of the atmosphere was not controlled and could therefore also vary throughout the experiment, further signifying the robustness of the synthesis.

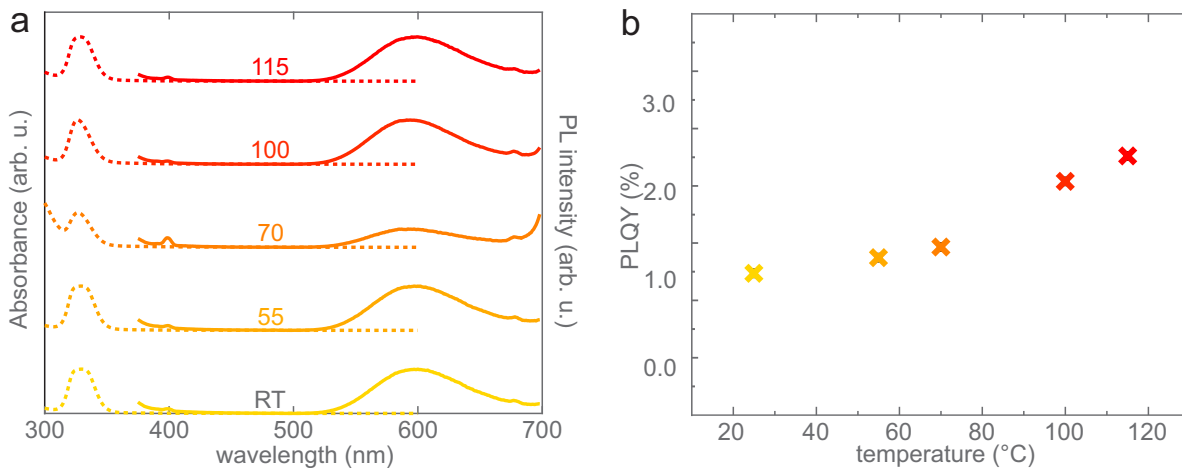


Figure 6.7: Impact of the Reaction Temperature on the Synthesis of Mn:Cs₂NaBiCl₆ NCs The reaction temperature was varied from RT to 115 °C. All samples exhibit the same optical features regarding absorption and PL, however, with increasing temperature they become more pronounced. This can be seen nicely in the PLQY rising with increasing temperature.

6.4 Longterm Stability of Mn:Cs₂NaBiCl₆ Nanocrystals

After achieving a LFDP sample with satisfying optical properties, the long-term stability of the NCs needs to be investigated. Therefore, the samples were synthesized, characterized, and stored in ambient conditions for two months, afterwards, the characterization was repeated. Figure 6.8 shows the corresponding absorption and PL spectra immediately after synthesis (dashed lines) and after storage for two months (bold lines) for Mn:Cs₂NaBiCl₆ NCs (10% Mn) following different purification steps. For the absorption spectra, no significant change is observed for different purified samples. In the PL, however, significant differences become apparent. The unwashed sample exhibits an unchanged weak emission at around 595 nm after two months, with an additional emission peak emerging between 420 nm and 428 nm. This additional peak is also present in the samples with more purification steps, albeit less pronounced. Taking into account that metal oleate species cause a similar

PL response (compare Figure 6.3), a degradation of the sample is presumably the cause. Hence, it is likely that LFDPs decompose into metal oleate species over time. The process seems to be reduced after one purification cycle and completely suppressed by two purification steps.

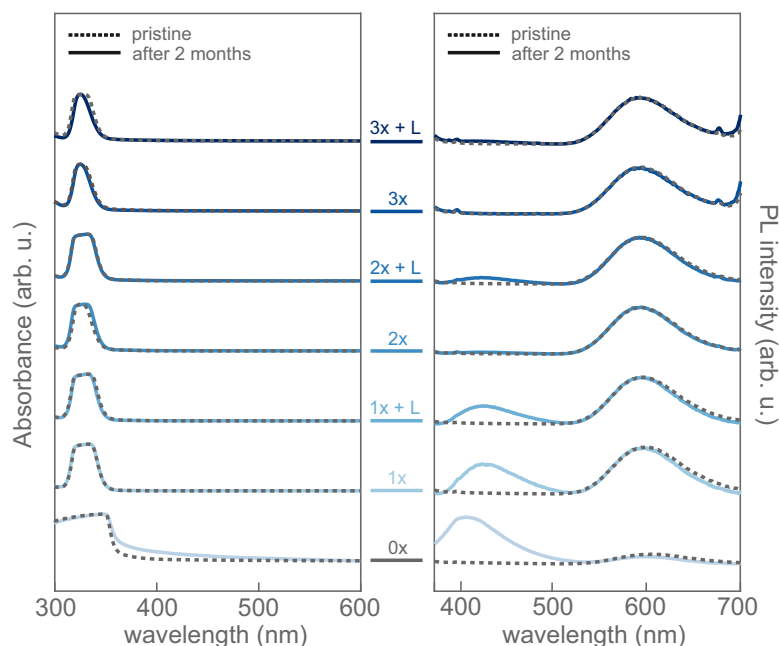


Figure 6.8: Long-Term Stability of Mn:Cs₂NaBiCl₆ Nanocrystals Absorption and PL spectra of Mn:Cs₂NaBiCl₆ NCs immediately after synthesis and after two months show a good long-term stability for NCs subjected to at least two purification steps. Especially the non-purified sample appears to degrade into various precursor species, resulting in an emerging emission peak around 420 nm.

6.5 Summary

In summary, we developed a new synthesis routine for the fabrication of manganese doped Cs₂NaBiCl₆ NCs. The process is inspired by both hot injection and LARP processes and is designed to be conducted at ambient atmosphere with moderate temperatures. After clarifying the origin of various PL signals, we found the undoped species Cs₂NaBiCl₆ to be non-emissive, likely due to the indirect bandgap. The introduction of Mn, however, introduces color centers in the structure and d-d transitions in Mn were observed with a bright orange emission around 595 nm. The effect of repeated purification of the NCs was analyzed and shown to negatively affect the morphology of the samples while enhancing the PLQY of the samples. The manganese content was tested and found to have an optimum with the highest PLQY at 10% Mn while retaining excellent optical properties. Further, the reaction temperature was scanned and it was shown that the synthesis can be conducted at room temperature. However, the PLQY is significantly increased for moderately higher reaction temperatures. Lastly, the samples were tested for their long-term stability upon storage in dispersion, and slow degradation into different precursor species was observed. However, consecutive purification of the sample after synthesis suppressed the degradation completely. Further research should be invested in optimizing the emission properties and enhancing the samples' PLQY. Only then can LFDPs compete in the market of semiconductors for optoelectronic applications.

7

Conclusion

This thesis aimed to enhance our understanding of perovskite nanocrystals and their limitations. Thereby, the focus was on the main issues hindering the commercialization of perovskite-based devices: their lack of environmental stability, their insufficient emission properties, and the toxicity of lead. Each of these aspects was tackled in a chapter of this thesis where detailed summaries of the corresponding work can be found.

Firstly, the main issue impeding perovskite nanocrystals applications is approached in [Chapter 4](#). We drastically enhance the stability of LHP NCs with the use of diblock copolymer micelle nanoreactors. The synthesis allows LHPs to grow confined within a polymer micelle where the NCs are protected from environmental-induced degradation. Micelle-encapsulated LHP NC thin films show great stability against air, moisture, and even complete submersion in water. Through selective elucidation of the effects of the polymer concentration and the diffusion time of ions, the micelle-templated synthesis could be optimized to be more time-efficient and cost-efficient in the long term. To further enhance the application possibilities of micelle-encapsulated LHPs, organic ligands are introduced in the synthesis routine to boost the PLQY to near unity and further increase their durability. The doubly stabilized LHP NCs are shown to be efficient emission downconverters. However, the huge amount of insulating organic materials impedes the direct implementation in optoelectronic devices. Hence, further research regarding conductive nanoreactors and ligands is necessary.

Secondly, the emission properties of LHP NCs are analyzed and optimized in [Chapter 5](#). Simulations of anisotropic $\text{Cs}_{n-1}\text{Pb}_n\text{Br}_{3n+1}$ NPLs in an LED revealed the beneficial emission profile of NPLs. Their anisotropic structure allows for a targeted and more efficient light outcoupling. This can be used to boost the EQE of LEDs beyond the known limits. Furthermore, a machine learning algorithm is developed to improve the emission of LHP NPLs. The precursor ratio of the synthesis can be used to quantify and predict the PL properties of the respective synthesis. The algorithm was used to improve known NPL samples and establish new thicknesses allowing to select an emission wavelength between 435 and 505 nm. Additionally, through targeted, post-synthetic halide ion exchange, the emission range of LHP-based NPLs could be extended to cover the whole visible spectrum from 400 to

610 nm. Especially red-emitting NPLs show a near-unity PLQY and, hence, should be considered as efficient red emitters in the future. While the optoelectronic properties are widely understood, little is known about how LHP NC syntheses proceed. We conducted in-situ synthesis experiments at DESY to understand the processes during the reaction. With SAXS analyses, we found, that contrary to the literature, $\text{Cs}_{n-1}\text{Pb}_n\text{Br}_{3n+1}$ NPLs are not obtained from a LARP synthesis but rather through a well-defined precursor ratio handling. The antisolvent, acetone, is merely used to induce a superstructure formation allowing the purification of the NPL samples. Furthermore, the post-synthetic enhancement treatments with bromide and iodide were observed.

Lastly, in [Chapter 6](#), a new synthesis in ambient atmosphere for lead-free double perovskites was established. Manganese doped $\text{Cs}_2\text{NaBiCl}_6$ NCs were synthesized using a process inspired by hot injection and LARP procedures. Distinct emission features were identified and used to improve the synthesis routine further. A maximal PLQY of 2.2% was obtained for samples with 10% Mn content. Furthermore, manganese doped $\text{Cs}_2\text{NaBiCl}_6$ showed great long-term stability upon storage in dispersion.

In general, it is feasible to optimize LHP NCs towards one aspect. However, to realize perovskite applications in industrial processes, they need to fulfill every requirement mentioned in the beginning of this chapter. To this points a lot of effort still needs to be dedicated to find a durable, environmentally friendly and highly efficient emitter based on halide perovskites.

References

- [1] Richard P. Feynman. “There’s Plenty of Room at the Bottom.” In: *Engineering and Science* 23.5 (1960), pp. 22–36 (cited on page 1).
- [2] Threes G Smijs and Stanislav Pavel. “Titanium dioxide and zinc oxide nanoparticles in sunscreens: focus on their safety and effectiveness.” In: *Nanotechnology, science and applications* 4 (2011), p. 95. DOI: [10.2147/NSA.S19419](https://doi.org/10.2147/NSA.S19419) (cited on page 1).
- [3] Katherine Bourzac. “Quantum dots go on display.” In: *Nature* 493.7432 (2013), p. 283. DOI: [10.1038/493283a](https://doi.org/10.1038/493283a) (cited on page 1).
- [4] Ivana Angelini, Gilberto Artioli, Paolo Bellintani, Valeria Diella, Mauro Gemmi, Angela Polla, and Antonella Rossi. “Chemical analyses of Bronze Age glasses from Frattesina di Rovigo, northern Italy.” In: *Journal of Archaeological Science* 31.8 (2004), pp. 1175–1184. DOI: [10.1016/j.jas.2004.02.015](https://doi.org/10.1016/j.jas.2004.02.015) (cited on page 1).
- [5] Federico Montanarella and Maksym V. Kovalenko. “Three Millennia of Nanocrystals.” In: *ACS Nano* (2022). DOI: [10.1021/acsnano.1c11159](https://doi.org/10.1021/acsnano.1c11159) (cited on page 1).
- [6] Gustav Rose. *De novis quibusdam fossilibus quae in montibus Uraliis inveniuntur*. typis AG Schadii, 1839 (cited on pages 1, 11).
- [7] Akihiro Kojima, Kenjiro Teshima, Yasuo Shirai, and Tsutomu Miyasaka. “Organometal halide perovskites as visible-light sensitizers for photovoltaic cells.” In: *Journal of the American Chemical Society* 131.17 (2009), pp. 6050–6051. DOI: [10.1021/ja809598r](https://doi.org/10.1021/ja809598r) (cited on page 1).
- [8] Jaeki Jeong, Minjin Kim, Jongdeuk Seo, Haizhou Lu, Paramvir Ahlawat, Aditya Mishra, Yingguo Yang, Michael A Hope, Felix T Eickemeyer, Maengsuk Kim, Yung Jin Yoon, In Woo Choi, Barbara Primera Darwich, Seung Ju Choi, Yimhyun Jo, Jun Hee Lee, Bright Walker, Shaik M. Zakeeruddin, Lyndon Emsley, Ursula Rothlisberger, Anders Hagfeldt, Dong Suk Kim, Michael Grätzel, and Jin Young Kim. “Pseudo-halide anion engineering for α -FAPbI₃ perovskite solar cells.” In: *Nature* 592.7854 (2021), pp. 381–385. DOI: [10.1038/s41586-021-03406-5](https://doi.org/10.1038/s41586-021-03406-5) (cited on pages 1, 11).
- [9] Amran Al-Ashouri, Eike Köhnen, Bor Li, Artiom Magomedov, Hannes Hempel, Pietro Caprioglio, José A Márquez, Anna Belen Morales Vilches, Ernestas Kasparavicius, Joel A. Smith, Nga Phung, Dorothee Menzel, Max Grischek, Lukas Kegelman, Dieter Skroblin, Christian Gollwitzer, Tadas Malinauskas, Marko Jost, Gasper Matic, Bernd Rech, Rutger Schlatmann, Vytautas Getautis, and Steve Albrecht. “Monolithic perovskite/silicon tandem solar cell with > 29% efficiency by enhanced hole extraction.” In: *Science* 370.6522 (2020), pp. 1300–1309. DOI: [10.1126/science.abd4016](https://doi.org/10.1126/science.abd4016) (cited on page 1).
- [10] Zhi-Kuang Tan, Reza Saberi Moghaddam, May Ling Lai, Pablo Docampo, Ruben Higler, Felix Deschler, Michael Price, Aditya Sadhanala, Luis M Pazos, Dan Credgington, Fabian Hanusch, Thomas Bein, Henry J. Snaith, and Richard H. Friend. “Bright light-emitting diodes based on organometal halide perovskite.” In: *Nature Nanotechnology* 9.9 (2014), pp. 687–692. DOI: [10.1038/nnano.2014.149](https://doi.org/10.1038/nnano.2014.149) (cited on pages 1, 11, 58).
- [11] Loredana Protesescu, Sergii Yakunin, Maryna I. Bodnarchuk, Franziska Krieg, Riccarda Caputo, Christopher H. Hendon, Ruo Xi Yang, Aron Walsh, and Maksym V. Kovalenko. “Nanocrystals of cesium lead halide perovskites (CsPbX₃, X= Cl, Br, and I): novel optoelectronic materials showing bright emission with wide color gamut.” In: *Nano Letters* 15.6 (2015), pp. 3692–3696. DOI: [10.1021/nl5048779](https://doi.org/10.1021/nl5048779) (cited on pages 1, 14, 15).
- [12] Pablo Docampo and Thomas Bein. “A long-term view on perovskite optoelectronics.” In: *Accounts of Chemical Research* 49.2 (2016), pp. 339–346. DOI: [10.1021/acs.accounts.5b00465](https://doi.org/10.1021/acs.accounts.5b00465) (cited on pages 2, 19).
- [13] Khaoula Jemli, Hiba Diab, Ferdinand Lédée, Gaele Trippé-Allard, Damien Garrot, Bernard Geffroy, Jean-Sébastien Lauret, Pierre Audebert, and Emmanuelle Deleporte. “Using low temperature photoluminescence spectroscopy to investigate CH₃NH₃PbI₃ hybrid perovskite degradation.” In: *Molecules* 21.7 (2016), p. 885. DOI: [10.3390/molecules21070885](https://doi.org/10.3390/molecules21070885) (cited on pages 2, 19).
- [14] Joop Schoonman. “Organic–inorganic lead halide perovskite solar cell materials: a possible stability problem.” In: *Chemical Physics Letters* 619 (2015), pp. 193–195. DOI: [10.1016/j.cplett.2014.11.063](https://doi.org/10.1016/j.cplett.2014.11.063) (cited on pages 2, 19).
- [15] Giorgio Schileo and Giulia Grancini. “Lead or no lead? Availability, toxicity, sustainability and environmental impact of lead-free perovskite solar cells.” In: *Journal of Materials Chemistry C* 9.1 (2021), pp. 67–76. DOI: [10.1039/D0TC04552G](https://doi.org/10.1039/D0TC04552G) (cited on pages 2, 20).
- [16] Junming Li, Hai-Lei Cao, Wen-Bin Jiao, Qiong Wang, Mingdeng Wei, Irene Cantone, Jian Lü, and Antonio Abate. “Biological impact of lead from halide perovskites reveals the risk of introducing a safe threshold.” In: *Nature Communications* 11.1 (2020), pp. 1–5. DOI: [10.1038/s41467-019-13910-y](https://doi.org/10.1038/s41467-019-13910-y) (cited on pages 2, 20).
- [17] Peter Y. Yu and Manuel Cardona. *Fundamentals of Semiconductors: Physics and Materials Properties*. Springer, 2010. DOI: [10.1007/978-3-642-00710-1](https://doi.org/10.1007/978-3-642-00710-1) (cited on pages 4, 5).

- [18] Neil W. Ashcroft and N. David Mermin. *Solid State Physics*. Saunders College Publishing, 1976. DOI: [10.1002/piuz.19780090109](https://doi.org/10.1002/piuz.19780090109) (cited on page 4).
- [19] Charles Kittel. *Introduction to Solid State Physics*. Vol. 8. Wiley New York, 2004. DOI: [10.1119/1.1974177](https://doi.org/10.1119/1.1974177) (cited on pages 4, 30).
- [20] Rudolf Gross, Achim Marx, Dietrich Einzel, and Stephan Geprägs. *Festkörperphysik*. de Gruyter, 2018 (cited on pages 4, 29, 30).
- [21] Wahyu Setyawan and Stefano Curtarolo. “High-throughput electronic band structure calculations: Challenges and tools.” In: *Computational Materials Science* 49.2 (2010), pp. 299–312. DOI: [10.1016/j.commatsci.2010.05.010](https://doi.org/10.1016/j.commatsci.2010.05.010) (cited on page 5).
- [22] Mark Fox. *Optical Properties of Solids*. Oxford University Press, 2002. DOI: [10.1119/1.1691372](https://doi.org/10.1119/1.1691372) (cited on pages 5, 6, 9).
- [23] Jasprit Singh. *Electronic and Optoelectronic Properties of Semiconductor Structures*. Cambridge University Press, 2003. DOI: [10.1017/CBO9780511805745](https://doi.org/10.1017/CBO9780511805745) (cited on page 8).
- [24] Werner Heisenberg. “Über den anschaulichen Inhalt der quantentheoretischen Kinematik und Mechanik.” In: *Zeitschrift für Physik* 43.3 (1927), pp. 172–198. DOI: [10.1007/BF01397280](https://doi.org/10.1007/BF01397280) (cited on page 8).
- [25] Woldemar Voigt. “Über das Gesetz der Intensitätsverteilung innerhalb der Linien eines Gasspektrums.” In: *Sitzungsberichte der K. B. Akad. d. Wiss.* 1912,25 (1912) (cited on page 9).
- [26] S. Rudin, T. L. Reinecke, and B. Segall. “Temperature-dependent exciton linewidths in semiconductors.” In: *Physical Review B* 42.17 (1990), pp. 11218–11231. DOI: [10.1103/PhysRevB.42.11218](https://doi.org/10.1103/PhysRevB.42.11218) (cited on page 9).
- [27] Shizuo Miyake and Ryuzo Ueda. “On polymorphic change of BaTiO₃.” In: *Journal of the Physical Society of Japan* 1.1 (1932), pp. 32–33. DOI: [10.1143/JPSJ.1.32](https://doi.org/10.1143/JPSJ.1.32) (cited on page 11).
- [28] L. E. Cross and R. E. Newnham. “History of ferroelectrics.” In: *Ceramics and Civilization* 3 (1987), pp. 289–305 (cited on page 11).
- [29] H. L. Wells and W. R. Johnston. “Über die Ammoniumbleihalogenide.” In: *Zeitschrift für anorganische Chemie* 4.1-2 (1893), pp. 117–127. DOI: [10.1002/zaac.18930030124](https://doi.org/10.1002/zaac.18930030124) (cited on page 11).
- [30] Dieter Weber. “CH₃NH₃PbX₃, ein Pb(II)-System mit kubischer Perowskitstruktur/ CH₃NH₃PbX₃, a Pb(II)-system with cubic perovskite structure.” In: *Zeitschrift für Naturforschung B* 33.12 (1978), pp. 1443–1445. DOI: [10.1515/ZNB-1978-1214](https://doi.org/10.1515/ZNB-1978-1214) (cited on page 11).
- [31] Tao Fang, Tiantian Wang, Xiansheng Li, Yuhui Dong, Sai Bai, and Jizhong Song. “Perovskite QLED with an external quantum efficiency of over 21% by modulating electronic transport.” In: *Science Bulletin* 66.1 (2021), pp. 36–43. DOI: [10.1016/j.scib.2020.08.025](https://doi.org/10.1016/j.scib.2020.08.025) (cited on pages 11, 58).
- [32] Victor M. Goldschmidt. “Die Gesetze der Krystallochemie.” In: *Naturwissenschaften* 14.21 (1926), pp. 477–485. DOI: [10.1007/BF01507527](https://doi.org/10.1007/BF01507527) (cited on page 11).
- [33] W. Travis, E. N. K. Glover, Hugo Bronstein, D. O. Scanlon, and R. G. Palgrave. “On the application of the tolerance factor to inorganic and hybrid halide perovskites: a revised system.” In: *Chemical Science* 7.7 (2016), pp. 4548–4556. DOI: [10.1039/C5SC04845A](https://doi.org/10.1039/C5SC04845A) (cited on page 12).
- [34] Joseph S. Manser, Jeffrey A. Christians, and Prashant V. Kamat. “Intriguing optoelectronic properties of metal halide perovskites.” In: *Chemical Reviews* 116.21 (2016), pp. 12956–13008. DOI: [10.1021/acs.chemrev.6b00136](https://doi.org/10.1021/acs.chemrev.6b00136) (cited on page 12).
- [35] David B. Mitzi, Christos D. Dimitrakopoulos, and Laura L. Kosbar. “Structurally tailored organic- inorganic perovskites: optical properties and solution-processed channel materials for thin-film transistors.” In: *Chemistry of Materials* 13.10 (2001), pp. 3728–3740. DOI: [10.1021/cm010105g](https://doi.org/10.1021/cm010105g) (cited on page 12).
- [36] Gregor Kieslich, Shijing Sun, and Anthony .K Cheetham. “An extended tolerance factor approach for organic-inorganic perovskites.” In: *Chemical Science* 6.6 (2015), pp. 3430–3433. DOI: [10.1039/C5SC00961H](https://doi.org/10.1039/C5SC00961H) (cited on page 12).
- [37] Shunsuke Hirotsu, Jimpei Harada, Masashi Iizumi, and Kazuo Gesi. “Structural phase transitions in CsPbBr₃.” In: *Journal of the Physical Society of Japan* 37.5 (1974), pp. 1393–1398. DOI: [10.1143/JPSJ.37.1393](https://doi.org/10.1143/JPSJ.37.1393) (cited on page 12).
- [38] Noriko Onoda-Yamamuro, Takasuke Matsuo, and Hiroshi Suga. “Calorimetric and IR spectroscopic studies of phase transitions in methylammonium trihalogenoplumbates (II).” In: *Journal of Physics and Chemistry of Solids* 51.12 (1990), pp. 1383–1395. DOI: [10.1016/0022-3697\(90\)90021-7](https://doi.org/10.1016/0022-3697(90)90021-7) (cited on page 12).
- [39] Bertrand Philippe, T Jesper Jacobsson, Juan-Pablo Correa-Baena, Naresh K Jena, Amitava Banerjee, Sudip Chakraborty, Ute B Cappel, Rajeev Ahuja, Anders Hagfeldt, Michael Odelius, and Hakan Rensmo. “Valence level character in a mixed perovskite material and determination of the valence band maximum from photoelectron spectroscopy: variation with photon energy.” In: *The Journal of Physical Chemistry C* 121.48 (2017), pp. 26655–26666. DOI: [10.1021/acs.jpcc.7b08948](https://doi.org/10.1021/acs.jpcc.7b08948) (cited on page 13).
- [40] Masaki Shirayama, Hideyuki Kadowaki, Tetsuhiko Miyadera, Takeshi Sugita, Masato Tamakoshi, Masato Kato, Takemasa Fujiseki, Daisuke Murata, Shota Hara, Takuro N. Murakami, Shohei Fujimoto, Masayuki Chikamatsu, and Hiroyuki Fujiwara. “Optical Transitions in Hybrid Perovskite Solar Cells: Ellipsometry, Density Functional Theory, and Quantum Efficiency Analyses for CH₃NH₃PbI₃.” In: *Physical Review Applied* 5 (1 2016), p. 014012. DOI: [10.1103/PhysRevApplied.5.014012](https://doi.org/10.1103/PhysRevApplied.5.014012) (cited on page 13).

- [41] Mujtaba Hussain, Muhammad Rashid, Faisal Saeed, and AS Bhatti. "Spin-orbit coupling effect on energy level splitting and band structure inversion in CsPbBr₃." In: *Journal of Materials Science* 56.1 (2021), pp. 528–542. doi: [10.1007/s10853-020-05298-8](https://doi.org/10.1007/s10853-020-05298-8) (cited on page 13).
- [42] Yu-Yun Pan, Yen-Hsun Su, Chuang-Han Hsu, Li-Wen Huang, and Chao-Cheng Kaun. "The electronic structure of organic-inorganic hybrid perovskite solar cell: a first-principles analysis." In: *Computational Materials Science* 117 (2016), pp. 573–578. doi: [10.1016/j.commatsci.2015.12.015](https://doi.org/10.1016/j.commatsci.2015.12.015) (cited on page 13).
- [43] Nobuaki Kitazawa, Y. Watanabe, and Y. Nakamura. "Optical properties of CH₃NH₃PbX₃ (X= halogen) and their mixed-halide crystals." In: *Journal of Materials Science* 37.17 (2002), pp. 3585–3587. doi: [10.1023/A:1016584519829](https://doi.org/10.1023/A:1016584519829) (cited on page 13).
- [44] Laura M. Herz. "Charge-carrier dynamics in organic-inorganic metal halide perovskites." In: *Annual Review of Physical Chemistry* 67.1 (2016), pp. 65–89. doi: [10.1146/annurev-physchem-040215-112222](https://doi.org/10.1146/annurev-physchem-040215-112222) (cited on pages 13, 14).
- [45] Jun Kang and Lin-Wang Wang. "High Defect Tolerance in Lead Halide Perovskite CsPbBr₃." In: *The Journal of Physical Chemistry Letters* 8.2 (2017), pp. 489–493. doi: [10.1021/acs.jpcllett.6b02800](https://doi.org/10.1021/acs.jpcllett.6b02800) (cited on page 14).
- [46] Junzhi Ye, Mahdi Malekshahi Byranvand, Clara Otero Martínez, Robert L.Z. Hoye, Michael Saliba, and Lakshminarayana Polavarapu. "Defect Passivation in Lead-Halide Perovskite Nanocrystals and Thin Films: Toward Efficient LEDs and Solar cells." In: *Angewandte Chemie* 60.40 (2021), pp. 21636–21660. doi: [10.1002/anie.202102360](https://doi.org/10.1002/anie.202102360) (cited on page 14).
- [47] He Huang, Maryna I. Bodnarchuk, Stephen V. Kershaw, Maksym V. Kovalenko, and Andrey L. Rogach. "Lead halide perovskite nanocrystals in the research spotlight: stability and defect tolerance." In: *ACS Energy Letters* 2.9 (2017), pp. 2071–2083. doi: [10.1021/acsenergylett.7b00547](https://doi.org/10.1021/acsenergylett.7b00547) (cited on page 14).
- [48] R. Rossetti, S. Nakahara, and Louis E. Brus. "Quantum size effects in the redox potentials, resonance Raman spectra, and electronic spectra of CdS crystallites in aqueous solution." In: *The Journal of Chemical Physics* 79.2 (1983), pp. 1086–1088. doi: [10.1063/1.445834](https://doi.org/10.1063/1.445834) (cited on page 14).
- [49] Louis Brus. "Electronic wave functions in semiconductor clusters: experiment and theory." In: *The Journal of Physical Chemistry* 90.12 (1986), pp. 2555–2560 (cited on page 14).
- [50] Jeong-Hyeok Im, Chang-Ryul Lee, Jin-Wook Lee, Sang-Won Park, and Nam-Gyu Park. "6.5% efficient perovskite quantum-dot-sensitized solar cell." In: *Nanoscale* 3.10 (2011), pp. 4088–4093. doi: [10.1039/C1NR10867K](https://doi.org/10.1039/C1NR10867K) (cited on page 14).
- [51] Luciana C Schmidt, Antonio Pertegás, Soranyel González-Carrero, Olga Malinkiewicz, Said Agouram, Guillermo Minguez Espallargas, Henk J. Bolink, Raquel E. Galian, and Julia Pérez-Prieto. "Nontemplate synthesis of CH₃NH₃PbBr₃ perovskite nanoparticles." In: *Journal of the American Chemical Society* 136.3 (2014), pp. 850–853. doi: [10.1021/ja4109209](https://doi.org/10.1021/ja4109209) (cited on page 14).
- [52] Yu Tong, Eva Bladt, Meltem F. Aygüler, Aurora Manzi, Karolina Z. Milowska, Verena A. Hintermayr, Pablo Docampo, Sara Bals, Alexander S. Urban, Lakshminarayana Polavarapu, and Jochen Feldmann. "Highly luminescent cesium lead halide perovskite nanocrystals with tunable composition and thickness by ultrasonication." In: *Angewandte Chemie* 55.44 (2016), pp. 13887–13892. doi: [10.1002/anie.201605909](https://doi.org/10.1002/anie.201605909) (cited on pages 14, 15).
- [53] Yehonadav Bekenstein, Brent A. Koscher, Samuel W. Eaton, Peidong Yang, and A. Paul Alivisatos. "Highly luminescent colloidal nanoplates of perovskite cesium lead halide and their oriented assemblies." In: *Journal of the American Chemical Society* 137.51 (2015), pp. 16008–16011. doi: [10.1021/jacs.5b11199](https://doi.org/10.1021/jacs.5b11199) (cited on page 14).
- [54] Dandan Zhang, Samuel W Eaton, Yi Yu, Letian Dou, and Peidong Yang. "Solution-phase synthesis of cesium lead halide perovskite nanowires." In: *Journal of the American Chemical Society* 137.29 (2015), pp. 9230–9233. doi: [10.1021/jacs.5b05404](https://doi.org/10.1021/jacs.5b05404) (cited on page 14).
- [55] Yu Tong, Bernhard J. Bohn, Eva Bladt, Kun Wang, Peter Müller-Buschbaum, Sara Bals, Alexander S. Urban, Lakshminarayana Polavarapu, and Jochen Feldmann. "From precursor powders to CsPbX₃ perovskite nanowires: One-pot synthesis, growth mechanism, and oriented self-assembly." In: *Angewandte Chemie* 56.44 (2017), pp. 13887–13892. doi: [10.1002/anie.201707224](https://doi.org/10.1002/anie.201707224) (cited on page 14).
- [56] Theobald Lohmüller, Daniel Aydin, Marco Schwieder, Christoph Morhard, Ilia Louban, Claudia Pacholski, and Joachim P. Spatz. "Nanopatterning by block copolymer micelle nanolithography and bioinspired applications." In: *Biointerphases* 6.1 (2011), MR1–MR12. doi: [10.1116/1.3536839](https://doi.org/10.1116/1.3536839) (cited on pages 15, 20, 21, 38, 39).
- [57] Javad Shamsi, Alexander S. Urban, Muhammad Imran, Luca De Trizio, and Liberato Manna. "Metal halide perovskite nanocrystals: synthesis, post-synthesis modifications, and their optical properties." In: *Chemical Reviews* 119.5 (2019), pp. 3296–3348. doi: [10.1021/acs.chemrev.8b00644](https://doi.org/10.1021/acs.chemrev.8b00644) (cited on page 15).
- [58] C. Bea Murray, David J. Norris, and Mounqi G. Bawendi. "Synthesis and characterization of nearly monodisperse CdE (E= sulfur, selenium, tellurium) semiconductor nanocrystallites." In: *Journal of the American Chemical Society* 115.19 (1993), pp. 8706–8715 (cited on page 15).
- [59] Craig R Bullen and Paul Mulvaney. "Nucleation and growth kinetics of CdSe nanocrystals in octadecene." In: *Nano Letters* 4.12 (2004), pp. 2303–2307. doi: [10.1021/nl0496724](https://doi.org/10.1021/nl0496724) (cited on page 15).

- [60] Oleh Vybornyi, Sergii Yakunin, and Maksym V. Kovalenko. "Polar-solvent-free colloidal synthesis of highly luminescent alkylammonium lead halide perovskite nanocrystals." In: *Nanoscale* 8.12 (2016), pp. 6278–6283. doi: [10.1039/C5NR06890H](https://doi.org/10.1039/C5NR06890H) (cited on page 15).
- [61] Qi Pan, Huicheng Hu, Yatao Zou, Min Chen, Linzhong Wu, Di Yang, Xiaolei Yuan, Jian Fan, Baoquan Sun, and Qiao Zhang. "Microwave-assisted synthesis of high-quality "all-inorganic" CsPbX₃ (X= Cl, Br, I) perovskite nanocrystals and their application in light emitting diodes." In: *Journal of Materials Chemistry C* 5.42 (2017), pp. 10947–10954. doi: [10.1039/C7TC03774K](https://doi.org/10.1039/C7TC03774K) (cited on page 15).
- [62] Mark Kurlansky and SD Schindler. *The story of salt*. GP Putnam's Sons, 2006 (cited on page 15).
- [63] Hitoshi Kasai, Hari Singh Nalwa, Hidetoshi Oikawa, Shuji Okada, Hiro Matsuda, Nobutsugu Minami, Atsushi Kakuta, Katsumichi Ono, Akio Mukoh, and Hachiro Nakanishi. "A novel preparation method of organic microcrystals." In: *Japanese Journal of Applied Physics* 31.8A (1992), p. L1132 (cited on page 16).
- [64] Yong Sheng Zhao, Hongbing Fu, Aidong Peng, Ying Ma, Debao Xiao, and Jiannian Yao. "Low-dimensional nanomaterials based on small organic molecules: preparation and optoelectronic properties." In: *Advanced Materials* 20.15 (2008), pp. 2859–2876. doi: [10.1002/adma.200800604](https://doi.org/10.1002/adma.200800604) (cited on page 16).
- [65] Ioannis Lignos, Stavros Stavrakis, Georgian Nedelcu, Loredana Protesescu, Andrew J. deMello, and Maksym V. Kovalenko. "Synthesis of cesium lead halide perovskite nanocrystals in a droplet-based microfluidic platform: fast parametric space mapping." In: *Nano Letters* 16.3 (2016), pp. 1869–1877. doi: [10.1021/acs.nanolett.5b04981](https://doi.org/10.1021/acs.nanolett.5b04981) (cited on page 16).
- [66] Jasmina A. Sichert, Yu Tong, Niklas Mutz, Mathias Vollmer, Stefan Fischer, Karolina Z. Milowska, Ramon García Cortadella, Bert Nickel, Carlos Cardenas-Daw, Jacek K. Stolarczyk, Alexander S. Urban, and Jochen Feldmann. "Quantum size effect in organometal halide perovskite nanoplatelets." In: *Nano Letters* 15.10 (2015), pp. 6521–6527. doi: [10.1021/acs.nanolett.5b02985](https://doi.org/10.1021/acs.nanolett.5b02985) (cited on pages 16, 63).
- [67] Sudhir Kumar, Jakub Jagielski, Sergii Yakunin, Peter Rice, Yu-Cheng Chiu, Mingchao Wang, Georgian Nedelcu, Yeongin Kim, Shangchao Lin, Elton J. G. Santos, Maksym V. Kovalenko, and Chih-Jen Shih. "Efficient blue electroluminescence using quantum-confined two-dimensional perovskites." In: *ACS Nano* 10.10 (2016), pp. 9720–9729. doi: [10.1021/acs.nano.6b05775](https://doi.org/10.1021/acs.nano.6b05775) (cited on page 16).
- [68] Feng Zhang, Sheng Huang, Peng Wang, Xiaomei Chen, Suling Zhao, Yuping Dong, and Haizheng Zhong. "Colloidal synthesis of air-stable CH₃NH₃PbI₃ quantum dots by gaining chemical insight into the solvent effects." In: *Chemistry of Materials* 29.8 (2017), pp. 3793–3799. doi: [10.1021/acs.chemmater.7b01100](https://doi.org/10.1021/acs.chemmater.7b01100) (cited on page 16).
- [69] Javad Shamsi, Prachi Rastogi, Vincenzo Caligiuri, Ahmed L Abdelhady, Davide Spirito, Liberato Manna, and Roman Krahne. "Bright-emitting perovskite films by large-scale synthesis and photoinduced solid-state transformation of CsPbBr₃ nanoplatelets." In: *ACS Nano* 11.10 (2017), pp. 10206–10213. doi: [10.1021/acs.nano.7b04761](https://doi.org/10.1021/acs.nano.7b04761) (cited on page 16).
- [70] Song Wei, Yanchun Yang, Xiaojiao Kang, Lan Wang, Lijian Huang, and Daocheng Pan. "Room-temperature and gram-scale synthesis of CsPbX₃ (X= Cl, Br, I) perovskite nanocrystals with 50–85% photoluminescence quantum yields." In: *Chemical Communications* 52.45 (2016), pp. 7265–7268. doi: [10.1039/C6CC01500J](https://doi.org/10.1039/C6CC01500J) (cited on page 16).
- [71] Bernhard J. Bohn, Yu Tong, Moritz Gramlich, May Ling Lai, Markus Döblinger, Kun Wang, Robert L. Z. Hoye, Peter Müller-Buschbaum, Samuel D. Stranks, Alexander S. Urban, Lakshminarayana Polavarapu, and Jochen Feldmann. "Boosting tunable blue luminescence of halide perovskite nanoplatelets through postsynthetic surface trap repair." In: *Nano Letters* 18.8 (2018), pp. 5231–5238. doi: [10.1021/acs.nanolett.8b02190](https://doi.org/10.1021/acs.nanolett.8b02190) (cited on pages 16–18, 27, 28, 61–63, 65, 66).
- [72] Guilherme Almeida, Luca Goldoni, Quinten Akkerman, Zhiya Dang, Ali Hossain Khan, Sergio Marras, Iwan Moreels, and Liberato Manna. "Role of acid–base equilibria in the size, shape, and phase control of cesium lead bromide nanocrystals." In: *ACS Nano* 12.2 (2018), pp. 1704–1711. doi: [10.1021/acs.nano.7b08357](https://doi.org/10.1021/acs.nano.7b08357) (cited on page 17).
- [73] Victor M. Burlakov, Yasser Hassan, Mohsen Danaie, Henry J. Snaith, and Alain Goriely. "Competitive nucleation mechanism for CsPbBr₃ perovskite nanoplatelet growth." In: *The Journal of Physical Chemistry Letters* 11.16 (2020), pp. 6535–6543. doi: [10.1021/acs.jpcclett.0c01794](https://doi.org/10.1021/acs.jpcclett.0c01794) (cited on page 17).
- [74] Elisabetta Fanizza, Francesca Cascella, Davide Altamura, Cinzia Giannini, Annamaria Panniello, Leonardo Triggiani, Francesca Panzarea, Nicoletta Depalo, Roberto Grisorio, Gian Paolo Suranna, Angela Agostiano, M. Lucia Curri, and Marinella Striccoli. "Post-synthesis phase and shape evolution of CsPbBr₃ colloidal nanocrystals: The role of ligands." In: *Nano Research* 12.5 (2019), pp. 1155–1166. doi: [10.1007/s12274-019-2371-2](https://doi.org/10.1007/s12274-019-2371-2) (cited on page 17).
- [75] Jizhong Song, Leimeng Xu, Jianhai Li, Jie Xue, Yuhui Dong, Xiaoming Li, and Haibo Zeng. "Monolayer and few-layer all-inorganic perovskites as a new family of two-dimensional semiconductors for printable optoelectronic devices." In: *Advanced Materials* 28.24 (2016), pp. 4861–4869. doi: [10.1002/adma.201600225](https://doi.org/10.1002/adma.201600225) (cited on page 17).
- [76] Javad Shamsi, Zhiya Dang, Paolo Bianchini, Claudio Canale, Francesco Di Stasio, Rosaria Brescia, Mirko Prato, and Liberato Manna. "Colloidal synthesis of quantum confined single crystal CsPbBr₃ nanosheets with lateral size control up to the micrometer range." In: *Journal of the American Chemical Society* 138.23 (2016), pp. 7240–7243. doi: [10.1021/jacs.6b03166](https://doi.org/10.1021/jacs.6b03166) (cited on page 17).

- [77] Jonathan De Roo, Maria Ibáñez, Pieter Geiregat, Georgian Nedelcu, Willem Walravens, Jorick Maes, Jose C. Martins, Isabel Van Driessche, Maksym V Kovalenko, and Zeger Hens. “Highly dynamic ligand binding and light absorption coefficient of cesium lead bromide perovskite nanocrystals.” In: *ACS Nano* 10.2 (2016), pp. 2071–2081. doi: [10.1021/acsnano.5b06295](https://doi.org/10.1021/acsnano.5b06295) (cited on pages 17–19).
- [78] Franziska Krieg, Stefan T. Ochsenein, Sergii Yakunin, Stephanie Ten Brinck, Philipp Aellen, Adrian Süess, Baptiste Clerc, Dominic Guggisberg, Olga Nazarenko, Yevhen Shynkarenko, Sudhir Kumar, Chih-Jen Shih, Ivan Infante, and Maksym V. Kovalenko. “Colloidal CsPbX₃ (X= Cl, Br, I) nanocrystals 2.0: Zwitterionic capping ligands for improved durability and stability.” In: *ACS Energy Letters* 3.3 (2018), pp. 641–646. doi: [10.1021/acseenergylett.8b00035](https://doi.org/10.1021/acseenergylett.8b00035) (cited on pages 18, 19).
- [79] Maryna I Bodnarchuk, Simon C Boehme, Stephanie Ten Brinck, Caterina Bernasconi, Yevhen Shynkarenko, Franziska Krieg, Roland Widmer, Beat Aeschlimann, Detlef Günther, Maksym V Kovalenko, and Ivan Infante. “Rationalizing and controlling the surface structure and electronic passivation of cesium lead halide nanocrystals.” In: *ACS Energy Letters* 4.1 (2018), pp. 63–74. doi: [10.1021/acseenergylett.8b01669](https://doi.org/10.1021/acseenergylett.8b01669) (cited on pages 18, 19).
- [80] Andriy Stelmakh, Marcel Aebli, Andrij Baumketner, and Maksym V. Kovalenko. “On the mechanism of alkylammonium ligands binding to the surface of CsPbBr₃ nanocrystals.” In: *Chemistry of Materials* 33.15 (2021), pp. 5962–5973. doi: [10.1021/acs.chemmater.1c01081](https://doi.org/10.1021/acs.chemmater.1c01081) (cited on page 18).
- [81] Francesco Di Stasio, Sotirios Christodoulou, Nengjie Huo, and Gerasimos Konstantatos. “Near-unity photoluminescence quantum yield in CsPbBr₃ nanocrystal solid-state films via postsynthesis treatment with lead bromide.” In: *Chemistry of Materials* 29.18 (2017), pp. 7663–7667. doi: [10.1021/acs.chemmater.7b02834](https://doi.org/10.1021/acs.chemmater.7b02834) (cited on page 18).
- [82] Junichiro Mizusaki, Kimiyasu Arai, and Kazuo Fueki. “Ionic conduction of the perovskite-type halides.” In: *Solid State Ionics* 11.3 (1983), pp. 203–211. doi: [10.1016/0167-2738\(83\)90025-5](https://doi.org/10.1016/0167-2738(83)90025-5) (cited on page 19).
- [83] Christopher Eames, Jarvist M. Frost, Piers R. F. Barnes, Brian C. O’regan, Aron Walsh, and M. Saiful Islam. “Ionic transport in hybrid lead iodide perovskite solar cells.” In: *Nature Communications* 6.1 (2015), pp. 1–8. doi: [10.1038/ncomms8497](https://doi.org/10.1038/ncomms8497) (cited on page 19).
- [84] Edoardo Mosconi and Filippo De Angelis. “Mobile ions in organohalide perovskites: interplay of electronic structure and dynamics.” In: *ACS Energy Letters* 1.1 (2016), pp. 182–188. doi: [10.1021/acseenergylett.6b00108](https://doi.org/10.1021/acseenergylett.6b00108) (cited on page 19).
- [85] Maksym V. Kovalenko, Loredana Protesescu, and Maryna I. Bodnarchuk. “Properties and potential optoelectronic applications of lead halide perovskite nanocrystals.” In: *Science* 358.6364 (2017), pp. 745–750. doi: [10.1126/science.aam7093](https://doi.org/10.1126/science.aam7093) (cited on page 19).
- [86] Cun-Zheng Ning, Letian Dou, and Peidong Yang. “Bandgap engineering in semiconductor alloy nanomaterials with widely tunable compositions.” In: *Nature Reviews Materials* 2.12 (2017), pp. 1–14. doi: [10.1038/natrevmats.2017.70](https://doi.org/10.1038/natrevmats.2017.70) (cited on page 19).
- [87] Chris Guhrenz, Albrecht Benad, Christoph Ziegler, Danny Haubold, Nikolai Gaponik, and Alexander Eychmüller. “Solid-state anion exchange reactions for color tuning of CsPbX₃ perovskite nanocrystals.” In: *Chemistry of Materials* 28.24 (2016), pp. 9033–9040. doi: [10.1021/acs.chemmater.6b03980](https://doi.org/10.1021/acs.chemmater.6b03980) (cited on page 19).
- [88] Yongping Fu, Haiming Zhu, Constantinos C Stoumpos, Qi Ding, Jue Wang, Mercouri G Kanatzidis, Xiaoyang Zhu, and Song Jin. “Broad wavelength tunable robust lasing from single-crystal nanowires of cesium lead halide perovskites (CsPbX₃, X= Cl, Br, I).” In: *ACS Nano* 10.8 (2016), pp. 7963–7972. doi: [10.1021/acsnano.6b03916](https://doi.org/10.1021/acsnano.6b03916) (cited on page 19).
- [89] Jarvist M Frost, Keith T Butler, Federico Brivio, Christopher H Hendon, Mark Van Schilfgaarde, and Aron Walsh. “Atomistic origins of high-performance in hybrid halide perovskite solar cells.” In: *Nano Letters* 14.5 (2014), pp. 2584–2590. doi: [10.1021/nl500390f](https://doi.org/10.1021/nl500390f) (cited on page 19).
- [90] Shouqiang Huang, Zhichun Li, Bo Wang, Nanwen Zhu, Congyang Zhang, Long Kong, Qi Zhang, Aidang Shan, and Liang Li. “Morphology evolution and degradation of CsPbBr₃ nanocrystals under blue light-emitting diode illumination.” In: *ACS Applied Materials & Interfaces* 9.8 (2017), pp. 7249–7258. doi: [10.1021/acsam.6b14423](https://doi.org/10.1021/acsam.6b14423) (cited on page 19).
- [91] Anna Loidice, Seryio Saris, Emad Oveisi, Duncan T. L. Alexander, and Raffaella Buonsanti. “CsPbBr₃ QD/AlO_x inorganic nanocomposites with exceptional stability in water, light, and heat.” In: *Angewandte Chemie International Edition* 56.36 (2017), pp. 10696–10701. doi: [10.1002/anie.201703703](https://doi.org/10.1002/anie.201703703) (cited on page 20).
- [92] Ashraf Uddin, Mushfika Baishakhi Upama, Haimang Yi, and Leipeng Duan. “Encapsulation of organic and perovskite solar cells: A review.” In: *Coatings* 9.2 (2019), p. 65. doi: [10.3390/coatings9020065](https://doi.org/10.3390/coatings9020065) (cited on page 20).
- [93] M. Bidikoudi, E. Fresta, and R. D. Costa. “White perovskite based lighting devices.” In: *Chemical Communications* 54.59 (2018), pp. 8150–8169. doi: [10.1039/C8CC03166E](https://doi.org/10.1039/C8CC03166E) (cited on page 20).
- [94] Weilin Zheng, Zhichun Li, Congyang Zhang, Bo Wang, Qinggang Zhang, Qun Wan, Long Kong, and Liang Li. “Stabilizing perovskite nanocrystals by controlling protective surface ligands density.” In: *Nano Research* 12.6 (2019), pp. 1461–1465. doi: [10.1007/s12274-019-2407-7](https://doi.org/10.1007/s12274-019-2407-7) (cited on page 20).
- [95] Da Eun Lee, Soo Young Kim, and Ho Won Jang. “Lead-free all-inorganic halide perovskite quantum dots: review and outlook.” In: *Journal of the Korean Ceramic Society* 57.5 (2020), pp. 455–479. doi: [10.1007/s43207-020-00058-5](https://doi.org/10.1007/s43207-020-00058-5) (cited on pages 20, 22).

- [96] Michael Szwarc, M. Levy, and R. Milkovich. "Polymerization initiated by electron transfer to monomer. A new method of formation of block polymers." In: *Journal of the American Chemical Society* 78.11 (1956), pp. 2656–2657 (cited on page 20).
- [97] A. Hirao and S. Nakahama. "Anionic living polymerization of functionalized monomers." In: *Acta Polymerica* 49.4 (1998), pp. 133–144. doi: [10.1002/\(SICI\)1521-4044\(199804\)49:4<133::AID-APOL133>3.0.CO;2-P](https://doi.org/10.1002/(SICI)1521-4044(199804)49:4<133::AID-APOL133>3.0.CO;2-P) (cited on page 20).
- [98] Jean-François Gohy. "Block copolymer micelles." In: *Block copolymers II*. Springer, 2005, pp. 65–136 (cited on page 20).
- [99] F. M. Merret. "The Separation and Characterization of Graft Copolymers from Natural Rubber." In: *Rubber Chemistry and Technology* 31.4 (1958), pp. 819–828. doi: [10.5254/1.3542343](https://doi.org/10.5254/1.3542343) (cited on page 20).
- [100] Gerard Riess. "Micellization of block copolymers." In: *Progress in Polymer Science* 28.7 (2003), pp. 1107–1170. doi: [10.1016/S0079-6700\(03\)00015-7](https://doi.org/10.1016/S0079-6700(03)00015-7) (cited on page 20).
- [101] R. Nagarajan and K. Ganesh. "Block copolymer self-assembly in selective solvents: Spherical micelles with segregated cores." In: *The Journal of chemical physics* 90.10 (1989), pp. 5843–5856. doi: [10.1063/1.456390](https://doi.org/10.1063/1.456390) (cited on page 20).
- [102] Stephan Förster, Mathias Zisenis, Eckhard Wenz, and Markus Antonietti. "Micellization of strongly segregated block copolymers." In: *The Journal of Chemical Physics* 104.24 (1996), pp. 9956–9970. doi: [10.1063/1.471723](https://doi.org/10.1063/1.471723) (cited on page 20).
- [103] Ludwik Leibler, Henri Orland, and John C. Wheeler. "Theory of critical micelle concentration for solutions of block copolymers." In: *The Journal of Chemical Physics* 79.7 (1983), pp. 3550–3557. doi: [10.1063/1.446209](https://doi.org/10.1063/1.446209) (cited on page 21).
- [104] Tom C. Jellicoe, Johannes M. Richter, Hugh F. J. Glass, Maxim Tabachnyk, Ryan Brady, Siân E. Dutton, Akshay Rao, Richard H. Friend, Dan Credgington, Neil C. Greenham, and Marcus L. Böhm. "Synthesis and optical properties of lead-free cesium tin halide perovskite nanocrystals." In: *Journal of the American Chemical Society* 138.9 (2016), pp. 2941–2944. doi: [10.1021/jacs.5b13470](https://doi.org/10.1021/jacs.5b13470) (cited on page 22).
- [105] Aifei Wang, Yanyan Guo, Faheem Muhammad, and Zhengtao Deng. "Controlled synthesis of lead-free cesium tin halide perovskite cubic nanocages with high stability." In: *Chemistry of Materials* 29.15 (2017), pp. 6493–6501. doi: [10.1021/acs.chemmater.7b02089](https://doi.org/10.1021/acs.chemmater.7b02089) (cited on page 22).
- [106] Xiaotong Wu, Weidong Song, Qian Li, Xixia Zhao, Dongsheng He, and Zewei Qian. "Synthesis of lead-free CsGeI₃ perovskite colloidal nanocrystals and electron beam-induced transformations." In: *Chemistry—An Asian Journal* 13.13 (2018), pp. 1654–1659. doi: [10.1002/asia.201800573](https://doi.org/10.1002/asia.201800573) (cited on page 22).
- [107] Xin-Gang Zhao, Ji-Hui Yang, Yuhao Fu, Dongwen Yang, Qiaoling Xu, Liping Yu, Su-Huai Wei, and Lijun Zhang. "Design of lead-free inorganic halide perovskites for solar cells via cation-transmutation." In: *Journal of the American Chemical Society* 139.7 (2017), pp. 2630–2638. doi: [10.1021/jacs.6b09645](https://doi.org/10.1021/jacs.6b09645) (cited on page 22).
- [108] Sidney E. Creutz, Evan N. Crites, Michael C. De Siena, and Daniel R. Gamelin. "Colloidal nanocrystals of lead-free double-perovskite (elpasolite) semiconductors: synthesis and anion exchange to access new materials." In: *Nano Letters* 18.2 (2018), pp. 1118–1123. doi: [10.1021/acs.nanolett.7b04659](https://doi.org/10.1021/acs.nanolett.7b04659) (cited on page 22).
- [109] Meiyang Leng, Zhengwu Chen, Ying Yang, Zha Li, Kai Zeng, Kanghua Li, Guangda Niu, Yisu He, Qingchao Zhou, and Jiang Tang. "Lead-free, blue emitting bismuth halide perovskite quantum dots." In: *Angewandte Chemie International Edition* 55.48 (2016), pp. 15012–15016. doi: [10.1002/anie.201608160](https://doi.org/10.1002/anie.201608160) (cited on pages 22, 23).
- [110] Meiyang Leng, Ying Yang, Kai Zeng, Zhengwu Chen, Zhifang Tan, Shunran Li, Jinghui Li, Bing Xu, Dengbing Li, Matthew P. Hautzinger, Yongping Fu, Tianyou Zhai, Ling Xu, Guangda Niu, Song Jin, and Jiang Tang. "All-inorganic bismuth-based perovskite quantum dots with bright blue photoluminescence and excellent stability." In: *Advanced Functional Materials* 28.1 (2018), p. 1704446. doi: [10.1002/adfm.201704446](https://doi.org/10.1002/adfm.201704446) (cited on page 22).
- [111] Jian Zhang, Ying Yang, Hui Deng, Umar Farooq, Xiaokun Yang, Jahangeer Khan, Jiang Tang, and Haisheng Song. "High quantum yield blue emission from lead-free inorganic antimony halide perovskite colloidal quantum dots." In: *ACS Nano* 11.9 (2017), pp. 9294–9302. doi: [10.1021/acsnano.7b04683](https://doi.org/10.1021/acsnano.7b04683) (cited on page 22).
- [112] Jackson D. Majher, Matthew B. Gray, T. Amanda Strom, and Patrick M. Woodward. "Cs₂NaBiCl₆: Mn²⁺—a new orange-red halide double perovskite phosphor." In: *Chemistry of Materials* 31.5 (2019), pp. 1738–1744. doi: [10.1021/acs.chemmater.8b05280](https://doi.org/10.1021/acs.chemmater.8b05280) (cited on page 23).
- [113] Wonseok Lee, Doowon Choi, and Sungjee Kim. "Colloidal Synthesis of Shape-Controlled Cs₂NaBiX₆ (X = Cl, Br) Double Perovskite Nanocrystals: Discrete Optical Transition by Non-Bonding Characters and Energy Transfer to Mn Dopants." In: *Chemistry of Materials* 32.16 (2020), pp. 6864–6874. doi: [10.1021/acs.chemmater.0c01315](https://doi.org/10.1021/acs.chemmater.0c01315) (cited on page 23).
- [114] Ming-Ming Yao, Li Wang, Ji-Song Yao, Kun-Hua Wang, Chen Chen, Bai-Sheng Zhu, Jun-Nan Yang, Jing-Jing Wang, Wei-Ping Xu, Qun Zhang, and Hong-Bin Yao. "Improving lead-free double perovskite Cs₂NaBiCl₆ nanocrystal optical properties via ion doping." In: *Advanced Optical Materials* 8.8 (2020), p. 1901919. doi: [10.1002/adom.201901919](https://doi.org/10.1002/adom.201901919) (cited on pages 23, 78).
- [115] Peigeng Han, Xue Zhang, Cheng Luo, Wei Zhou, Songqiu Yang, Jianzhang Zhao, Weiqiao Deng, and Keli Han. "Manganese-doped, lead-free double perovskite nanocrystals for bright orange-red emission." In: *ACS Central Science* 6.4 (2020), pp. 566–572. doi: [10.1021/acscentsci.0c00056](https://doi.org/10.1021/acscentsci.0c00056) (cited on pages 23, 78).

- [116] Pierre Hohenberg and Walter Kohn. “Inhomogeneous electron gas.” In: *Physical Review* 136.3B (1964), B864. doi: [10.1103/PhysRev.136.B864](https://doi.org/10.1103/PhysRev.136.B864) (cited on page 24).
- [117] A. Hussain, L. H. Yang, Y. B. Zou, S. F. Mao, B. Da, H. M. Li, and Z. J. Ding. “Monte Carlo simulation study of electron yields from compound semiconductor materials.” In: *Journal of Applied Physics* 128.1 (2020), p. 015305. doi: [10.1063/5.0012154](https://doi.org/10.1063/5.0012154) (cited on page 24).
- [118] Berni J. Alder and Thomas Everett Wainwright. “Studies in molecular dynamics. I. General method.” In: *The Journal of Chemical Physics* 31.2 (1959), pp. 459–466. doi: [/10.1063/1.1730376](https://doi.org/10.1063/1.1730376) (cited on page 24).
- [119] Qiuling Tao, Pengcheng Xu, Minjie Li, and Wencong Lu. “Machine learning for perovskite materials design and discovery.” In: *npj Computational Materials* 7.1 (2021), pp. 1–18. doi: [10.1038/s41524-021-00495-8](https://doi.org/10.1038/s41524-021-00495-8) (cited on page 24).
- [120] Valentin Stanev, Corey Oses, A Gilad Kusne, Efrain Rodriguez, Johnpierre Paglione, Stefano Curtarolo, and Ichiro Takeuchi. “Machine learning modeling of superconducting critical temperature.” In: *npj Computational Materials* 4.1 (2018), pp. 1–14. doi: [10.1038/s41524-018-0085-8](https://doi.org/10.1038/s41524-018-0085-8) (cited on page 24).
- [121] Wenbo Sun, Yujie Zheng, Ke Yang, Qi Zhang, Akeel A Shah, Zhou Wu, Yuyang Sun, Liang Feng, Dongyang Chen, Zeyun Xiao, Shirong Lu, Yong Li, and Kuan Sun. “Machine learning–assisted molecular design and efficiency prediction for high-performance organic photovoltaic materials.” In: *Science Advances* 5.11 (2019), eaay4275. doi: [10.1126/sciadv.aay4275](https://doi.org/10.1126/sciadv.aay4275) (cited on page 24).
- [122] “Lattice constant prediction of cubic and monoclinic perovskites using neural networks and support vector regression.” In: *Computational Materials Science* 50.2 (2010), pp. 363–372. doi: <https://doi.org/10.1016/j.commatsci.2010.08.028> (cited on page 24).
- [123] Jared C. Stanley, Felix Mayr, and Alessio Gagliardi. “Machine Learning Stability and Bandgaps of Lead-Free Perovskites for Photovoltaics.” In: *Advanced Theory and Simulations* 3.1 (), p. 1900178. doi: <https://doi.org/10.1002/adts.201900178> (cited on page 24).
- [124] Zheng Li, Luke E. K. Achenie, and Hongliang Xin. “An Adaptive Machine Learning Strategy for Accelerating Discovery of Perovskite Electrocatalysts.” In: *ACS Catalysis* 10.7 (2020), pp. 4377–4384. doi: [10.1021/acscatal.9b05248](https://doi.org/10.1021/acscatal.9b05248) (cited on page 24).
- [125] Nobel Prize Outreach. *The Nobel Prize in Physics 1901*. 2022. URL: <https://www.nobelprize.org/prizes/physics/1901/summary/> (visited on 05/10/2022) (cited on page 30).
- [126] Nobel Prize Outreach. *The Nobel Prize in Physics 1914*. 2022. URL: <https://www.nobelprize.org/prizes/physics/1914/summary/> (visited on 05/10/2022) (cited on page 30).
- [127] Linda K. Bruetzel, Stefan Fischer, Annalena Salditt, Steffen M. Sedlak, Bert Nickel, and Jan Lipfert. “A Mo-anode-based in-house source for small-angle X-ray scattering measurements of biological macromolecules.” In: *Review of Scientific Instruments* 87.2 (2016), p. 025103. doi: [10.1063/1.4940936](https://doi.org/10.1063/1.4940936) (cited on page 31).
- [128] DESY. *P07 - Unified Data Sheet*. 2013. URL: https://photon-science.desy.de/facilities/petra_iii/beamlines/p07_high_energy_materials_science/unified_data_sheet_p07/index_eng.html (visited on 04/21/2022) (cited on page 32).
- [129] DESY. *P62 - Unified Data Sheet*. 2021. URL: https://photon-science.desy.de/facilities/petra_iii/beamlines/p62_saxsmat/unified_data_sheet/index_eng.html (visited on 04/21/2022) (cited on page 32).
- [130] R Pecora. “Dynamic light scattering measurement of nanometer particles in liquids.” In: *Journal of Nanoparticle Research* 2.2 (2000), pp. 123–131. doi: [10.1023/A:1010067107182](https://doi.org/10.1023/A:1010067107182) (cited on page 33).
- [131] Richard Anthony Lewis Jones, Richard AL Jones, R Jones, et al. *Soft condensed matter*. Vol. 6. Oxford University Press, 2002 (cited on page 33).
- [132] Fabian Pedregosa, Gaël Varoquaux, Alexandre Gramfort, Vincent Michel, Bertrand Thirion, Olivier Grisel, Mathieu Blondel, Peter Prettenhofer, Ron Weiss, Vincent Dubourg, Jake Vanderplas, Alexandre passos, David Cournapeau, Matthieu Brucher, Matthieu Perrot, and Edouard Duchesnay. “Scikit-learn: Machine learning in Python.” In: *The Journal of Machine Learning Research* 12 (2011), pp. 2825–2830 (cited on page 35).
- [133] Martín Abadi, Ashish Agarwal, Paul Barham, Eugene Brevdo, Zhifeng Chen, Craig Citro, Greg S Corrado, Andy Davis, Jeffrey Dean, Matthieu Devin, Sanjay Ghemawat, Ian Goodfellow, Andrew Harp, Geoffrey Irving, Michael Isard, Yangqing Jia, Rafal Jozefowicz, Lukasz Kaiser, Manjunath Kudlur, Josh Levenberg, Dan Mane, Rajat Monga, Sherry Moore, Derek Murray, Chris Olah, Mike Schuster, Jonathon Shlens, Benoit Steiner, Ilya Sutskever, Kunal Talwar, Paul Tucker, Vincent Vanhoucke, Vijay Vasudevan, Fernanda Viegas, Oriol Vinyals, Pete Warden, Martin Wattenberg, Martin Wicke, Yuan Yu, and Xiaoqiang Zheng. *TensorFlow: Large-scale machine learning on heterogeneous systems*. 2015 (cited on page 35).
- [134] Verena A. Hintermayr, Carola Lampe, Maximilian Löw, Janina Roemer, Willem Vanderlinden, Moritz Gramlich, Anton X. Böhm, Cornelia Sattler, Bert Nickel, Theobald Lohmüller, and Alexander S. Urban. “Polymer nanoreactors shield perovskite nanocrystals from degradation.” In: *Nano Letters* 19.8 (2019), pp. 4928–4933. doi: [10.1021/acs.nanolett.9b00982](https://doi.org/10.1021/acs.nanolett.9b00982) (cited on pages 37, 38, 40–44, 51).
- [135] Qi Xue, Carola Lampe, Tassilo Naujoks, Kilian Frank, Moritz Gramlich, Markus Schoger, Willem Vanderlinden, Patrick Reisbeck, Bert Nickel, Wolfgang Brütting, and Alexander S. Urban. “Doubly Stabilized Perovskite Nanocrystal Luminescence Downconverters.” In: *Advanced Optical Materials* n/a.n/a (), p. 2102791. doi: <https://doi.org/10.1002/adom.202102791> (cited on pages 37, 49, 52).

- [136] Shaocong Hou, Yuzheng Guo, Yuguo Tang, and Qimin Quan. "Synthesis and stabilization of colloidal perovskite nanocrystals by multidentate polymer micelles." In: *ACS Applied Materials & Interfaces* 9.22 (2017), pp. 18417–18422. doi: [10.1021/acsami.7b03445](https://doi.org/10.1021/acsami.7b03445) (cited on page 39).
- [137] Constantinos C Stoumpos, Christos D Malliakas, and Mercouri G Kanatzidis. "Semiconducting tin and lead iodide perovskites with organic cations: phase transitions, high mobilities, and near-infrared photoluminescent properties." In: *Inorganic Chemistry* 52.15 (2013), pp. 9019–9038. doi: [10.1021/ic401215x](https://doi.org/10.1021/ic401215x) (cited on pages 41, 42).
- [138] Cristiane R Martins, Giacomo Ruggeri, and Marco-A De Paoli. "Synthesis in pilot plant scale and physical properties of sulfonated polystyrene." In: *Journal of the Brazilian Chemical Society* 14.5 (2003), pp. 797–802 (cited on page 41).
- [139] Önder Topel, Burçin Acar Çakır, Leyla Budama, and Numan Hoda. "Determination of critical micelle concentration of polybutadiene-block-poly (ethyleneoxide) diblock copolymer by fluorescence spectroscopy and dynamic light scattering." In: *Journal of Molecular Liquids* 177 (2013), pp. 40–43. doi: [10.1016/j.molliq.2012.10.013](https://doi.org/10.1016/j.molliq.2012.10.013) (cited on page 45).
- [140] Francisco Palazon, Quinten A Akkerman, Mirko Prato, and Liberato Manna. "X-ray lithography on perovskite nanocrystals films: from patterning with anion-exchange reactions to enhanced stability in air and water." In: *ACS Nano* 10.1 (2016), pp. 1224–1230. doi: [10.1021/acsnano.5b06536](https://doi.org/10.1021/acsnano.5b06536) (cited on page 51).
- [141] Diego Di Girolamo, M Ibrahim Dar, Danilo Dini, Lorenzo Gontrani, Ruggero Caminiti, Alessandro Mattoni, Michael Graetzel, and Simone Meloni. "Dual effect of humidity on cesium lead bromide: enhancement and degradation of perovskite films." In: *Journal of Materials Chemistry A* 7.19 (2019), pp. 12292–12302. doi: [10.1039/C9TA00715F](https://doi.org/10.1039/C9TA00715F) (cited on page 51).
- [142] Caroline Murawski, Karl Leo, and Malte C. Gather. "Efficiency roll-off in organic light-emitting diodes." In: *Advanced Materials* 25.47 (2013), pp. 6801–6827. doi: [10.1002/adma.201301603](https://doi.org/10.1002/adma.201301603) (cited on page 52).
- [143] Kebin Lin, Jun Xing, Li Na Quan, FPG De Arquer, Xiwen Gong, Jianxun Lu, Liqiang Xie, Weijie Zhao, Di Zhang, Chuanzhong Yan, Wenqiang Li, Yan Lu, Jeffrey Kirman, Edward H. Sargent, Qihua Xiong, and Zhanhua Wei. "Perovskite light-emitting diodes with external quantum efficiency exceeding 20%." In: *Nature* 562.7726 (2018), pp. 245–248. doi: [10.1038/s41586-018-0575-3](https://doi.org/10.1038/s41586-018-0575-3) (cited on page 58).
- [144] Xiaofei Zhao, Jun De Andrew Ng, Richard H Friend, and Zhi-Kuang Tan. "Opportunities and challenges in perovskite light-emitting devices." In: *ACS Photonics* 5.10 (2018), pp. 3866–3875. doi: [10.1021/acsp Photonics.8b00745](https://doi.org/10.1021/acsp Photonics.8b00745) (cited on pages 58, 61).
- [145] *Parameter values for ultra-high definition television systems for production and international programme exchange*. 2020. URL: <https://www.itu.int/rec/R-REC-BT.2020-2-201510-I/en> (visited on 04/21/2022) (cited on page 58).
- [146] Thomas Morgenstern, Carola Lampe, Tassilo Naujoks, Matthew Jurow, Yi Liu, Alexander S. Urban, and Wolfgang Brütting. "Elucidating the performance limits of perovskite nanocrystal light emitting diodes." In: *Journal of Luminescence* 220 (2020), p. 116939. doi: [10.1016/j.jlumin.2019.116939](https://doi.org/10.1016/j.jlumin.2019.116939) (cited on page 58).
- [147] Matthew J. Jurow, Thomas Lampe, Erika Penzo, Jun Kang, Matthew A Koc, Thomas Zechel, Zachary Nett, Michael Brady, Lin-Wang Wang, A. Paul Alivisatos, Stefano Cabrini, Wolfgang Brütting, and Yi Liu. "Tunable anisotropic photon emission from self-organized CsPbBr₃ perovskite nanocrystals." In: *Nano Letters* 17.7 (2017), pp. 4534–4540. doi: [10.1021/acs.nanolett.7b02147](https://doi.org/10.1021/acs.nanolett.7b02147) (cited on page 60).
- [148] Thomas Morgenstern. "Preferential alignment of anisotropic transition dipole moments in organic and perovskite thin films." Dissertation. Universität Augsburg, 2019 (cited on page 61).
- [149] Matthew J Jurow, Thomas Morgenstern, Carissa Eisler, Jun Kang, Erika Penzo, Mai Do, Manuel Engelmayr, Wojciech T Osowiecki, Yehonadav Bekenstein, Christopher Tassone, LinWang Wang, A. Paul Alivisatos, Wolfgang Brütting, and Yi Liu. "Manipulating the transition dipole moment of CsPbBr₃ perovskite nanocrystals for superior optical properties." In: *Nano Letters* 19.4 (2019), pp. 2489–2496. doi: [10.1021/acs.nanolett.9b00122](https://doi.org/10.1021/acs.nanolett.9b00122) (cited on page 61).
- [150] Moritz Gramlich, Michael W. Swift, Carola Lampe, John L. Lyons, Markus Döblinger, Alexander L. Efros, Peter C. Sercel, and Alexander S. Urban. "Dark and Bright Excitons in Halide Perovskite Nanoplatelets." In: *Advanced Science* (2021), p. 2103013. doi: [10.1002/advs.202103013](https://doi.org/10.1002/advs.202103013) (cited on page 66).

List of Figures

2.1	Simple Cubic Crystal Lattice	4
2.2	Brillouin Zone	5
2.3	Direct and Indirect Bandgaps in Semiconductors	6
2.4	Wannier-Mott Exciton and its Energetic States	7
2.5	Effect of Quantum Confinement - From 3D to 2D	10
2.6	Perovskite Crystal Structure	11
2.7	Structure Factors for 3D Lead Perovskites	12
2.8	Band Structure and Partial Density of States CsPbBr ₃	13
2.9	Electronic Band Structure of Lead Halide Perovskites	14
2.10	Photoluminescence and Absorption Spectra of CsPbBr ₃ -based Nanoplatelets	17
2.11	Typical Organic Ligands for Perovskite Nanocrystals	18
2.12	Enhancement of CsPbBr ₃ -based Nanoplatelets	18
2.13	Polystyrene-Polyvinyl Pyridine Diblock Copolymer	21
2.14	Micellization and Micelle Films	21
2.15	Double Perovskite Structure	22
2.16	Reported Properties of Mn:Cs ₂ NaBiCl ₆ Nanocrystals	23
3.1	Transmission Electron Microscope	30
3.2	Bragg's Law	31
3.3	Schematic Depiction of the Mo-based Small-Angle X-Ray Scattering Setup	31
3.4	Schematic Description of the In-situ Synthesis Setup	32
3.5	Schematic Description of the Flouromax4-Plus	34
4.1	Photoluminescence Spectra of Micelle-Encapsulated Methylammonium Halide Perovskites	38
4.2	Photoluminescence Spectra of Micelle-Encapsulated Mixed Perovskites	39
4.3	TEM and AFM images of Micelle Monolayers	40
4.4	TEM Images and Corresponding Size Distributions for Different PS-PVP Polymer Lengths	41
4.5	Size Dependence of PS-PVP Micelles	41
4.6	WAXS and SAXS analysis of Micelle Encapsulated Nanocrystals	42
4.7	Photoluminescence Analysis of Differently Fabricated and Stored LHP NC Films Before and After Stability Experiments	43
4.8	Enhanced Stability of Diblock Copolymer Micelle Encapsulated Nanocrystals	43
4.9	Förster Resonance Energy Transfer Between Micelle Encapsulated LHP NCs	44
4.10	Exemplary Analysis of DLS Measurements of PS(113)-PVP(143)	46
4.11	Diblock Copolymer Size Distribution Obtained from DLS Measurements	46

4.12	Time Dependent Size Distributions Upon MABr Injection in Polymer Micelle Solutions	47
4.13	Photoluminescence Spectra of Micelle-Encapsulated MAPbBr ₃ NCs Synthesized With Original and Optimized Synthesis Parameter	48
4.14	General Characterization of Doubly Stabilized LHP NCs Films	49
4.15	XRD Analysis of Doubly Stabilized Nanocrystals	50
4.16	Schematic Depiction of a Thin Film Comprising Doubly Stabilized LHP NCs	50
4.17	Optical Properties of Doubly Stabilized LHP NCs	52
4.18	TEM Analysis of Doubly Stabilized LHP NCs	53
4.19	Optical Properties of Doubly Stabilized LHP NCs Synthesized with Organic Ligands	53
4.20	Stability of Doubly Stabilized LHP NCs	54
4.21	Perovskite Downconverter-OLED	54
5.1	Schematic Description of the Alignment Constant	59
5.2	Simulations of the Outcoupling Efficiency Depending on the Refractive Index and TDM Angle of an Emitter	59
5.3	Angular Dependent Radiation Pattern of 3 ML NPL	60
5.4	Alignment Constant of Each NPL Thickness	60
5.5	Outcoupling Efficiency Limits of Perovskite-Based LEDs	61
5.6	EQE Limits of Perovskite-Based LEDs	61
5.7	Scheme of the Optimization Process	63
5.8	Photoluminescence Data from the Optimization	65
5.9	Optimized Nanoplatelet Properties	65
5.10	Image of Mixed Halide 5 ML Nanoplatelets Under UV illumination	67
5.11	Absorption and Photoluminescence Spectra of Mixed Halide 5 ML Nanoplatelets	68
5.12	TEM Images of Mixed Halide 5 ML Nanoplatelets	68
5.13	Absorption and Photoluminescence Spectra of Mixed Halide 4 ML Nanoplatelets	69
5.14	Photoluminescence Spectra of CsPbBr ₃ -based Nanoplatelets with Similar PbI ₂ Treatment	70
5.15	Photoluminescence Spectra of Mixed Halide 5 ML Nanoplatelets Before and After 4 Months Storage	70
5.16	In-Situ SAXS on a 3 ML Nanoplatelet Synthesis	72
5.17	In-Situ SAXS on a 5 ML Nanoplatelet Synthesis	72
5.18	In-Situ PL Measurement During the Synthesis of 3 ML Nanoplatelets	73
5.19	In-Situ SAXS on 3 ML Nanoplatelet Syntheses With Varying Delay Time Between Precursor Injections	74
5.20	In-Situ SAXS on the Enhancement Treatment of 3 ML Nanoplatelets	75
5.21	In-Situ SAXS on the Enhancement Treatment of 5 ML Nanoplatelets	75
6.1	Synthesis Scheme for Lead Free Double Perovskites	78
6.2	Absorption and Photoluminescence of Mn:Cs ₂ NaBiCl ₆	79
6.3	Photoluminescence of Metal Oleates	79
6.4	Impact of Repeated Purification	80

6.5	Structural Characterization of Mn:Cs ₂ NaBiCl ₆ NCs	80
6.6	Influence of the Manganese Content in Mn:Cs ₂ NaBiCl ₆ NCs	81
6.7	Impact of the Reaction Temperature on the Synthesis of Mn:Cs ₂ NaBiCl ₆ NCs	82
6.8	Long-Term Stability of Mn:Cs ₂ NaBiCl ₆ Nanocrystals	83

List of Tables

2.1	Quantum Confinement	9
3.1	Chemicals	26
3.2	Precursor Amounts for Nanoplatelets with Different Thicknesses	28
3.3	Precursor Amounts for Lead-Free Double Perovskites	29
4.1	Micelle Sizes and Spacings Obtained From TEM Imaging	40
4.2	New Synthesis Parameter for Micelle Encapsulated LHP NCs	47
4.3	PLQY of Micelle-Encapsulated MAPbBr ₃ NCs Synthesized With Original and Optimized Parameters	48
5.1	Emission Optimum, Minimum and Maximum Position for Each Nanoplatelets Thickness	64
5.2	Characteristic PL Features of Nanoplatelets After Original and Optimized Parameters	66
5.3	Precursor Ratios for Conventional and Optimized Nanoplatelet Syntheses	66

List of Abbreviations

AFM	Atomic Force Microscopy
BZ	Brillouin Zone
CB	Conduction Band
CBM	Conduction Band Minimum
CCD	Charge-Coupled Device
CMC	Critical Micelle Concentration
DESY	Deutsches Elektronen Synchrotron
DFT	Density Functional Theory
DLS	Dynamic Light Scattering
DMF	Dimethylformamide
DMSO	Dimethyl Sulfoxide
DOS	Density of States
DP	Double Perovskite
DC	Downconverter
EA	Ethylammonium
EML	Emitter Layer
EQE	External Quantum Efficiency
FA	Formamidinium
FRET	Förster Resonance Energy Transfer
FWHM	Full Width at Half Maximum
GISAXs	Grazing Incidence Small Angle X-Ray Scattering
GIWAXS	Grazing Incidence Wide Angle X-Ray Scattering
HWHM	Half Width at Half Maximum
LARP	Ligand Assisted Reprecipitation
LED	Light Emitting Diode
LFDP	Lead-Free Double Perovskite
LHP	Lead Halide Perovskite
MA	Methylammonium
ML	Monolayer
NPL	Nanoplatelet
OD	Optical Density
OLED	Organic Light Emitting Diode
PCS	Photon Correlation Spectroscopy
PL	Photoluminescence
PLQY	Photoluminescence Quantum Yield
PS	Polystyrene
PVP	Poly-2-Vinyl Pyridine
QF	Quality Factor
RT	Room Temperature
SAXS	Small Angle X-Ray Scattering
SC	Semiconductor
TCSPC	Time-Correlated Single Photon Counting
TDM	Transition Dipole Moment
TEM	Transmission Electron Microscopy
UV	Ultraviolet
VB	Valence Band
VBM	Valence Band Maximum
WAXS	Wide Angle X-Ray Scattering

Acknowledgments

I am most thankful to **Alexander Urban** for encouraging my work in chemical physics. You supported me during an internship that extended to a total of five years working with you including a master thesis and a dissertation. In my second week with you, you already told me I will stay and be a physicist without me knowing it. You put enough trust in me to help you start a new research group and built the foundation for your career as a professor. I cannot put in words how thankful I am for the time we worked together. In the last years with you, I learned how to be a better person and a better scientist. You became my mentor and a precious friend. With your own enthusiasm for science, you are a real inspiration to all of your students. I always enjoyed our Ubahn-conversations, shared your love for gin and beer and I hope we have many more evenings drinking together!

Further, I would like to thank **Moritz Gramlich** for the time we had together. As the founder of the Nanospec Group, he was the base for every setup and everything we did in the beginning. He was a great office neighbor providing every help for a fellow chemist to learn how to pretend to be a physicist. I thank **Andreas Singldinger** for trusting us enough to be one of our first students. He quickly became an irreplaceable member of the group. He is truly our Blender-King and the only one who knows everything about the laser lab. I thank **Michael Lichtenegger** for being an amazing office neighbor. He took care of every beer emergency and was always open for a chat. Thanks to **Ulrich Leo** for the most amazing red wine cake, organization of LAN parties and answering all my questions about sous vide cooking. To my fellow chemists **Nina Henke** and **Patrick Ganswindt**: I know physicists can be a pain in the lab, but they need us, so keep being a chemist ;) Thank you for every nostalgic talk about our time in the lab!

A special thanks go to all the students who worked with me! I hope you learned a lot during our time, I definitely did. Every one of you inspired me to be a better student and scientist. **Stefan Martin**, I am so happy you came back for the master thesis! I would have missed our boulder and coffee breaks. Many thanks to **Fiona Treber** for your amazing work here, you became a real friend to me! A lot of thanks to my master students **Juri Crimann** and **Hyowon Jeong**, I enjoyed every discussion about micelles and I wish you all the best for your Ph.D. studies! Thank you to **Jan, Max, Borni, Markus, Michele, Tena, Connor, Selina, Laura, Christoph, Schubi, Moritz** and every former and present colleague of the Nanospec Group!

Further, I want to thank **Bert Nickel** and **Kilian Frank** for the great collaboration! Special thanks go to Kilian for endless hours of discussions, setup planning and testing, data processing and long night shifts at DESY. He and his work contributed huge parts of this thesis. I want to thank **Ioannis Kouroudis** and **Milan Hart** for implementing the machine learning code and providing rapid feedback always. A lot of thanks go to **Tassilo Naujoks** and **Wolfgang Brütting** for the collaboration in device design.

A person necessary for my sanity and enough distraction from work is my best friend **Melli**. Every Thursday she listened to my science problems and always supported me, ready with a coffee followed by a glass of wine.

I am forever grateful for the support of **André**. You went the whole journey of the Ph.D. with me. Thank you for every week's 'Erdnuss-Ente', every time you pretended to understand whatever I said and thank you for being with me!

I am forever thankful for the support of my parents **Sandra** and **Dieter** who always encouraged me to make my own decisions and supported me throughout my time at the University. My grandfather **Hans** taught me that strength and curiosity is only limited by ourselves. A special thanks goes to my brother **Thomas**, I have never imagined to work with you as a scientist. Thank you for the support and projects together! Lastly, I apologize to my brother **Matthias** and sisters-in-law for endless science talks during our monthly family lunches but I am forever grateful for your support.